Computational Studies of Doped Tin Disulphide Monolayer for Photoelectrochemical Water Splitting

by

Onke Lwazi Gqiba

UNIVERSITEIT VAN PRETORIA
UNIVERSITY OF PRETORIA
YUNIBESITHI YA PRETORIA

Denkleiers • Leading Minds • Dikgopolo tša Dihlalefi

Submitted in fulfilment of the requirements for the degree

Master of Science (MSc) in Physics

In the Faculty of Natural and Agricultural Sciences

University of Pretoria

Supervisor: Dr. R.E. Mapasha

Co-supervisor: Prof. M. Diale

May 2023

DECLARATION

I, Onke Lwazi Gqiba, declare that the dissertation I hereby submit for the degree Master of Science (MSc) in Physics at the University of Pretoria is my work and has not been submitted previously by me or anyone else for a degree at this or any other institution.

Signature 

Student name: Onke Gqiba

Month year: May 2023

ABSTRACT

In this *ab initio* study, density functional theory, including a Hubbard U correction term (DFT+U), calculations were performed to investigate the photoelectrochemical (PEC) water splitting possibility of SnS_2 monolayer. Initially, the thermodynamic stability and photocatalytic (PC) properties of pristine SnS_2 were studied and it was found that it suffers poor electrical conductivity and the bottom of conduction band minimum (CBM) is below the reduction potential of H^+/H_2 level, limiting the PC performance. To improve performance for PEC water splitting, various doping strategies were performed on a large 5×5 SnS_2 supercell. These doping strategies are: C adsorbed onto an interstitial position, C adsorbed on a S atom, C adsorbed on a Sn atom, C substituting a S atom and C substituting a Sn atom.

Si is in the same group with C, and prefers sp^3 bonding while C prefers sp^2 bonding network. A second study involved Si doping on a 5×5 SnS_2 supercell following similar configurations to those of carbon (Si adsorbed onto an interstitial position, Si adsorbed on a S atom, Si adsorbed on a Sn atom, Si substituting a S atom and Si substituting a Sn atom). These structures were relaxed using geometric optimization (GO) options found in the Quantum esspresso packages. The following properties were calculated: formation energies, band gap (E_g) values, total and partial densities of states (TDOS and PDOS), charge density differences and band edge alignment.

The formation energies of all the doped configurations is positive, therefore they are endothermic and an external energy is necessary for synthesis of the configurations. C/Si adsorbed on a Sn atom is the most energetically favourable doping configuration. Furthermore, it was found that all the doped configurations have E_g values less than that of pristine SnS_2 monolayer, but still fall within the visible light activation energy region. It was further established that doping configurations: C/Si adsorbed on an interstitial position, C/Si adsorbed on a S atom and C/Si adsorbed on a Sn atom, are n-type materials which introduce intermediate bands (IBs). These IBs act as a stepping stone of photon energy between the VBM and the CBM. The configurations: C/Si substituting a S atom

and C/Si substituting a Sn atom, are p-type materials and have no IBs which reduces the possibility of quick recombination of the electron-hole pairs.

From charge density difference diagram analysis of these doping configurations, C dopant is the positive centre which could act as oxidants and Si is the negative centre which could act as reductants. Lastly, band edge alignment for pristine and doped SnS_2 configurations were all suitable for oxygen evolution, as VBMs of the materials are below the oxygen evolution potential O_2/H_2O. However, an external bias as a means of donating electrons into the material to raise CBM to energy levels above the water reduction potential H^+/H_2 will be needed. The presented results will be beneficial to experimentalists concerned about the production of clean H_2 fuel.

DEDICATION

This dissertation is dedicated to:

- My mother, Pinkie Dinah Gqiba, and father, Dumisani Sanele Gqiba, for their love and support.
- My sister, Dr Akhona Gqiba Nqala, and brother-in-law, Dr Onke Nqala for their love and support.
- My daughter, Khazimla Ulikhwezi Ngubo, whom I love dearly.
- My nieces, Iminathi Nqala and Philasande Nqala, whom I love dearly.

ACKNOWLEDGEMENTS

- I thank GOD Almighty for providing me with grace, strength and wisdom to understand and complete this MSc program.
- I would like to convey my deepest gratitude to my supervisor Dr R.E. Mapasha for his never-ending patience, support, encouragement, guidance, valuable knowledge and discussions throughout my MSc research.
- I would like to express my deepest appreciation to my co-supervisor Prof M Diale for her warm welcoming, guidance, knowledge and enabling financial support for me.
- I thank the University of Pretoria for accepting me and providing computational resources to pursue my MSc research.
- I thank the Head of the Department of Physics, Prof. Chris Theron, for the constant support in the department throughout my study.
- I thank Prof Walter Meyer and Dr Jannie Pretorius for helping with computational resources.
- I would like to acknowledge the National Research Fund (NRF) for their financial support throughout my studies.
- I would like to acknowledge the Centre for High-Performance Computing (CHPC) in Cape Town, South Africa for allowing me to conduct calculations through their cluster
- I thank my research group members and friends for their academic and social support.
- Finally, my heartfelt gratitude to my family for their love and support throughout my MSc research.

TABLE OF CONTENTS

List of figures

List of tables

LIST OF ABBREVIATIONS

PEC	Photoelectrochemical
PV	Photovoltaic
Å	Angstroms
eV	Electronvolts
VBM	Valence band maximum
CBM	Conduction band minimum
FFs	Fossil fuels
SA	Surface area
V	Volume
HER	Hydrogen evolution reaction
OER	Oxygen evolution reaction
QM	Quantum mechanical
IBs	Intermediate bands
DFT	Density functional theory
WS	Water splitting
LDA	Local density approximation
LSDA	Local spin density approxmiation
DOS	Density of states
E_g	Band gap
GGA	Generalized gradient approximation
GGA+U/DFT+U	Generalized gradient approximation with a Hubbard U value
FGO	Full geometric optimization
QESP	Quantum-espressso simulation package

CHAPTER 1: INTRODUCTION

1.1 Brief introduction

In this chapter, we introduce the main idea of the research carried out. Firstly socio-economic problems such as worldwide energy shortages and technological solutions considered nowadays are mentioned. The necessity of two-dimensional (2D) semiconductors for photocatalytic water splitting are discussed to illuminate the motivation of the research. Lastly, we briefly highlight the methodology and computational techniques capable of conducting this research. Thereafter the aims with several objectives are highlighted.

1.2 Rationale

The increasing need for energy supply coupled with the shortage of energy sources has urged an increase in the search for more clean renewable sources. Up to 80% of the world population relies on the depleting and polluting fossil fuels (FFs) [1]. FFs inject up to 5.981 million metric tons of carbon dioxide (CO_2), a harmful greenhouse gas, into the atmosphere [2]. The critical problem this research aims to investigate is how to use a 2D material to synthesize an environmentally friendly energy fuel from a renewable source. FFs are known to be primary energy sources purely from the nature [3]. Examples of primary energy sources are: sun (solar), radioisotopes used in nuclear power stations, wind, wave, biomass, geothermal, etc. [3, 4, 5]. In the future, the most promising, clean and inexhaustible source of energy will be the sun. About $3 \times 10^{24} J$ of solar energy is received by the earth annually, which is 10 000 times more than the annual global energy consumption from FFs [1, 6, 7].

Primary energy sources are engineered into secondary energy sources which can be stored and transported [8]. Secondary energy sources are also classified as fuels, since they are also energy carriers and are: Electricity, chemicals used in batteries, petrol, diesel, hydrogen (H_2), oxygen (O_2), etc. [8-10]. Majority of primary energy sources are used to produce electricity [5, 9, 10], the only energy carrier that is able to effortlessly be converted into multiple forms of daily usable energy. Extensive research has been invested on electricity and storage techniques [5, 11-13]. The methods or sources of energy researched have to be efficient and low cost approaches. It has been widely identified that using the abundant solar energy to produce hydrogen fuel from water is one of the most efficient ways to store solar energy and produce electricity [6, 14, 15, 16, 17].

Hydrogen is the lightest gas and is the most abundant element in the whole universe [18]. It is a highly reactive, in fact an explosive gas and requires very minimal energy to start reacting [19]. Hydrogen combusts explosively with oxygen following equation (1.1) below [20], producing a heat intensity with a higher combustion index or ignitability to that of both natural gas and FFs [19],

$$2H_2(g) + O_2(g) \xrightarrow[\Delta]{} 2H_2O(l). \quad (1.1)$$

The short arrow indicates the spontaneity of the reaction. Since water and heat are the only products, combustion of hydrogen is a clean energy production process. Hydrogen has been used as rocket fuel and high temperature industrial furnaces fuel for its enormous energy output [21]. However, the enormous energy generated from hydrogen has its advantages and disadvantages. Advantage is that a lesser amount of hydrogen is needed to get the same energy given by FFs [19] and the disadvantage is that storing and transporting large amounts of hydrogen fuel is very dangerous due to its highly explosive nature [19, 22]. The production of energy using hydrogen may be a clean process, but the current existing methods of producing hydrogen are not clean processes. Some articles have reported that the production of hydrogen releases more greenhouse gases than the use of FFs [23]. Methods of hydrogen production follow these reaction mechanisms:

Acid & Metals Reactions [24]: $2HCl\,(l) + 2Zn(s) \longrightarrow 2ZnCl(s) + H_2(g)$ (1.2)

$$Fe(s) + H_2SO_4(l) \longrightarrow FeSO_4(s) + H_2(g) \quad (1.3)$$

Equation (1.2) is the decomposition of zinc in hydrochloric acid to produce zinc chloride salts and hydrogen gas. Similarly, equation (1.3) is the decomposition of iron in sulfuric acid to produce iron sulphate salts and hydrogen gas.

Natural gas reforming [23, 25]: $$CH_4(g) + H_2O(g) \xrightarrow[700-1000℃]{} CO(g) + 3H_2(g) \quad (1.4)$$

$$CO(g) + H_2O(g) \xrightarrow[360℃]{} CO_2(g) + H_2(g) \quad (1.5)$$

Steam reforming of natural gas is the majorly explored method of hydrogen production [23]. Steam reforming produces carbon monoxide (CO), a very toxic gas, and hydrogen. Subsequently, the CO is also steamed to produce CO_2 and more hydrogen gas.

Voltaic Production [26]: $$2H_2O(l) + electricity \xrightarrow{Na_2SO_4} 2H_2(g) + O_2(g) \quad (1.6)$$

Biotechnology [15]: Using algae and bacteria to produce hydrogen.

Voltaic production (VP) and biotechnology are considered to be the cleanest of all mentioned hydrogen production methods. Biotechnological method uses micro-organisms which produce hydrogen naturally from sunlight [15]. VP method synthesizes hydrogen using electricity, from a voltage source, and water [27]. The electricity is the activation energy that separates water into its components, a process called electrolysis [23]. Electrolysis of clean water is non-spontaneous as water, on its own, is very stable. Therefore, Na_2SO_4 is the catalyst in the electrolyte, which acts as the charge carrier to allow for rapid charge movement in the solution [26]. Since water covers up 70% of the planet's surface [28], VP could have been a possibility for mass producing hydrogen, however the electricity, for electrolysis, is still produced from FFs. Thus, eliminating VP of hydrogen as an absolute clean method for energy storage.

Hydrogen and electricity have a good sibling relationship. Until recently, there was no way to safely process hydrogen to another form of energy. It is until the 1990s [22] that hydrogen can be converted into electricity through the use of fuel cells [14]. There are different types of fuel cells, namely: Proton exchange membrane (PEM) fuel cell [29], Anion exchange membrane (AEM) fuel cell [30] and hydrogen fuel cell [14, 22]. These fuel cells use membrane technology [31, 32]. Membranes are semipermeable and porous polymers which selectively allow the exchange or passing through of only a specific particle. The particle could be a charge, element, ion or molecule. The name of the fuel cell

specifies what type of particle can migrate through. The PEM fuel cells only conduct protons and cations through the membrane, the AEM fuel cells only conduct electrons and anions through the membrane and for hydrogen fuel cells, only hydrogen can migrate through the membrane. The hydrogen fuel cell uses the same concept as PEM fuel cell, in that case the proton allowed to pass through the membrane is a hydrogen atom which has been stripped off its electron [33].

Hydrogen fuel cells are based on the idea that hydrogen (H_2) and oxygen (O_2) gas always want to come together to form water [19]. Since the hydrogen atom consists of only one proton and electron, it has a relatively low ionization energy, as all group 1 elements have very low ionization energies [34]. Thus, hydrogen's proton and electron are easily separated. In the hydrogen fuel cell, as illustrated in figure 1.1, hydrogen is oxidized at the anode and reduced at the cathode [18]. The catalyst in the platinum (Pt) based anode coupled with the electrolyte in the PEM membrane split the hydrogen into an electron and proton [29]. The H^+ ions migrate through the membrane to the cathode [29]. The electrons, which cleaved hydrogen, can feel the positive charge (potential difference) at the other side of the membrane, which is at the cathode. However, the membrane is chemically insulated from electrons [31, 32], therefore electrons flow through the external (conductor) to the other terminal causing current which generates electricity. At the cathode, electrons reduce hydrogen ions to hydrogen gas which bonds with atmospheric oxygen to produce water. Therefore, the water used to produce hydrogen is returned back to the environment where it can be reused to again produce hydrogen. Thus, not only is this a process for clean electricity production, but is also a continuous cycle which would remove the strain of depending on the depleting and environmentally unfriendly FFs.

Through the use of hydrogen fuel cells, hydrogen has become the fuel used to drive vehicles [18]. In the vehicle, the electric current derived from the hydrogen drives the motor propelling the vehicle and empowers all other electronic devices. In a hydrogen driven car, the fuel cells are stacked together, like slices of bread, in order to increase the vehicle's power and performance [14, 22, 25]. This same concept can be applied for emission free power generation for homes, cities and industries [14, 35, 36], which would be the realization of a hydrogen driven economy. With more years of research and

technological improvements, fuel cell technology may be used to produce hydrogen fuel directly from water.

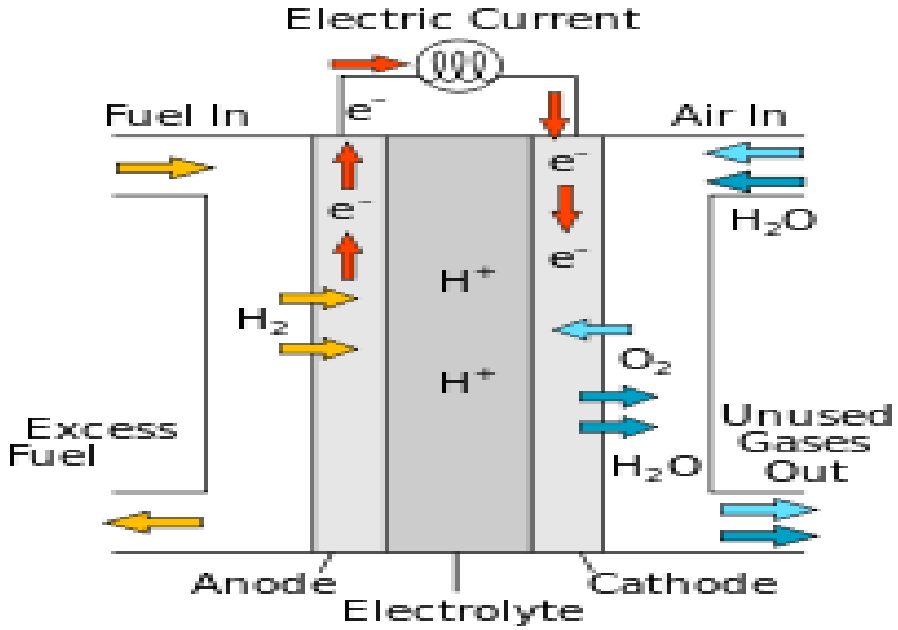

Figure 1.1: Schematic diagram of a hydrogen fuel cell used to produce electricity. A hydrogen fuel cell uses the proton exchange membrane as the exchange electrolyte [14, 37].

We have discussed the magnificence of electricity production using hydrogen gas and its potential as a champion fuel to drive the economy of the world. Developing affordable and renewable technologies of producing hydrogen with less damage to the environment would complete the puzzle of a hydrogen economy. Therefore, we propose using a photocatalyst to produce the electric current to drive decomposition of water into hydrogen and oxygen, a process called photoelectrochemical (PEC) water splitting (WS). A photocatalyst is a material which converts solar energy into electric current [38].

It is worth mentioning that other techniques of WS using solar energy are: photoelctrochemical (PEC), photovoltaic (PV), solar thermal (ST), photothermal catalysis (PTC) and photobiological technologies (PBT) [16]. For PEC WS, the photocatalyst material is submerged into the water wherein the sunlight activates the electrons in the material to produce the current which catalyses WS, as shown in figure 1.2. The photocatalyst plays the role of an electrode. Since the activation energy of the electrode

comes from solar energy, it is referred to as a stand-alone photoelectrode [17]. A stand-alone photoelectrode can perform water splitting for both water oxidation and water reduction [14, 39], following equations (1.7) and (1.8) below:

Water reduction reaction [40]: $$2H^+ + 2e^- \rightarrow H_2 \quad (1.7)$$

Water oxidation reaction [40]: $$2H_2O + 4h^+ \rightarrow O_2 + 4H^+ \quad (1.8)$$

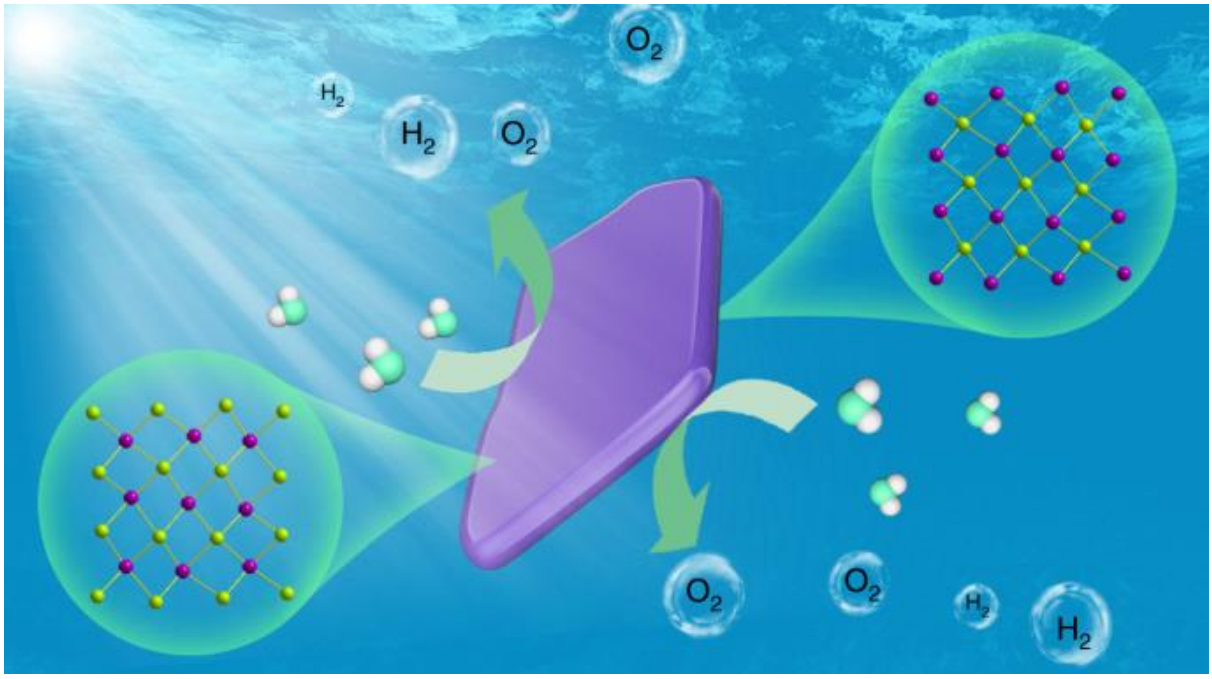

Figure 1.2: Photoelectrochemical water splitting using the technique of a stand-alone photoelectrode [17].

The challenge now is finding the best photoelectrode material. Two-dimensional (2D) semiconductors have recently found a wide range of applications in the electronics industry [41-43]. 2D materials are characterized as materials with a large surface area-to-volume ratio [44], thus the surface area is significantly larger than the volume of the material. 2D materials include: monolayers, quantum dots, nanotubes, etc. [45, 46]. Majority of 2D semiconductors are synthesized using chemical vapour deposition (CVD), exfoliation, hydrothermal synthesis, thermal decomposition, pusher laser deposition (PLD), spray pyrolysis, etc. [47]. The large surface area of 2D materials expands the active region and the ultra-thin structure reduces distance of charge migration within the material. This results in a high charge carrier mobility [48].

Each material has its characteristic valence band (VB) and conduction band (CB) energies. These characteristic bands define the type of material i.e. metals, semiconductors, insulators, etc. [49]. Semiconductors have poor conductivity and are band gap materials [49]. The band gap (E_g) is the energy gap in between the VB and CB and, by definition, is the amount of energy needed to excite an electron from the VB to the CB [50]. Once in the conduction band, the electron can move freely in the material [51], and is referred to as the conduction electron. For metals $E_g = 0eV$ [49], semiconductors $1.2eV \leq E_g \leq 4.0eV$ [6, 17, 50] and insulators have an E_g value of more or less than 9 eV [49].

Doping is a means of engineering the chemical structure of a material through defect generation [52, 53]. Doping introduces a foreign atom(s), which is not part of the periodic arrangement of the material's original atoms. This dopant will introduce defect states which hybridize with the material's states, thus changing the chemical behaviour of the material [54]. The hybridized states, as a consequence of dopant introduction, can improve charge carrier mobility of the material by making the material n-type [53, 55], therefore a good electron donor, or p-type [52, 53], which is a good electron receiver. As a result of defects, some materials may have bands occurring in between the band gap, known as intermediate bands (IBs) [50, 56]. The IBs provide a pathway for the electron to the CB. Therefore, the electron is excited from VB to IB to CB. Thus, a photocurrent is achieved even with absorption of a photon with energy less than E_g, some literatures refer to as sub-band gap energy [50]. Therefore, IBs are able to raise a material's PV efficiencies. However, the IBs should not overlap with the VB or CB to avoid any spontaneous relaxations and recombination [40].

Chapter 4 gets deeper in the details of VBs, CBs and IBs through studying a simulation of density of states (DOS), which demonstrates the positions and energies of the electronic states with respect to the VB and CB [57]. A simulation of partial density of states (PDOS) is also used to study the effects of hybridization of defect states with the material's states [58]. For both DOS and PDOS simulations, the Fermi level is the level of the highest occupied states [59].

A 2D semiconductor which has met almost all the requirements as a stand-alone photoelectrode for WS is tin disulphide (SnS_2). SnS_2 is non-toxic, earth-abundant, thus low-cost, and importantly, it is chemically stable in both acidic and neutral aqueous solutions [55, 60, 61]. SnS_2, as a photocatalyst, would ensure fast efficient electron transfer without actually participating in the reactions or dissolving in the aqueous solution. In nature, SnS_2 is an odourless, gold-yellow powder, resulting from SnS_2 monolayers stacked together and joined by weak van der Waals forces [62]. Experimental and first-principles studies have revealed that SnS_2 improves photoabsorption and has potential for PEC WS [63-66, 67]. 2D SnS_2 has applications in field effective transistors (FETs), photovoltaic solar cells, sensors, photocatalytic applications and widely reported for applications in lithium batteries [60, 62, 64, 66, 68]. SnS_2 has a band gap of 2.1-2.35 eV [62, 64, 66], which is efficient for photoabsorption [40], and crystallizes with two standard hexagonal structures, namely: 2H-Polytype and 1T-Polytype [69, 70], shown in figure 1.3.

The unit cell in both structures, illustrated by a rhombic shape, has 4 Sn atoms at the corners of the unit cell and 2 S atoms inside the unit cell. The Sn shares its atom with 4 adjacent unit cells in the monolayer, thus, according to solid state physics [71], Sn contributes only ¼ of its atom to the unit cell. Since there are 4 Sn atoms, their contribution altogether give one Sn atom in the unit cell. The 2 S atoms in the unit cell contribute a whole atom each, hence the stoichiometry is SnS_2. The 2H-Polytype structure, figure 1.3 (a), has S atoms directly on top and below one another, while the 1T-Polytype structure, figure 1.3 (b), has S atoms also on top and below each other, but diagonally across each other in the unit cell. Each SnS_2 monolayer consists of a sheet of Sn atoms sandwiched between two sheets of S atoms. The 1T-SnS_2 is the more chemically stable of the two [67, 70]. Therefore, a high concentration of 1T-SnS_2 will be formed during synthesis [72].

As much as SnS_2 meets the requirements of a 2D photoelectrode for WS, there are some challenges facing it, such as: insufficient performance at low sunlight intensities and improper band alignment [39, 64, 73]. O_2/H_2O is the potential at which water is oxidized to synthesize oxygen and H^+/H_2 is the potential at which water is reduced to synthesize hydrogen [39]. A band edge alignment diagram is a comparison of the valence band maximum (VBM) energy and conduction band minimum (CBM) energy of a material, relative to O_2/H_2O and H^+/H_2. For overall water splitting, the CBM should be above

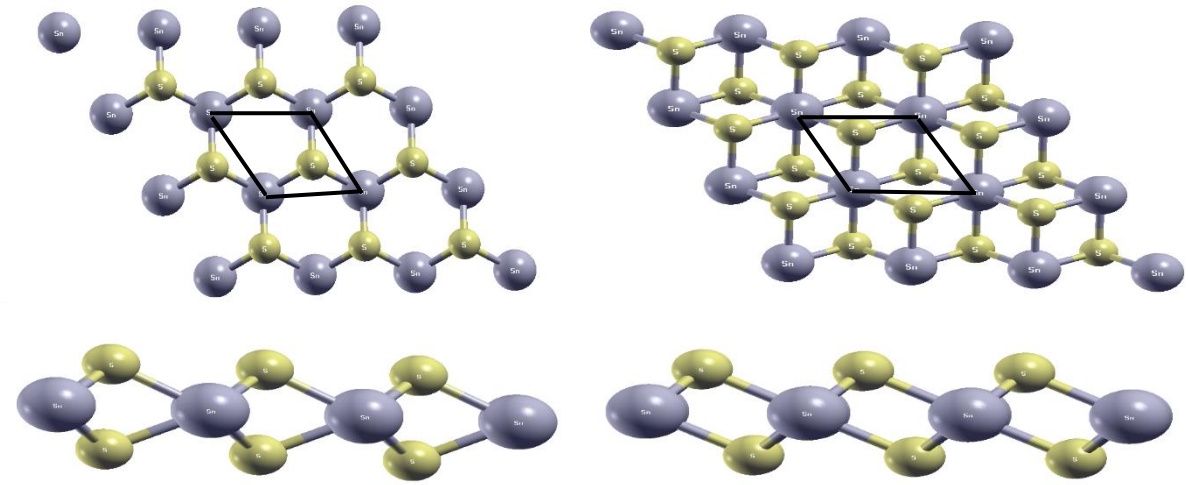

(a) (b)

Figure 1.3: Top and side view of (a) 2H-Polytype SnS_2 and (b) 1T-Polytype SnS_2. The rhombic structure on the top views indicates the unit cell for both structures.

H^+/H_2, thus water is reduced to produce hydrogen, and VBM should be below O_2/H_2O, thus water is oxidized to produce oxygen [39, 40]. A photo-excited electron from the VB will reduce water (H^+/H_2) while jumping to the CB [66]. An electron from the anion OH^- will be received at the VBM which will be at a lower energy than (O_2/H_2O) [66]. For an electron, a lower energy signifies higher stability [74]. These processes should occur simultaneously to avoid photo-induced corrosion or degradation of the photocatalyst [39]. For, if only the CBM is above H^+/H_2, then the photocatalyst will be oxidized since it is losing its electrons in the process of hydrogen evolution. Likewise, if only the VBM is below O_2/H_2O, then the photocatalyst will be reduced as it would receive an excess of electrons in the process of oxygen evolution.

Pristine SnS_2 has a CBM below H^+/H_2 and a VBM below O_2/H_2O [60, 76], as illustrated in figure 1.4. This implies that pristine SnS_2 is only suitable for oxygen evolution, which defeats the purpose of the research, as hydrogen is the focus as an electricity producing fuel. Sainbileg et al. [75] demonstrated that doping SnS_2 engineers the CBM and VBM to be properly aligned with H^+/H_2 and O_2/H_2O for overall WS. From figure 1.4, it is observable that this technique further reduces the band gap from 2.34 eV for pristine SnS_2, to 1.97 eV for Ni-SnS_2 and 1.88 eV for Ni-SnS_2-Vs. A reduced band gap increases photocurrent, thus enhancing the photocatalyst's performance even at low sunlight

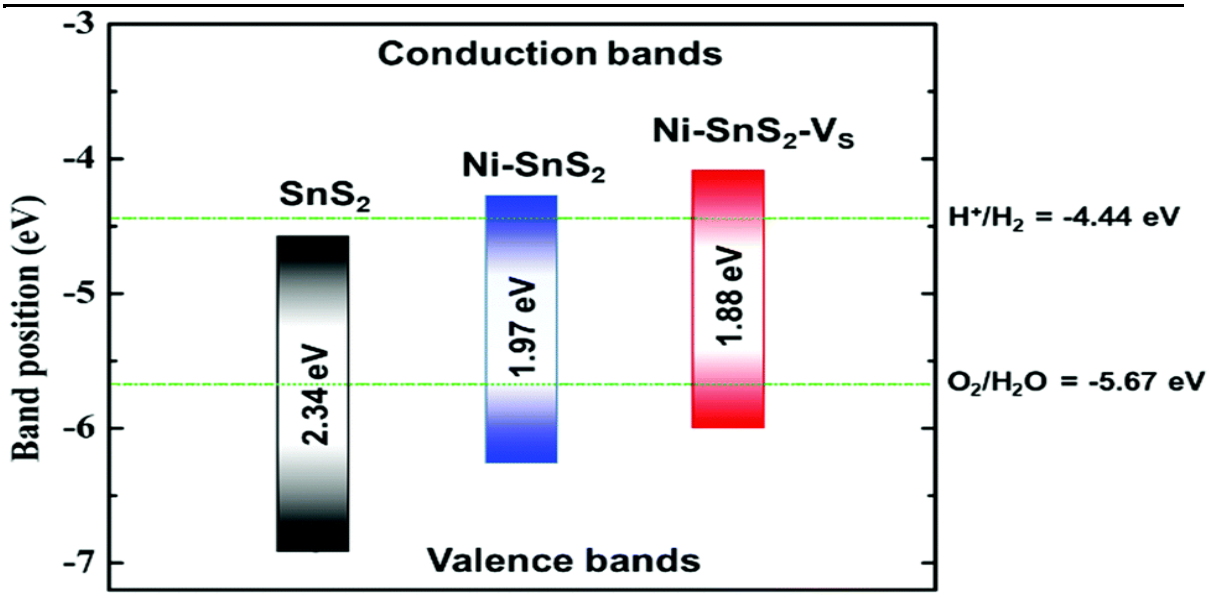

Figure 1.4: Band alignment for Pristine SnS_2 (black bar), Nickel doped SnS_2 (blue bar), and Nickel and Sulphur monovacancy doped SnS_2 (red bar) with reference to band alignment for water redox potentials. Top of the bar represents the CBM and bottom of the bar represents the VBM. The top green line crossing the bar is the water reduction potential and lower green line is the water oxidation potential [75].

intensities [64, 75, 76]. Thus, we use doping as a means to computationally engineer SnS_2 to perform at its peak for PEC WS for mass-hydrogen production to be realized.

1.3 Aims and objectives

The influence of C and Si doping of SnS_2 for enhanced PEC WS was investigated using first-principles simulations based on density functional theory (DFT) [77]. DFT calculations have received increasing attention, in the past years, for their accurate prediction at an atomistic level and good agreement with experimental results [78]. Its setback is that the exchange-correlation functionals: local density approximation (LDA) [79] and generalized gradient approximation (GGA) [80], fail to correctly predict the band gap [81]. To counteract this failure, a U constant from the Hubbard model [82] is incorporated within DFT, thus a DFT+U/GGA+U method, which is further discussed in Chapter 3. Various experimental and DFT studies have been extensively carried out on SnS_2 monolayer, which are reported in Chapter 2. However, more research is still required for commercialization of SnS_2 as a photoelectrode for WS. Doping of SnS_2 semiconductor

can effectively improve its performance to enhance hydrogen production during photoelectrolysis. The main aims and objectives of our work are:

- To determine the most suitable computational conditions for studying SnS_2 monolayer supercell (cut-off energy and k-points).
- To examine properties such as: lattice constants (a_0), bond length (d_{S-Sn}), band gap (E_g) and binding energy (Cohesive energy per atoms, $E_{Coh/atom}$).
- To study the effects of C and Si atom doping on SnS_2 monolayer supercell.
- To examine the influence of supercell sizes on the stability of the different doping configurations by calculating binding energies.
- To analyze the electronic structures of the different C and Si doped configurations from the total and partial densities of states (TDOS and PDOS, respectively).
- To examine the influence of C and Si doping of SnS_2 on the band gap size and intermediate states induced by the impurity states.
- Perform charge density difference plots to investigate the influence of the C and Si dopant on the charge distribution among host atoms.
- To examine C and Si doped SnS_2 with regards to their CBM and VBM alignment with respect to redox potentials of water.

1.4 Outline of dissertation

In this dissertation, Chapter 2 focuses on the previous studies of pristine and doped SnS_2 monolayer. Doping studies have been done using experimental and DFT on improving the photocatalytic properties of SnS_2. Chapter 2 reports on the different doping studies which are, to mention a few: n- and p-type doping, co-doping, vacancy doping, ion doping, etc. Chapter 3 presents DFT methods which our calculations are simulated with. Chapter 3 also goes deeper into the exchange-correlation functionals postulated by Hartree-Fock Approximation, Hohenberg-Kohn theorems, and Kohn-Sham equations. Chapter 4 focuses on the results of calculations performed with the intentions of enhancing our champion material (SnS_2) as a photoelectrode for WS. Electronic structure, charge density differences and band alignment are simulated as argument points which lead to the conclusion on the approach of producing the best photoelectrode. Finally, Chapter 5 (conclusion), summarizes the overview of the whole study.

BIBLIOGRAPHY

[1] Goldemberg José (2007). *Ethanol for a sustainable energy future*. Science, 315(5813), pp. 808–810. Available at: https://doi.org/10.1126/science.1137013.

[2] Hannah Ritchie and Max Roser (2020). *CO_2 and Greenhouse Gas Emissions*. Available at: https://www.researchgate.net/figure/Hannah-Ritchie-and-Max-Roser-2020-CO-and-Greenhouse-Gas-Emissions-Published-online_fig4_353949059 (Accessed: February 7, 2023).

[3] Aydin, G. (2014). *The modeling and projection of primary energy consumption by the sources*. Energy Sources, Part B: Economics, Planning, and Policy, 10(1), pp. 67–74. Available at: https://doi.org/10.1080/15567249.2013.771716.

[4] Hassmann, K. and Kuhne, H. (1993). *Primary energy sources for hydrogen production*. International Journal of Hydrogen Energy, 18(8), pp. 635–640. Available at: https://doi.org/10.1016/0360-3199(93)90115-q.

[5] Wong, K.V. and Tan, N. (2015). *Feasibility of using more geothermal energy to generate electricity*. Journal of Energy Resources Technology, 137(4). Available at: https://doi.org/10.1115/1.4028138.

[6] Ma, G., Hisatomi, T. and Domen, K. (2015). *Semiconductors for photocatalytic and photoelectrochemical solar water splitting*. From Molecules to Materials, pp. 1–56. Available at: https://doi.org/10.1007/978-3-319-13800-8_1.

[7] Grätzel, M. (2001). *Photoelectrochemical cells*. Nature, 414(6861), pp. 338–344. Available at: https://doi.org/10.1038/35104607.

[8] Zohuri, B. and McDaniel, P. (2021). *Energy insight: An energy essential guide*. Introduction to Energy Essentials, pp. 321–370. Available at: https://doi.org/10.1016/b978-0-323-90152-9.00009-8.

[9] Kumar, S. and Jan, J.M. (2013). *Research Collaboration Networks of two OIC Nations: Comparative Study between Turkey and Malaysia in the field of 'energy fuels', 2009–2011*. *Scientometrics*, 98(1), pp. 387–414. Available at: https://doi.org/10.1007/s11192-013-1059-8.

[10] Dicks, J. (1978). *Electricity from coal by the MHD process*. 14th Annual Meeting and Technical Display [Preprint]. Available at: https://doi.org/10.2514/6.1978-291.

[11] Bohning, L., Herget, M. and Schwalbe, U. (2021). *Investigation of Energy Storage Systems - improvement of utilization by use case combination*. 2021 Ural-Siberian Smart Energy Conference (USSEC) [Preprint]. Available at: https://doi.org/10.1109/ussec53120.2021.9655735.

[12] Ma, C.-T. and Hsieh, C.-L. (2020). *Investigation on hybrid energy storage systems and their application in Green Energy Systems*. Electronics, 9(11), p. 1907. Available at: https://doi.org/10.3390/electronics9111907.

[13] Węcel, D. *et al.* (2020). *Investigation on system for renewable electricity storage in small scale integrating photovoltaics, batteries, and hydrogen generator*. Energies, 13(22), p. 6039. Available at: https://doi.org/10.3390/en13226039.

[14] Edwards, P.P., Kuznetsov, V.L. and David, W.I.F. (2007). *Hydrogen Energy*. Philosophical Transactions of the Royal Society A: Mathematical, Physical and Engineering Sciences, 365(1853), pp. 1043–1056. Available at: https://doi.org/10.1098/rsta.2006.1965.

[15] Benemann, J. (1996). *Hydrogen biotechnology: Progress and prospects*. Nature Publishing Group, 14.

[16] Song, H. *et al.* (2022). *Solar-driven hydrogen production: Recent advances, challenges, and future perspectives*. ACS Energy Letters, 7(3), pp. 1043–1065. Available at: https://doi.org/10.1021/acsenergylett.1c02591.

[17] Song, X., Wei, G., Sun, J. *et al.* (2020). *Overall photocatalytic water splitting by an organolead iodide crystalline material*. Nat Catal **3**, 1027–1033. https://doi.org/10.1038/s41929-020-00543-4.

[18] Lubitz, W. and Tumas, W. (2007). *Hydrogen: an overview*. Chemical Reviews, 107(10), pp. 3900–3903. Available at: https://doi.org/10.1021/cr050200z.

[19] Crowl, D.A. and Jo, Y.-D. (2007). *The hazards and risks of hydrogen*. Journal of Loss Prevention in the Process Industries, 20(2), pp. 158–164. Available at: https://doi.org/10.1016/j.jlp.2007.02.002.

[20] Brescia, Arents, Turk et al. (1975). *Fundamentals of Chemistry*. 3rd edn, pp. 41–45.

[21] Sharma, S. and Ghoshal, S.K. (2015). *Hydrogen the future transportation fuel: From production to applications*. Renewable and Sustainable Energy Reviews, 43, pp. 1151–1158. Available at: https://doi.org/10.1016/j.rser.2014.11.093.

[22] Ball, M. and Wietschel, M. (2009). *The future of hydrogen – opportunities and challenges*. International Journal of Hydrogen Energy, 34(2), pp. 615–627. Available at: https://doi.org/10.1016/j.ijhydene.2008.11.014.

[23] Rievaj, V., Gaňa, J. and Synák, F. (2019). *Is hydrogen the fuel of the future?* Transportation Research Procedia, 40, pp. 469–474. Available at: https://doi.org/10.1016/j.trpro.2019.07.068.

[24] Peavey, M.A. (2008). "Chapter 2," in *Fuel from water: Energy Independence with hydrogen*. Louisville, KY: Merit Inc.

[25] Holladay, J.D. *et al.* (2009). *An overview of hydrogen production technologies*. Catalysis Today, 139(4), pp. 244–260. Available at: https://doi.org/10.1016/j.cattod.2008.08.039.

[26] Naya, K. and Okada, F. (2012). *Effects of NaCl and Na_2SO_4 cathode electrolytes on electrochemical ozone production*. Electrochimica Acta, 78, pp. 495–501. Available at: https://doi.org/10.1016/j.electacta.2012.06.071.

[27] Eggen, P.-O. and Kvittingen, L. (2004). *A small-scale and low-cost apparatus for the electrolysis of water*. Journal of Chemical Education, 81(9), p. 1337. Available at: https://doi.org/10.1021/ed081p1337.

[28] Schmitt, R.W. (1995). *The ocean component of the Global Water Cycle*. Reviews of Geophysics, 33(S2), pp. 1395–1409. Available at: https://doi.org/10.1029/95rg00184.

[29] Spurgeon, J.M. and Lewis, N.S. (2011). *Proton exchange membrane electrolysis sustained by water vapor*. Energy & Environmental Science, 4(8), p. 2993. Available at: https://doi.org/10.1039/c1ee01203g.

[30] Dekel, D.R. (2018). *Review of cell performance in anion exchange membrane fuel cells*. Journal of Power Sources, 375, pp. 158–169. Available at: https://doi.org/10.1016/j.jpowsour.2017.07.117.

[31] Wang, Y. *et al.* (2011). *A review of polymer electrolyte membrane fuel cells: Technology, applications, and needs on fundamental research*. Applied Energy, 88(4), pp. 981–1007. Available at: https://doi.org/10.1016/j.apenergy.2010.09.030.

[32] Rajendran, R.G. (2005). *Polymer electrolyte membrane technology for fuel cells*. MRS Bulletin, 30(8), pp. 587–590. Available at: https://doi.org/10.1557/mrs2005.165.

[33] Zaidi, S.M. and Matsuura, T. (2008). *Polymer Membranes for Fuel Cells*. 1st edn. Springer New York, NY. (ISBN: 978-0-387-73531-3).

[34] Batsanov, S.S. (2007). *Ionization, atomization, and bond energies as functions of distances in inorganic molecules and Crystals*. Russian Journal of Inorganic Chemistry, 52(8), pp. 1223–1229. doi:10.1134/s0036023607080128.

[35] Turner, J.A. (2004). *Sustainable hydrogen production*. Science, 305(5686), pp. 972–974. Available at: https://doi.org/10.1126/science.1103197.

[36] Ramachandran, R. (1998). *An overview of industrial uses of hydrogen*. International Journal of Hydrogen Energy, 23(7), pp. 593–598. Available at: https://doi.org/10.1016/s0360-3199(97)00112-2.

[37] *Fuel cell - Energy Education*. Available at: https://energyeducation.ca/encyclopedia/Fuel_cell (Accessed: February 13, 2023).

[38] Marzo, L. *et al.* (2018). *Visible-light photocatalysis: Does it make a difference in organic synthesis?* Angewandte Chemie International Edition, 57(32), pp. 10034–10072. Available at: https://doi.org/10.1002/anie.201709766.

[39] Chen, S. and Wang, L.-W. (2012). *Thermodynamic oxidation and reduction potentials of photocatalytic semiconductors in aqueous solution*. Chemistry of Materials, 24(18), pp. 3659–3666. Available at: https://doi.org/10.1021/cm302533s.

[40] Maeda, K. (2011). *Photocatalytic water splitting using semiconductor particles: History and recent developments*. Journal of Photochemistry and Photobiology C: Photochemistry Reviews, 12(4), pp. 237–268. Available at: https://doi.org/10.1016/j.jphotochemrev.2011.07.001.

[41] Liu, B., Abbas, A. and Zhou, C. (2017). *Two-dimensional semiconductors: From materials preparation to electronic applications*. Advanced Electronic Materials, 3(7), p. 1700045. Available at: https://doi.org/10.1002/aelm.201700045.

[42] Polyushkin, D.K. *et al.* (2020). *Analogue two-dimensional semiconductor electronics*. Nature Electronics, 3(8), pp. 486–491. Available at: https://doi.org/10.1038/s41928-020-0460-6.

[43] Roy, P.K., Luxa, J. and Sofer, Z. (2020). *Emerging Pnictogen-based 2D semiconductors: Sensing and electronic devices*. Nanoscale, 12(19), pp. 10430–10446. Available at: https://doi.org/10.1039/d0nr02932g.

[44] Shivananju, B.N. *et al.* (2019). *Optical biochemical sensors based on 2D materials*. Fundamentals and Sensing Applications of 2D Materials, pp. 379–406. Available at: https://doi.org/10.1016/b978-0-08-102577-2.00010-5.

[45] Cheng, Z. *et al.* (2016). *Carbon dots decorated vertical SnS_2 nanosheets for efficient photocatalytic oxygen evolution*. Applied Physics Letters, 109(5), p. 053905. Available at: https://doi.org/10.1063/1.4960527.

[46] Diko, C.S. *et al.* (2022). *Synthesis and applications of dimensional SnS_2 and SnS_2/carbon nanomaterials*. Nanomaterials, 12(24), p. 4497. Available at: https://doi.org/10.3390/nano12244497.

[47] Thoma, S., Grohens, Y. and James, J. (eds) (2020). "Chapter 9," in *Nano-Optics: Fundamentals, Experimental Methods and Applications*. Elsevier Inc.

[48] Mir, S.H., Yadav, V.K. and Singh, J.K. (2020). *Recent advances in the carrier mobility of two-dimensional materials: A theoretical perspective*. ACS Omega, 5(24), pp. 14203–14211. Available at: https://doi.org/10.1021/acsomega.0c01676.

[49] Fan and Fudong (2019). *Band Gap*. Encyclopedia Britannica.

[50] Makuła, P., Pacia, M. and Macyk, W. (2018). *How to correctly determine the band gap energy of modified semiconductor photocatalysts based on UV–vis spectra*. The Journal of Physical Chemistry Letters, 9(23), pp. 6814–6817. Available at: https://doi.org/10.1021/acs.jpclett.8b02892.

[51] Juster, N.J. (1963). *Conduction and semiconduction.* Journal of Chemical Education, 40(9), p. 489. Available at: https://doi.org/10.1021/ed040p489.

[52] Liang, Q. *et al.* (2020). *Oxygen-induced controllable P-type doping in 2D semiconductor transition metal dichalcogenides*. Nano Research, 13(12), pp. 3439–3444. Available at: https://doi.org/10.1007/s12274-020-3038-8.

[53] Pfeiffer, M. *et al.* (2003). *Doped Organic Semiconductors: Physics and application in Light Emitting Diodes*. Organic Electronics, 4(2-3), pp. 89–103. Available at: https://doi.org/10.1016/j.orgel.2003.08.004.

[54] Laks, D.B. *et al.* (1991). *Role of native defects in wide-band-gap semiconductors*. Physical Review Letters, 66(5), pp. 648–651. Available at: https://doi.org/10.1103/physrevlett.66.648.

[55] Brownlie, L. and Shapter, J. (2018). *Advances in carbon nanotube N-type doping: Methods, analysis and applications*. Carbon, 126, pp. 257–270. Available at: https://doi.org/10.1016/j.carbon.2017.09.107.

[56] Wahnón, P. *et al.* (2011). *V-doped SnS_2: A new intermediate band material for a better use of the solar spectrum*. Physical Chemistry Chemical Physics, 13(45), p. 20401. Available at: https://doi.org/10.1039/c1cp22664a.

[57] Haus, J.W. (2016). "11.2.2 Density of states," in *Fundamentals and Applications of Nanophotonics*. Elsevier Ltd.

[58] Magero, D. *et al.* (2017). *Partial density of states ligand field theory (pdos-LFT): Recovering a LFT-like picture and application to photoproperties of ruthenium(ii) polypyridine complexes*. Journal of Photochemistry and Photobiology A: Chemistry, 348, pp. 305–325. Available at: https://doi.org/10.1016/j.jphotochem.2017.07.037.

[59] Britannica, T. Editors of Encyclopaedia (2006, October 6). *Fermi level*. *Encyclopedia Britannica*. https://www.britannica.com/science/Fermi-level.

[60] Zhuang, H.L. and Hennig, R.G. (2013). *Theoretical perspective of photocatalytic properties of single-layer SnS_2*. Physical Review B, 88(11). Available at: https://doi.org/10.1103/physrevb.88.115314.

[61] Zhang, J. *et al.* (2012). *Development of visible light-responsive photocatalysts*. International Journal of Photoenergy, 2012, pp. 1–4. Available at: https://doi.org/10.1155/2012/280297.

[62] Burton, L.A. *et al.* (2016). *Electronic and optical properties of single crystal SnS_2: An Earth-abundant disulfide photocatalyst*. Journal of Materials Chemistry A, 4(4), pp. 1312–1318. Available at: https://doi.org/10.1039/c5ta08214e.

[63] Tan, F. *et al.* (2011). *Preparation of SnS_2 colloidal quantum dots and their application in organic/inorganic hybrid solar cells*. Nanoscale Research Letters, 6(1). Available at: https://doi.org/10.1186/1556-276x-6-298.

[64] Sun, Y., Cheng, H., Gao, S., et al. (2012). *Freestanding Tin Disulfide Single-Layers Realizing Efficient Visible-Light Water Splitting*. Angewandte Chemie International Edition, 51(35), pp.8727-8731.

[65] Shown, I., Samireddi, S., Chang, Y., Putikam, R., Chang, P., Sabbah, A., Fu, F., Chen, W., Wu, C., Yu, T., Chung, P., Lin, M., Chen, L. and Chen, K., 2018. *Carbon-doped SnS_2 nanostructure as a high-efficiency solar fuel catalyst under visible light*. Nature Communications, 9(1).

[66] Chen, L. *et al.* (2019). *Two-dimensional SnS_2 nanosheets arrays as photoelectrode by low temperature CVD method for efficient photoelectrochemical water splitting*. Applied Surface Science, 467-468, pp. 698–707. Available at: https://doi.org/10.1016/j.apsusc.2018.10.199.

[67] Wei, R. *et al.* (2014). *Ultrathin SnS_2 nanosheets with exposed {001} facets and enhanced photocatalytic properties*. Acta Materialia, 66, pp. 163–171. Available at: https://doi.org/10.1016/j.actamat.2013.11.076.

[68] Yu, D., Liu, Y., Sun, L., Wu, P. and Zhou, W. (2016). *Density functional study on the hole doping of single-layer SnS2 with metal element X (X = Li, Mg, and Al)*. Phys. Chem. Chem. Phys., 18(1), pp.318-324.

[69] Xiong, Z. *et al.* (2021). *Structural defects, mechanical behaviors, and properties of two-dimensional materials*. Materials, 14(5), p. 1192. Available at: https://doi.org/10.3390/ma14051192.

[70] Scalise, E. and Houssa, M. (2017). *Predicting 2D silicon allotropes on SnS_2*. Nano Research, 10(5), pp. 1697–1709. Available at: https://doi.org/10.1007/s12274-016-1409-y.

[71] Sigrist, M. (2014). *Solid State Theory*. [online] Edu.itp.phys.ethz.ch. Available at: <https://edu.itp.phys.ethz.ch/fs14/sst/Lecture-Notes.pdf> [Accessed 11 October 2022].

[72] Mabiala-Poaty, H., Douma, D., M'Passi-Mabiala, B. and Mapasha, R. (2018). *Structural and electronic properties of SnS_2 stacked nanosheets: An ab-initio study*. Journal of Physics and Chemistry of Solids, 120, pp.211-217.

[73] Tian, Z. *et al.* (2019). *Solar-driven capacity enhancement of aqueous redox batteries with a vertically oriented tin disulfide array as both the photo-cathode and battery-anode*. Chemical Communications, 55(9), pp. 1291–1294. Available at: https://doi.org/10.1039/c8cc08684b.

[74] Dudarev, S.L. *et al.* (1998). *Electron-energy-loss spectra and the structural stability of nickel oxide: an LSDA+U study*. Physical Review B, 57(3), pp. 1505–1509. Available at: https://doi.org/10.1103/physrevb.57.1505.

[75] Sainbileg, B. *et al.* (2019). *The dual-defective SnS_2 monolayers: Promising 2D photocatalysts for overall water splitting*. Physical Chemistry Chemical Physics, 21(48), pp. 26292–26300. Available at: https://doi.org/10.1039/c9cp04649f.

[76] Zhu, X. *et al.* (2018). *Band Gap Engineering of SnS_2 nanosheets by anion–anion codoping for visible-light photocatalysis*. RSC Advances, 8(6), pp. 3304–3311. Available at: https://doi.org/10.1039/c7ra12058c.

[77] Payne, M., Teter, M., Allan, D., Arias, T. and Joannopoulos, J. (1992). *Iterative minimization techniques for ab initio total energy: molecular dynamics and conjugate gradients*. Review of modern physics, 64, pp.1040-1050.

[78] Kohanoff, J. and Gidopoulos, N., 2003. *Density Functional Theory: Basics, New Trends and Applications*. 2nd ed. Handbook of molecular physics and quantum chemistry, pp.532-568.

[79] Dirac, P. (1930). *Note on Exchange Phenomena in the Thomas Atom*. Mathematical Proceedings of the Cambridge Philosophical Society, 26(3), pp.376-385.

[80] Shul'man, A. and Posvyanskii, D., 2014. *Truly self-consistent solution of Kohn-Sham equations for extended systems with inhomogeneous electron gas*. Journal of Physics: Conference Series, 510, p.012029.

[81] Bhavani, J. and John, R., 2020. *Band Gap Engineering of Cu_2ZnSnX_4 (X = S, Se and Te) Quaternary Semiconductors Using PBE-GGA, TB-mBJ and mBJ+U Potentials*. International Journal of Materials, Mechanics and Manufacturing, 8(1).

[82] Hubbard, J., 1967. *Electron correlations in narrow energy bands VI. The connexion with many-body perturbation theory*. Proceedings of the Royal Society of London. Series A. Mathematical and Physical Sciences, 296(1444), pp.99-118.

CHAPTER 2: LITERATURE REVIEW

2.1 Brief introduction

Considerable studies have been performed on SnS_2 monolayer as a valuable material in optoelectronic applications and more specifically for photo-induced water splitting [1, 2, 3]. SnS_2 is a 2D semiconductor that is made of abundant elements, has a band gap suitable for photocatalytic applications and is stable in aqueous solutions [2, 3]. Experimental and *Ab initio* studies have shown that SnS_2 has band alignments which are not suitable for overall water splitting and hinders its ability for hydrogen production [4, 5]. Considerable studies have indicated that the doping method with different atoms tends to improve photocatalytic properties of SnS_2 monolayer [1, 4, 5]. Below are reviews of doped SnS_2 monolayer summarizing the positive and negative effects of dopants.

2.2 Experimental and theoretical studies on pristine single-layer SnS_2

Sun *et al.* [1] experimentally studied SnS_2 single-layer photoelectrode and compared its properties to those of bulk SnS_2 in order to determine its efficiency as a photocatalyst for water splitting. The photeloectrode was fabricated through spin-coating ethanol dispersions of SnS_2 multi-layers onto an indium-tin-oxide (ITO) coated glass. To investigate the photoelectrochemical cell water splitting abilities, a 0.5 Molar Na_2SO_4 electrolyte was used in a three-electrode setup with a visible-light irradiation source from a 300W Xe lamp. Photocurrent density measurement for the SnS_2 single-layer was 2.75 mAcm^{-2} and this was roughly 72 times greater than that for the bulk SnS_2. Incident photon-to-current conversion efficiency (IPCE) [1] measurements showed a conversion of 38.7% at 420 nm for SnS_2 single-layers, which was higher than the 2.33% for bulk SnS_2. Moreover, the

IPCE of 38.7% for SnS_2 single-layers was higher than most existing reports, according to Sun *et al.*, the calculated electron density of SnS_2 single-layer was $5.87 \times 10^{19} cm^{-3}$, roughly 40 times greater than $1.48 \times 10^{18} cm^{-3}$ for bulk material. Thus, SnS_2 monolayer facilitated higher charge transport at the interfaces. Importantly as well, the photocurrent density of SnS_2 monolayer had negligible variations even after 3600s of irradiation, contrastingly, bulk SnS_2 displayed serious current vs time (I-t) fluctuations. These observations clearly highlight the remarkable photostability of SnS_2 monolayer and point to SnS_2 monolayer as one of the best currently known photocatalyst.

Zhuang *et al.* [2] performed an *Ab initio* study on the photocatalytic properties of pristine single-layer SnS_2. Sun *et al.* [1] have determined from experiments that single-layer materials have more photocatalytic advantages than bulk materials. Zhuang *et al.* performed a density functional theory (DFT) calculation with Projector-Augmented-Wave (PAW) method implemented in the Vienna *Ab initio* Simulation Package (VASP) code [6, 7]. Perdew-Burke-Ernzerhof (PBE) functionals with the Generalized Gradient Approximation (GGA) were used for structural relaxation and Heyd-Scuseria-Ernzerhof (HSE06) hybrid functional were also used for band gap calculations. The band gap (E_g) of monolayer SnS_2 monolayer was calculated to be 2.75 eV, thus within the mandatory photocatalytic range of 1.7 – 3.0 eV [8]. To determine the conditions under which SnS_2 monolayer can perform photoelectrochemical water splitting, the band edge positions were calculated and compared to the vacuum levels for water redox potentials. The VBM was below O_2/H_2O, thus energetically favourable to drive oxygen evolution and CBM was below H^+/H_2, thus inadequate to drive hydrogen evolution. Therefore to overcome this challenge, a number of band gap modification techniques can be adopted, such as: Applying an external bias potential, interface engineering, doping, etc. [9, 10, 11].

2.3 Experimental and theoretical studies on doping bulk and single-layer SnS_2 for photocatalytic applications

2.3.1 Singular atom, ion and nanoparticle doping

Shown *et al.* [12] studied carbon doped SnS_2 (denoted as SnS_2-C) for photocatalytic CO_2 reduction to form acetaldehyde, using a Photoelectrochemical Cell (PEC). Carbon doped

SnS_2 nanostructure was experimentally synthesized using L-cysteine-based hydrothermal process [13]. It was noted that the carbon doped SnS_2 had a significantly smaller band gap compared to pristine SnS_2 and also exhibited higher photon absorption ranging from visible light towards longer wavelengths. A DFT study, using VASP, was also performed for carbon doped SnS_2. The following structures were considered: (a) Carbon substituting a sulphur atom ($C_{S\text{-}S}$) and (b) Carbon placed at an interstitial position (C_{int}). The structure, $C_{int,}$ has a lower formation energy than $C_{S\text{-}S}$, thus C_{int} is more experimentally synthesizable than $C_{S\text{-}S}$. Furthermore, it was found that CO_2 adsorbed on the $C_{S\text{-}S}$ structure has a binding energy of $25.0\ kcal.mol^{-1}$, whereas CO_2 adsorbed on the C_{int} structure has a binding energy of $10.2\ kcal.mol^{-1}$. The photoreaction results indicate that acetaldehyde formation on carbon doped SnS_2 is almost 250 times higher than that formed on pristine SnS_2. Further experiments showed that the absence of CO_2 and light irradiation resulted in the absence of acetaldehyde detection. Therefore, it was concluded that carbon doped SnS_2 demonstrated enhanced photocatalytic performance and successfully reduced CO_2 to solar fuels or hydrocarbons. This could be an approach to combat global warming by reducing amount of CO_2 in the atmosphere in a similar way that plants naturally perform photosynthesis.

Wang *et al.* [14] investigated the effectiveness of Carbon-Quantum-Dots (CQDs) doped SnS_2 for harvesting oxygen using photocatalytic processes. SnS_2 nanosheets were grown experimentally, using solvothermal method [15], onto Fluorine doped Tin Oxide glass (FTO), with a 10nm layer of nickel (Ni). Thereafter, CQDs of size 10nm were integrated on the SnS_2 nanosheet and the composite is known as FTO-Ni-SnS_2-CQDs (FNSC) photoelectrode. It was observed that strong light absorption leading to enhanced photocurrent density resulted after Carbon Dots were integrated onto the SnS_2 nanosheet. FNSC exhibited high efficiency and highest rate of oxygen evolution compared to the FTO electrode with pristine SnS_2 monolayer alone. CQDs enhance light absorption thereby increasing photocurrent required for Oxygen evolution [14]. Long-term test cycles predict the potential of using this doping technique on a large scale.

Conesa *et al.* [16] contributed towards improving photocurrent of SnS_2 through doping with Vanadium (V) atom. In this work, the V-doped SnS_2 was synthesized experimentally using solution method [16] and theoretically using DFT employing GGA. Lattice values of the pristine and V-doped SnS_2 structures were obtained using X-Ray fluorescence [16].

Theoretically, the doping was accomplished through replacing two Sn atoms with two V atoms in a monolayer supercell containing 8 Sn atoms and 16 S atoms, leading to a composite supercell of $V_2Sn_6S_{16}$. These two techniques were in good agreement in predicting structural parameters, but differed slightly in predicting the band gap, with $E_g = 2.2eV$ for experimental and $E_g = 1.37eV$ for DFT GGA. The lattice constants and bond lengths are lower in V-doped SnS_2 than in pristine SnS_2. Conesa *et al.* attributed this to V atom having a larger atomic radius and therefore it approaches the S atom more than Sn atom did. Density of Sates (DOS) and Band Structure analysis of the V-doped material revealed an Intermediate Band (IB) which had no overlap with the CB or VB. The IB increased the overall photocurrent density of the material. The absorption coefficient spectrum comparing both SnS_2 and $V_2Sn_6S_{16}$ structure showed that the latter exhibited higher absorption features appearing at energy lower than 2.2 eV, in agreement with DFT. Thus, V-doped SnS_2 indicated new channels for photons with energies much below band gap of SnS_2. In conclusion, V doping of SnS_2 enhanced photocatalytic performance of the pristine SnS_2 through the introduction of the IB.

Wu *et al.* [17] reported different types of band gap engineering through doping SnS_2 with Iron (Fe). This study was based on DFT done in VASP using PAW pseudopotentials. Atoms were fully relaxed using GGA PBE functional and band gap calculations were acquired using the GGA+U method with a U value of 9.0 eV. For the van der Waals interactions, the Grimme's DFT-D2 method was used. The electronic structure of Fe-doped SnS_2 was investigated for five different Fe doping concentrations of $Sn_{1-x}Fe_xS_2$ (x = 0%, 5.56%, 6.25%, 8.33% and 12.50%). To achieve these concentrations, one Sn atom was replaced by the Fe atom in five different SnS_2 monolayer supercell sizes. Doping concentration of x = 0% is the un-doped pure SnS_2. The lattice parameters were calculated for the different concentrations and it was observed that an increase in Fe doping concentration lead to a decrease in the lattice parameters. Wu *et al.* attributed this to the difference in bond lengths of the Sn-S (longer) and Fe-S (shorter) bonds. The band gaps for the different concentrations were also calculated and displayed a decreasing trend with an increasing Fe doping concentrations. For pure SnS_2, the VBM is exactly at the Fermi level and when doped with Fe, the Fermi level shifts into the Valence Band. Thus, this could be a strategy for raising the VBM when modifying the band gap of the SnS_2 photocatalyst.

Yu *et al.* [18] studied the effects of cation doping on the photocatalytic water splitting properties of SnS_2 monolayer. All calculations were performed with DFT using a VASP code which employed GGA+U approach with an on-site coulomb interaction of U = 9 eV, for band gap calculations. Cation doping in single-layer SnS_2 supercell was accomplished by substituting the Sn atom by one X atom, denoted as SnS_2:X for X = Li, Mg or Al. To investigate the binding nature of SnS_2:X, the charge density difference near the dopant X was simulated. A covalent bond exists between Sn and S atoms [19, 20] and therefore a normal charge distribution was observed for pure SnS_2. Cation doping introduces holes in SnS_2. Thus, electron density close to the dopant reduces, thereby inducing an ionic bond. Therefore, the covalent property of X-S bond gradually decreases and its iconicity gradually increases with increasing hole density of the X-dopant. Thermodynamic stability analysis showed that formation energies (E_f) are lower under S-rich condition than Sn-rich condition for all doping cases. Also a decreasing trend in E_f with decreasing hole density of the dopant impurity was observed in the order of $E_f^{Li} > E_f^{Mg} > E_f^{Al}$. TDOS showed that for Li and Mg doping, the Fermi level (E_F) penetrated into the VB, which indicated p-type doping. Al-doped SnS_2 induced defect states in the band gap. It is seen from the band alignment diagram that the VBM for pristine SnS_2 is below oxidation potential H_2O/O_2, while CBM lies below the reduction potential H^+/H_2. This implies that pure singe-layer SnS_2 is only feasible for oxygen evolution, but not hydrogen evolution. Similarly for SnS_2:Mg(Al), the VBM lies below the water oxidation level (H_2O/O_2) and CBM also lies below the reduction level (H^+/H_2). For Li-doped SnS_2, the VBM lies below oxidation level of water and CBM is about 0.03 eV above the water reduction potential. This implies that Li-doped SnS_2 is efficient in both photo-oxidation and photo-reduction of water. According to Yu *et al.*, cation doping is easily realized than anion doping, a phenomenon also reported by Zhu *et al.* [4].

Xia *et al.* [21] proved that controlled n- and p-type doping of SnS_2 is an essential constituent for electronic and optoelectronic applications. This study was performed using spin-polarized DFT implemented in VASP which employed the PAW pseudopotential to describe the electron-hole potential. The n- and p-type doping of SnS_2 was simulated through substituting the S atom in the $4 \times 4 \times 1$ SnS_2 supercell with group VII (F, Cl, Br and I) and group V (N, P and As) atoms, respectively. The GGA+U was used for correct band gap predictions. TDOS and PDOS calculations were used to investigate the electronic

structure of the n- and p-type doped SnS_2. It was noted that for n-type (group VII) substitution, the spin-up and spin-down DOS are symmetric thus this system has a non-magnetic ground state. TDOS of p-type (group V) substitution, are asymmetric thus this system has a magnetic ground state. The formation energies for all doped cases are lower under Sn-rich condition than under S-rich condition. In particular, n-type doping has negative formation energies meaning it is more thermodynamically favourable. Furthermore, the formation energy increases as the impurity atomic size also increases which makes the formation energy of Fluorine doped SnS_2 the smallest. Numerical results pointed out that group V impurities can be considered deep acceptor doping [21], thus ineffective choices for p-type conductivity in SnS_2. It was concluded that F-doped SnS_2 was the most certain n-type donor impurity for SnS_2-based applications in electronic and optoelectronic devices.

Liang *et al.* [9] conducted a theoretical study to investigation whether Zn-doped SnS_2 accomplishes higher visible-light driven photocatalysis than pristine SnS_2. Liang *et al.* conducted this study by substituting Sn atom with Zn atom (Zn_{Sn}) using the DFT approach. The influence of Zn concentration on doped SnS_2 was investigated by considering three different SnS_2 monolayer supercells ($4 \times 4 \times 1, 3 \times 4 \times 1$ and $3 \times 3 \times 1$) which correspond to doping concentrations (6.25%, 8.33% and 11.11%). The GGA+U approach was used for the band gap prediction with U = 9.0 eV for S-4d states and U = 4.6 eV for Zn-3d states. Zn_{Sn} is favourably formed under S-rich conditions. Band structure calculations showed that monolayer SnS_2 has an indirect gap of approximately 2.23 eV. The TDOS analysis of Zn_{Sn} shows that the VBM extends towards the CBM causing the Fermi level to penetrate into the VB. This resulted in a decreased band gap of 1.84 eV. Band edge positions for Zn_{Sn} were studied and compared to those of pure SnS_2. As is reported by other literatures, pristine SnS_2 monolayer is only energetically favourable for oxygen evolution. For Zn-doped SnS_2, the VBM is below the oxidation potential O_2/H_2O and CBM is about 0.22 eV above the reduction potential H^+/H_2. Therefore, Zn-doped SnS_2 is efficient for photocatalytic water splitting.

Cho *et al.* [22] experimentally investigated Mg-doped SnS_2 for water splitting. The hydrothermal method [23] was used to synthesize the 2D few-layered Mg-doped SnS_2 ($Sn_{1-x}Mg_xS_2$) nanosheets. The photoelectrodes of both the pristine SnS_2 and $Sn_{1-x}Mg_xS_2$

were composed by drop casting onto indium tin oxide (ITO) glass. Types of investigations and measurements done for $Sn_{1-x}Mg_xS_2$ nanosheets were structural, optical and PEC properties. Quantitative analysis of a great number of nanosheets done by EDS [24] showed that Mg was present at a ratio of 1.87%≈2%, hence Mg-doped SnS_2 in this article was represented as $Sn_{0.98}Mg_{0.02}S_2$. Transmission Electron Microscopy (TEM) [24] images clearly revealed that $Sn_{0.98}Mg_{0.02}S_2$ has an indistinguishable CDI_2 type (1T-Polytype) [25] structural morphology. The band gap values for pristine SnS_2 and $Sn_{0.98}Mg_{0.02}S_2$ were measured to be 2.26 and 2.17 eV, respectively. Thus, doping SnS_2 with Mg does reduce the band gap. PEC performance of the two photoelectrodes were investigated in 1 Molar NaOH electrolyte using the conventional three-electrode setup [22]. The photocurrent density of $Sn_{0.98}Mg_{0.02}S_2$ at 1.5 V was 1.38 mA/cm^2, which is approximately 1.7 fold higher than 0.79 mA/cm^2, the photocurrent density of pristine SnS_2. The I-t curve measurements, for both pristine SnS_2 and $Sn_{0.98}Mg_{0.02}S_2$, exhibited good photostability even after 100 min of irradiation. These results conclude that both pristine SnS_2 and $Sn_{0.98}Mg_{0.02}S_2$ are suitable for photoelectrochemical water splitting. $Sn_{0.98}Mg_{0.02}S_2$ is a better of the two photocatalysts because of its high photoelectric conversion efficiency and low band gap. Photoluminescence results reveal a red shift in $Sn_{0.98}Mg_{0.02}S_2$, thus a wider visible-light response range compared to pure SnS_2.

Liu *et al.* [26] performed both an experimental and theoretical research on Copper (Cu) doping which introduces S vacancies to SnS_2 nanosheets (Cu/SnS_{2-x}). SnS_2 was formed using the hydrothermal method [23], using CH_4N_2S and $SnCl_4$ as reagents. Cu-doped SnS_2 was formed by initially forming CuS through the solvothermal method [15] then using the hydrothermal method to form Cu/SnS_{2-x}. Electron paramagnetic resonance (EPR) spectroscopy [27] confirm a typical signal at g = 2.003 for sulphur vacancies and no signal appearing for pure SnS_2. Consequent to abundant S vacancies, Cu/SnS_{2-x} showed a red-shift. Although SnS_2 has a hexagonal structure [20], SEM images showed that morphology of Cu/SnS_{2-x} was a flower-like structure with a uniform particle size of $\sim 1.5\mu m$. A standard three-electrode electrochemical cell, for both SnS_2 and Cu/SnS_{2-x}, was setup by submerging 0.05g of the as-prepared photocatalysts in 100 mL water containing Na_2S and Na_2SO_3. A 300W Xe lamp was irradiated at 278K and gas chromatography [28] together with thermal conductivity detector (TCD) [29, 30] were used for measuring the amount of H_2 evolved. Photocatalytic H_2 production, for pure SnS_2 and different doping amounts of

Cu, was measured. Results revealed that 5% Cu-doped SnS_2 had the highest yield of H_2 production of $1.37 mmol\, h^{-1} g^{-1}$, more than 6 times higher than $0.21 mmol\, h^{-1} g^{-1}$ for pure SnS_2. Cycling tests highlighted the impressive water splitting capacity of 5% Cu/SnS_{2-x} for constant H_2 evolution even after 12 hours of reaction. The S vacancies trap electrons which enhances charge carrier separation and ensures charges react with the water molecules rather than rapid recombination. The presence of S vacancies multiplies the number of active sites and a stable presence of S vacancies before and after photocatalytic reactions was reported. A theoretical study was also done to boost experimental findings using DFT implemented in VASP. PBE GGA was applied with a PAW potential which considered a $4 \times 4 \times 1$ supercell. The effect of Cu doping and S vacancies was examined using band structure and DOS. 5% Cu/SnS_{2-x} induced a higher VBM and an indirect band gap of 1.87 eV. The indirect smaller band gap is in agreement with experimental results that 5% Cu/SnS_{2-x} maximizes photon absorption and also increases lifetime of photoinduced carriers. Band alignment diagram shows that the CBM is above the hydrogen evolution potential H^+/H_2 and VBM is below the oxygen evolution potential O_2/H_2O. Thus, indicating that 5% Cu/SnS_{2-x} is very efficient for overall water splitting.

2.3.2 Atoms, ions, nanoparticles and vacancy co-doped studies

Zhu *et al.* [4] proved that doping SnS_2 with two different types of impurity atoms can improve its quality for effective photocatalytic performance. This study was performed with DFT employing GGA using PBE functional for structural optimisation and HSE06 for band gap estimation. A $3 \times 3 \times 1$ supercell was constructed and co-doped through Sulphur (S) atoms substitution with Nitrogen (N) and Phosphorus (P). Zhu *et al.* studied the following configurations: firstly, the two dopants substituted S atoms within the same unit cell, denoted as N-N(i), N-P(i) and P-P(i). Secondly, the dopants substituted S atoms in the same layer but in adjacent unit cells, denoted as N-N(ii), N-P(ii) and P-P(ii). The bond length N-Sn (2.203Å) is much shorter than bond length of pristine SnS_2 (2.582Å) because of stronger Coloumb interaction between N and Sn [4]. The bond length of P-Sn (2.617Å) is closer to that of pristine, but much larger than that of N-Sn and this is attributed to the larger atomic radius of the P atom compared to those of N and S atoms [4]. DOS of N-N(i),

N-N(ii), N-P(i), N-P(ii) systems showed unfilled impurity states which appear in the band gap. These configurations are therefore bad candidates for visible light photocatalysis, as these states may accelerate charge carrier recombination [4]. P-P(i) and P-P(ii) co-doped systems both have reduced band gaps of 1.62 eV and 1.29 eV respectively, and no impurity states in the band gap. Defect formation energies showed that the P-P co-doped systems had the least formation energies and the highest defect pair binding energies. Thus the P-P co-doped systems are the most experimentally feasible and the most thermodynamically stable. Moreover, P-P(ii) co-doped system is most suitable for oxygen evolution and P-P(i) is the best candidate for hydrogen evolution.

Murdachaem *et al.* [31] aimed to improve Oxygen Evolution Reaction (OER) of Single Walled Carbon Nanotube (SWCNT) through Nitrogen-doping, and Oxygen and Nitrogen co-doping. SWCNT are constructed by rolling a graphene monolayer forming a single-walled cylindrical tube structure. The SWCNTs were externally doped (i.e. doped impurity is positioned on the outer surface of the cylindrical structure) with Nitrogen (N), and Nitrogen and Oxygen (O) co-doping using DFT. Upon introduction of the Nitrogen atom, the following distortions were observed: formation of a pentagon and indentations in the system, flap opening, and radial upward puckering due to Stone-Wales defect [32, 33]. The charge analysis have shown that defects differed with different doping concentrations. The doped N pulled away electrons from the neighbouring C atom, because of its high electronegativity [34], thereby inducing a small positive charge in the adjacent C atom. This positive charge makes an excellent site for the adsorbate OH^-. The OH^- is oxidized at this site resulting in the synthesis of oxygen. Overpotentials for the Oxygen Evolution Reaction (η^{OER}) at various sites were also measured. The presence of 0.3 – 1% doped Nitrogen reduced the required OER overpotential considerably compared to pristine nanotubes [31, 35]. Therefore, O-doped and N,O co-doped nanotubes have good OER performance. This theoretical work supports the experimental work done by Davido *et al.* [15], which resulted with an excellent performance for both OER and HER of Ni-doped CNT.

Sainbileng *et al.* [36] investigated the optoelectronic properties of dual-doped SnS_2 as a method to enhance SnS_2 as a photocatalyst for water splitting. According to Sainbileng *et al.*, this was the first time a single atom dopant together with a vacancy defect are

investigated as a co-operative dual-defect. This investigation was done using DFT implemented in VASP. PBE exchange-correlation functional was used with Grimme's correction (PBE-D3) for structures optimization, while the HSE06 hybrid functional was used for electronic structure calculations. All calculations were performed on a $4 \times 4 \times 1$ supercell. Initially a nickel (Ni) atom was doped onto the Sn site of SnS_2 monolayer (Ni-SnS_2). Then the dual-defective SnS_2 (Ni-SnS_2-V_S) was created by single-atom Ni doping and S monovacancy (i.e. a vacancy substitutes a S atom). The band structure and DOS calculations show that Ni-SnS_2 and Ni-SnS_2-V_S have direct band gaps of 1.97 eV and 1.88 eV, respectively, smaller compared to the band gap of pristine SnS_2. Band edge alignment diagrams for both Ni-SnS_2 and Ni-SnS_2-V_S showed that they are suitable for overall water splitting, as opposed to pristine SnS_2 with a band edge alignment only favourable for oxygen evolution. The Ni-SnS_2-V_S displays effective optical absorption in the near-infrared and visible-light regions of the solar spectrum. Consequently, Ni-SnS_2 and Ni-SnS_2-V_S are prominent photocatalysts for overall water splitting.

2.4 Dissertation focus

Research on photoelectrodes based on other elements all points to SnS_2 as a champion material for its high efficiency and stability in aqueous solutions [19]. A wide range of doping research pertaining to the SnS_2 monolayer were explored. The negative and positive effects of dopants on a SnS_2 monolayer were reported for water splitting. This research seeks to tap into research space in which other dopants and doping configurations are not yet studied in detail. The few works on C dopants misses important configurations such as: doping at an interstitial site, adsorbing on a host atom and substituting a host atom, as well as some photocatalytic properties [12, 14, 37, 38]. Most of the dopants studied using DFT are metals with a high number of electrons, but few on the non-metal. According to our knowledge, the influence of Si doped SnS_2 for water splitting is missing in the literature. Therefore, this research will focus on different configurations of C and Si atom doping of SnS_2 monolayer for enhanced photocatalytic water splitting.

BIBLIOGRAPHY

[1] Sun, Y., Cheng, H., Gao, S., et al. (2012). *Freestanding Tin Disulfide Single-Layers Realizing Efficient Visible-Light Water Splitting*. Angewandte Chemie International Edition, 51(35), pp.8727-8731.

[2] Zhuang, H.L. and Hennig, R.G. (2013). *Theoretical perspective of photocatalytic properties of single-layer SnS_2*. Physical Review B, 88(11). Available at: https://doi.org/10.1103/physrevb.88.115314.

[3] Scalise, E. and Houssa, M. (2017). *Predicting 2D silicon allotropes on SnS_2*. Nano Research, 10(5), pp. 1697–1709. Available at: https://doi.org/10.1007/s12274-016-1409-y.

[4] Zhu, X. *et al.* (2018). *Band Gap Engineering of SnS_2 nanosheets by anion–anion codoping for visible-light photocatalysis*. RSC Advances, 8(6), pp. 3304–3311. Available at: https://doi.org/10.1039/c7ra12058c.

[5] Sainbileg, B. *et al.* (2019). *The dual-defective SnS_2 monolayers: Promising 2D photocatalysts for overall water splitting*. Physical Chemistry Chemical Physics, 21(48), pp. 26292–26300. Available at: https://doi.org/10.1039/c9cp04649f.

[6] Hafner, J. and Kresse, G. (1997). *The vienna ab-initio simulation program VASP: An efficient and versatile tool for studying the structural, dynamic, and electronic properties of materials*. Properties of Complex Inorganic Solids, pp. 69–82. Available at: https://doi.org/10.1007/978-1-4615-5943-6_10.

[7] Peressi, M. and Baldereschi, A. (2013). *Ab initio studies of structural and electronic properties*. Characterization of Semiconductor Heterostructures and Nanostructures, pp. 21–73. Available at: https://doi.org/10.1016/b978-0-444-59551-5.00002-9.

[8] Ma, G., Hisatomi, T. and Domen, K. (2015). *Semiconductors for photocatalytic and photoelectrochemical solar water splitting*. From Molecules to Materials, pp. 1–56.

[9] Sun, L., Zhou, W., Liu, Y., Yu, D., Liang, Y. and Wu, P. (2016). *Theoretical perspective on the electronic, magnetic and optical properties of Zn-doped monolayer SnS_2. Applied Surface Science*, 389, pp.484-490.

[10] Simfukwe, J. (2020) *First-principles study of doped hematite surfaces for photoeletrochemical water splitting*. dissertation. University of Pretoria.

[11] Zhang, Z. *et al.* (2018). *Interface Engineering of monolayer MoS_2/GaN hybrid heterostructure: Modified band alignment for photocatalytic water splitting application by Nitridation Treatment*. ACS Applied Materials & Interfaces, 10(20), pp. 17419–17426.

[12] Shown, I., Samireddi, S., Chang, Y., Putikam, R., Chang, P., Sabbah, A., Fu, F., Chen, W., Wu, C., Yu, T., Chung, P., Lin, M., Chen, L. and Chen, K. (2018). *Carbon-doped SnS2 nanostructure as a high-efficiency solar fuel catalyst under visible light*. Nature Communications, 9(1).

[13] Liyanage, P. *et al.* (2021). *L-cysteine as an irreversible inhibitor of the peroxidase-mimic catalytic activity of 2-dimensional Ni-based Nanozymes*. Nanomaterials, 11(5), p. 1285.

[14] Cheng, Z., Wang, F., Shifa, T., Liu, K., Huang, Y., Liu, Q., Jiang, C. and He, J. (2020). *Carbon Dots Decorated Vertical SnS_2 Nanosheets For Efficient Photocatalytic Oxygen Evolution*. Applied Physics Letters, 109(5). doi:10.1063/1.4960527.

[15] Hong, M., Zou, J. and Chen, Z.-G. (2021). *Synthesis of thermoelectric materials*. Thermoelectricity and Advanced Thermoelectric Materials, pp. 73–103. Available at: https://doi.org/10.1016/b978-0-12-819984-8.00010-2.

[16] Wahnón, P., Conesa, J., Palacios, P., Lucena, R., Aguilera, I., Seminovski, Y. and Fresno, F. (2011). *V-doped SnS2: a new intermediate band material for a better use of the solar spectrum*. Physical Chemistry Chemical Physics, 13(45), p.20401.

[17] Sun, L., Zhou, W., Liu, Y., Yu, D., Liang, Y. and Wu, P. (2016). *Electronic structure and optical properties of Fe-doped SnS2 from first-principle calculations*. RSC Advances, 6(5), pp.3480-3486.

[18] Yu, D., Liu, Y., Sun, L., Wu, P. and Zhou, W. (2016). *Density functional study on the hole doping of single-layer SnS_2 with metal element X (X = Li, Mg, and Al)*. Phys. Chem. Chem. Phys., 18(1), pp.318-324.

[19] Zhuang, H.L. and Hennig, R.G. (2013). *Theoretical perspective of photocatalytic properties of single-layer SnS_2*. Physical Review B, 88(11). Available at: https://doi.org/10.1103/physrevb.88.115314.

[20] Mabiala-Poaty, H., Douma, D., M'Passi-Mabiala, B. and Mapasha, R. (2018). *Structural and electronic properties of SnS 2 stacked nanosheets: An ab-initio study*. Journal of Physics and Chemistry of Solids, 120, pp.211-217.

[21] Xia, C., Zhao, X., Peng, Y., Zhang, H., Wei, S. and Jia, Y. (2015). *First-principles study of group V and VII impurities in SnS_2*. Superlattices and Microstructures, 85, pp.664-671.

[22] Mohan Kumar, G., Cho, H., Ilanchezhiyan, P., Siva, C., Ganesh, V., Yuldashev, S., Madhan Kumar, A. and Kang, T. (2019). *Evidencing enhanced charge-transfer with superior photocatalytic degradation and photoelectrochemical water splitting in Mg modified few-layered SnS_2*. Journal of Colloid and Interface Science, 540, pp.476-485.

[23] Yang, G. and Park, S.-J. (2019). *Conventional and microwave hydrothermal synthesis and application of Functional Materials: A Review*. Materials, 12(7), p. 1177. Available at: https://doi.org/10.3390/ma12071177.

[24] Parish, C.M. and Brewer, L.N. (2010). *Key parameters affecting quantitative analysis of STEM-EDS spectrum images*. Microscopy and Microanalysis, 16(3), pp. 259–272. Available at: https://doi.org/10.1017/s1431927610000267.

[25] Xiong, Z. *et al.* (2021). *Structural defects, mechanical behaviors, and properties of two-dimensional materials*. Materials, 14(5), p. 1192. Available at: https://doi.org/10.3390/ma14051192.

[26] Liu, Y., Zhou, Y., Zhou, X., Jin, X., Li, B., Liu, J. and Chen, G. (2020). *Cu doped SnS2 nanostructure induced sulfur vacancy towards boosted photocatalytic hydrogen evolution*. Chemical Engineering Journal, p.127180.

[27] M. Maghraby, A. (2019). *Introductory chapter: Electron paramagnetic resonance*. Topics From EPR Research [Preprint]. Available at: https://doi.org/10.5772/intechopen.83028.

[28] Forgács, E. and Cserháti, T. (2003). *Gas chromatography*. Food Authenticity and Traceability, pp. 197–217. Available at: https://doi.org/10.1533/9781855737181.1.197.

[29] Rastrello, F. *et al.* (2013). *Thermal conductivity detector for gas chromatography: Very wide gain range acquisition system and experimental measurements*. IEEE Transactions on Instrumentation and Measurement, 62(5), pp. 974–981. Available at: https://doi.org/10.1109/tim.2012.2236723.

[30] Chen, K. and Wu, Y.-E. (2000). *Thermal analysis and simulation of the microchannel flow in miniature thermal conductivity detectors*. Sensors and Actuators A: Physical, 79(3), pp. 211–218. Available at: https://doi.org/10.1016/s0924-4247(99)00287-3.

[31] Murdachaem, G. and Laasonen, K. (2018). *Oxygen Evolution Reaction on Nitrogen-Doped Defective Carbon Nanotubes and Graphene*. The Journal of Physical Chemistry C, 122(45), pp.25882-25892.

[32] An, Y. *et al.* (2020). *Stone–wales defects cause high proton permeability and isotope selectivity of single-layer graphene*. Advanced Materials, 32(37), p. 2002442.

[33] Kumar, J., Ansh and Shrivastava, M. (2020). *Stone–wales defect and vacancy-assisted enhanced atomic orbital interactions between graphene and ambient gases: A first-principles insight*. ACS Omega, 5(48), pp. 31281–31288.

[34] Tantardini, C. and Oganov, A.R. (2021). *Thermochemical electronegativities of the elements*. Nature Communications, 12(1). Available at: https://doi.org/10.1038/s41467-021-22429-0.

[35] Maeda, K. (2011). *Photocatalytic water splitting using semiconductor particles: History and recent developments*. Journal of Photochemistry and Photobiology C: Photochemistry Reviews, 12(4), pp. 237–268. Available at: https://doi.org/10.1016/j.jphotochemrev.2011.07.001.

[36] Sainbileg, B., Lai, Y., Chen, L. and Hayashi, M. (2019). *The dual-defective SnS2 monolayers: promising 2D photocatalysts for overall water splitting*. Physical Chemistry Chemical Physics, 21(48), pp.26292-26300.

[37] Kamali, K. (2022). *UV excited enhanced Raman scattering on carbon-doped SNS2 nanoflowers*. Materials Research Bulletin, 150, p. 111757. doi:10.1016/j.materresbull.2022.111757.

[38] Wu, R. *et al.* (2021). *Carbon-doping-induced energy-band modification and vacancies in SnS_2 nanosheets for room-temperature ppb-level NO_2 detection*. Inorganic Chemistry Frontiers, 8(23), pp. 5006–5015. doi:10.1039/d1qi00930c.

CHAPTER 3: METHODOLOGY

3.1 Brief introduction

In this chapter, a derivative of density functional theory (DFT) and its applications are discussed. DFT is still a relatively new concept in material science and quantum mechanical theory. Quantum mechanics methods together with computational simulations have become modern techniques for studying materials at the atomic level. The ability of computational physics to accurately predict the electronic structure has enabled complex studies of materials and doping techniques which provide results that can be supported both theoretically and experimentally. Density functional theory (DFT), using computational simulations, provides a detailed understanding of defects in materials and applications of such defects which can be used to improve material sciences.

3.2 Many body problem

The solution of the Schrödinger equation is a very effective approach for the description of the ideal properties of many body material systems. The time-independent non-relativistic Schrödinger equation in the general form is [1],

$$H\psi = E\psi. \tag{3.1}$$

H is the Hamiltonian operator, ψ is the wavefunction and E is the energy eigenvalue. The many body wavefunction and its dependant variables (electronic and ionic positions) along the 3D Cartesian system and other degrees of freedom is expressed as [2]:

$$\psi = \psi(\boldsymbol{r}_1, \boldsymbol{r}_2, \dots, \boldsymbol{r}_n, \boldsymbol{R}_1, \boldsymbol{R}_2, \dots, \boldsymbol{R}_m), \tag{3.2}$$

$\boldsymbol{R}$ is the position vector of the nuclei and $\boldsymbol{r}$ is the position vector of the electron. ψ is carrying information about the quantum mechanical behaviour of the system. Schrödinger equation can therefore be written as:

$$H\psi(\boldsymbol{r}_1, \boldsymbol{r}_2, \dots, \boldsymbol{r}_n, \boldsymbol{R}_1, \boldsymbol{R}_2, \dots, \boldsymbol{R}_m) = E_{tot}\psi(\boldsymbol{r}_1, \boldsymbol{r}_2, \dots, \boldsymbol{r}_n, \boldsymbol{R}_1, \boldsymbol{R}_2, \dots, \boldsymbol{R}_m), \tag{3.3}$$

E_{tot}, is the total energy of the quantum mechanical system.

The del (∇) or Laplacian in mathematics is an operator which is applied to a function to track its change along the x, y and z-directions [3]. It is expressed as:

$$\nabla^2 = \frac{\partial^2}{\partial x^2} + \frac{\partial^2}{\partial y^2} + \frac{\partial^2}{\partial z^2}. \tag{3.4}$$

The Hamiltonian is such an operator, operating on the many body wavefunction. The Hamiltonian Operator is given by [4]:

$$H = -\hbar^2 \sum_i \frac{\nabla_i^2}{2m_e} - \hbar^2 \sum_I \frac{\nabla_I^2}{2M_I} + \frac{1}{2}\sum_{i,j} \frac{e^2}{|\boldsymbol{r}_i - \boldsymbol{r}_j|} - \sum_{i,I} \frac{Z_I e^2}{|\boldsymbol{r}_i - \boldsymbol{R}_I|} + \frac{1}{2}\sum_{I,J} \frac{Z_I Z_J e^2}{|\boldsymbol{R}_I - \boldsymbol{R}_J|}, \tag{3.5}$$

$\boldsymbol{r}_i$ is the position vector of the i^{th} electron, m_e is the mass of the electron, $\boldsymbol{R}_I$ is the position vector of the I^{th} nucleus, M_I is the mass of the I^{th} nucleus and Z_I is the atomic number of the I^{th} nucleus. The first term in the Hamiltonian equation (3.5) is the kinetic energies of the electrons (T_e), the second term represents the kinetic energies of the nuclei (T_I), the third term represents the Coulomb energies for electron-electron interactions (U_{ee}), the fourth term represents Coulomb energies for electron-nuclei interactions (V_{Ie}) and the last term represents Coulomb energies for nuclei-nuclei interactions (V_{II}). To shorten the Hamiltonian we can write the corresponding terms as:

$$H = T_e + T_I + U_{ee} + V_{Ie} + V_{II}. \tag{3.6}$$

The many body Schrödinger equation becomes:

$$[T_e + T_I + U_{ee} + V_{Ie} + V_{II}]\psi = E_{tot}\psi. \tag{3.7}$$

3.3 Born-Oppenheimer Approximation

We simplify the Hamiltonian by applying the Born-Oppenheimer Approximation [5]. At a ground state, quantum systems' nuclei have minimum movement due to their size which constrains them from movement throughout the crystal compared to the electronic movement. Ions vibrate in one position while electrons can move throughout the crystal which eliminates the kinetic energy term of the nuclei and fixes the Coulomb attraction between any two nuclei;

$$T_I = -\hbar^2 \sum_I \frac{\nabla_I^2}{2M_I} \to 0, \tag{3.8}$$

$$V_{II} = \frac{1}{2}\sum_{I,J} \frac{Z_I Z_J e^2}{|\boldsymbol{R_I} - \boldsymbol{R_J}|} = c. \tag{3.9}$$

Equations (3.8) and (3.9) simplify the Hamiltonian and the many body Schrödinger equation (3.7) then becomes:

$$[T_e + U_{ee} + V_{ext}]\psi = E\psi. \tag{3.10}$$

V_{Ie} is also known as the external potential energy (V_{ext}) [2, 4] because the effect of an ion on electrons is a result of a fixed external potential. V_{II} is a constant in the electronic problem [2] and is subtracted from the total energy:

$$E = E_{tot} - V_{II} = E_{tot} - c. \tag{3.11}$$

Subsequent to simplification using the Born-Oppernheimer approximation, the Schrödinger equation (3.10) is still difficult to solve because of infinite interacting electrons causing an exponential increase in computational requirements [6].

3.4 Hartree Approximation

Hartree, in 1928, approached the complexity of this problem by reducing the many particle interacting system into a single-particle system [7]. With the Hartree approximation, the many body wavefunction with variables of position vectors becomes the product of many

single-particle wavefunctions, each consisting of a single variable of the particle's position vector. Therefore, the many body wavefunction then becomes:

$$\psi(\boldsymbol{r}_1, \boldsymbol{r}_2, \dots, \boldsymbol{r}_n) = u_1(\boldsymbol{r}_1)u_2(\boldsymbol{r}_2) \dots u_n(\boldsymbol{r}_n). \tag{3.12}$$

Hartreee approximation assumes the electrons are independent, distinguishable and non-interacting. Hence, the electrons behave as fermions, as two identical electrons cannot be in the same place at the same time. Fermions have antisymmetric wavefunctions, meaning swopping any two variables changes the sign of the wavefunction. The wavefunction can be written as:

$$\psi(\boldsymbol{r}_1, \boldsymbol{r}_2, \dots, \boldsymbol{r}_n) = c\psi(\boldsymbol{r}_1, \boldsymbol{r}_2, \dots, \boldsymbol{r}_n), \tag{3.13}$$

$$c = \begin{Bmatrix} 1 \; for \; bosons \\ -1 \; for \; fermions \end{Bmatrix}.$$

For bosons you can have an unlimited number of electrons in the same place at the same time [8]. Thus, Schrödinger equation becomes [9, 10]:

$$[T_e + U_{ee} + V_{ext}]\, u_i(\boldsymbol{r}) = \; \in_i (\boldsymbol{r})\, u_i(\boldsymbol{r}), \tag{3.14}$$

$u_i(\boldsymbol{r})$ is the single-particle wavefunction, $\in_i (\boldsymbol{r})$ is the energy eigenvalue. In the Hartree approach, the Schrödinger equation (3.14) of a many body system has become an equation of a single-particle.

The many body wavefunction and single-particle wavefunctions, $\psi \; and \; u(\boldsymbol{r})$, in QM theory, are also interpreted as probability amplitude of a particle occupying that certain space. The absolute value square of the wavefunction gives the probability amplitude [11],

$$\psi^*(\boldsymbol{r}_i)\psi(\boldsymbol{r}_i) = |\psi(\boldsymbol{r}_i)|^2. \tag{3.15}$$

Equation (3.15) represents the probability of finding one electron at $\boldsymbol{r}_1$, and another at $\boldsymbol{r}_2$, $\boldsymbol{r}_3$ and so forth. Therefore, if we have the probability of finding electrons at positions $\boldsymbol{r}_i$, then summing or integrating this function over all its variables gives the number of electrons which is simply the electron density [9, 11];

$$\int |\psi(\boldsymbol{r}_i)|^2 d\boldsymbol{r}_1 d\boldsymbol{r}_2 \dots d\boldsymbol{r}_n = n. \tag{3.16}$$

The probability amplitude of the wavefunction (3.12) is the product or probabilities of single-particle wavefunctions,

$$|\psi(\boldsymbol{r_i})|^2 = |u_1(\boldsymbol{r}_1)|^2|u_2(\boldsymbol{r}_2)|^2 \dots |u_n(\boldsymbol{r_n})|^2. \tag{3.17}$$

Integrating over all electrons except one, regardless which one, but in this case electron at position $\boldsymbol{r}_1$:

$$\int |\psi(\boldsymbol{r}_i)|^2 d\boldsymbol{r}_2 d\boldsymbol{r}_3 \dots d\boldsymbol{r}_n = n\,(\boldsymbol{r}_1). \tag{3.18}$$

Thus, according to equation (3.18), the electron density is a function of position $\boldsymbol{r}_1$. Therefore, if all unknowns are a continuous position variable ***r***, which could be along a line or area or volume covering from one position in a material to another. Integrating this function over all its variables results with N, the number of electrons along that particular region of a material is,

$$\int n(\boldsymbol{r}) d\boldsymbol{r} = N. \tag{3.19}$$

Therefore, equating equation (3.8) with equation (3.10) produces:

$$\int |\psi(\boldsymbol{r})|^2 d\boldsymbol{r} = \int n(\boldsymbol{r}) d\boldsymbol{r} = N, \tag{3.20}$$

$$\therefore \int n(\boldsymbol{r}) d\boldsymbol{r} = \int |\psi(\boldsymbol{r})|^2 d\boldsymbol{r}. \tag{3.21}$$

Removing the integrals:

$$n(\boldsymbol{r}) = \sum_j \left|\psi_j(\boldsymbol{r})\right|^2, \tag{3.22}$$

thus, summation of the probabilities of the wavefunction at a particular point, which according to equation (3.15) is the absolute value square, gives the electron density at that point. Therefore, the Hamiltonian also needs to be modified to be able to operate on the single-particle wavefunctions. There are two methods to do this, however the focus will only be on one of these methods [12]:

Variational Principle Method

This method uses the Variational Principle [9, 12] which predicts wavefunction and electronic properties at the ground state point. If electronic properties at ground state can be accurately predicted, then electronic properties at different energy levels can then be computed. Therefore, to find the ground state energy at absolute minimum where the system is at absolute stability:

$$E_0 = \frac{\langle\psi|H|\psi\rangle}{\langle\psi|\psi\rangle}, \tag{3.23}$$

$$\langle\psi_i|\psi_j\rangle = \int d^3r\ \psi_i^*(\boldsymbol{r})\,\psi_j(\boldsymbol{r}) = \delta_{ij} = \begin{cases} 1\,,\ i = j \\ 0\,,\ i \neq j \end{cases}. \tag{3.24}$$

A denominator cannot be 0, hence the only mathematically correct solution is 1,

$$\therefore \langle\psi|\psi\rangle = \int\ u_1^*(\boldsymbol{r}_1)u_2^*(\boldsymbol{r}_2)\ldots u_n^*(\boldsymbol{r}_n)\,u_1(\boldsymbol{r}_1)u_2(\boldsymbol{r}_2)\ldots u_n(\boldsymbol{r}_n)d\boldsymbol{\tau} = 1, \tag{3.25}$$

thus, it is normalized [9, 13]. Therefore, ground state energy becomes:

$$E_0 = \langle\psi|H|\psi\rangle$$

$$= \int d^3\boldsymbol{r}_1 d^3\boldsymbol{r}_2 \ldots d^3\boldsymbol{r}_n\, u_1^*(\boldsymbol{r}_1)u_2^*(\boldsymbol{r}_2)\ldots u_n^*(\boldsymbol{r}_n)\,[T_e + U_{ee} + V_{ext}]$$

$$u_1(\boldsymbol{r}_1)u_2(\boldsymbol{r}_2)\ldots u_n(\boldsymbol{r}_n). \tag{3.26}$$

Equation (3.26) is referred to as the expectation value of the ground state energy. Therefore, from equation (3.14), the energy for the entire system is the summation of the individual Hamiltonians and energy-eigenvalues of the particles;

$$\therefore \sum_i Hu_i(\boldsymbol{r}_i) = \sum_i \in (\boldsymbol{r})u_i(\boldsymbol{r}_i), \tag{3.27}$$

We multiply (3.27) by $\int u_i^*(r_i)d\boldsymbol{\tau}$, where $d\boldsymbol{\tau} = d^3\boldsymbol{r}_1 d^3\boldsymbol{r}_2 \ldots d^3\boldsymbol{r}_n$:

$$\sum_i \int u_i^*(\boldsymbol{r}_i)Hu_i(\boldsymbol{r}_i) = \sum_i \in (\boldsymbol{r}) \int u_i^*(\boldsymbol{r}_i)u_i(\boldsymbol{r}_i)d\boldsymbol{\tau}$$

$$\Rightarrow \qquad \sum_i\langle\psi|H|\psi\rangle = \sum_i \in (\boldsymbol{r}) \int u_i^*(\boldsymbol{r}_i)u_i(\boldsymbol{r}_i)d\boldsymbol{\tau}, \tag{3.28}$$

To find ground state energy, it is necessary to find the absolute minimum for $\langle\psi|H|\psi\rangle$. A convenient way to achieve this is through the use of the Variational Principle [6, 14]:

$$\delta[\sum_i\langle\psi|H|\psi\rangle - \sum_i \in (\boldsymbol{r}) \int u_i^*(\boldsymbol{r}_i)u_i(\boldsymbol{r}_i)d\boldsymbol{\tau}] = 0. \tag{3.29}$$

From here onwards, the atomic unit system is adopted as $\hbar = m_e = e = 4\pi/\varepsilon_0 = 1$. This leads to the single-particle Hartree equation:

$$\left[-\frac{1}{2}\nabla^2 - \sum_I \frac{Z_I}{|\boldsymbol{R}_I - \boldsymbol{r}|} + \sum_{i\neq j}\int \frac{|u(\boldsymbol{r}')|^2}{|\boldsymbol{r}-\boldsymbol{r}'|}d\boldsymbol{r}'\right] u_i(\boldsymbol{r}) = \in_i (\boldsymbol{r})u_i(\boldsymbol{r}). \tag{3.30}$$

To the right of the equation is the new energy eigenvalue. Using equation (3.22) and also generalising for a 3 dimensional system, the single-particle Hartree equation is obtained:

$$\left[-\frac{1}{2}\nabla^2 - \sum_I \frac{Z_I}{|\boldsymbol{R}_I - \boldsymbol{r}|} + \int \frac{n_j(\boldsymbol{r}')}{|\boldsymbol{r}-\boldsymbol{r}'|}d\boldsymbol{r}'\right] u_i(\boldsymbol{r}) = \in_i (\boldsymbol{r})u_i(\boldsymbol{r}). \tag{3.31}$$

The term $\int \frac{n_j(\boldsymbol{r}')}{|\boldsymbol{r}-\boldsymbol{r}'|}d\boldsymbol{r}'$ is known as the Hartree potential [8, 15, 16]. Equation (3.14) can now be written as:

$$[T_e + V_{ext} + V_H]u_i(\boldsymbol{r}) = \in_i (\boldsymbol{r})u_i(\boldsymbol{r}), \tag{3.32}$$

$$[T_e + V_{eff}]u_i(\boldsymbol{r}) = \in_i (\boldsymbol{r})u_i(\boldsymbol{r}). \tag{3.33}$$

The second term of equation (3.33) is known as the effective potential and is the sum of the external potential and the Hartree potential:

$$V_{eff} = V_{ext} + V_H. \tag{3.34}$$

The effective potential V_{eff} in equation (3.34) describes the movement of electrons in the solid, as it contains the V_{ext} term, which is the Coulomb interaction of the electrons and nuclei, and the V_H term, which is the Hartree electron-electron interactions. If the atoms are moved around, their energy will change and the electrons will automatically adjust. Thus, real electrons are replaced by effective electrons which have similar charge, mass, density distribution and are independent non-interacting electrons moving inside an effective potential or what in other literatures is referred to as an electron cloud.

Equation (3.33) contains the kinetic energy of an electron and the effective potential. Meaning that the movement of a single electron is tracked as a result of movement of other effective electrons. Therefore, this means that an electron at position $\boldsymbol{r}_i$ sees all other electrons as an electron cloud and this would mean that electrons are distinguishable. This leads to the failures of the Hartree model.

Equation (3.33) is incapable of representing real quantum mechanical systems [6, 15, 16] because in any real system:

- Electrons are indistinguishable, therefore it is almost impossible to keep track of the movement of any single electron.
- There is correlation interaction amongst electrons in a quantum system. The Hartree approach neglects all of these effects.

3.5 Hartree-Fock Approximation

Fock, in 1930, further developed the Hartree approximation and later called it the Hartree-Fock approximation. In the Hartree-Fock approximation, anti-symmetry is applied to the trial wavefunction through the expression of Slater determinants [17]. Anti-symmetry is also achieved through obeying the Pauli Exclusion Principle which states that no two electrons can occupy the same state [8, 18]. Electrons in the same state have the same energy, occupy the same position and have the same spin [18]. Therefore, the Hartree-Fock approximation considers the spin parameter in its wavefunction. Hartree-Fock approximation is the first theory to allow qualitative predictions of molecular systems in a way that was computationally manageable.

Slater Determinants

Given N electron wavefunctions, only one antisymmetric combination can be formed. Therefore, the wavefunction $\psi(\boldsymbol{r}_i, \sigma_i)$ is written in terms of position $(\boldsymbol{r}_i)$ and spin (σ_i) of

the i[th] electron. The different electron wavefunctions containing electron position and spin can be represented by the following matrix [19, 20]:

$$\psi(\boldsymbol{r}_i,\sigma_i)=\frac{1}{\sqrt{N!}}\begin{bmatrix} u_1(\boldsymbol{r}_1,\sigma_1)\ u_2(\boldsymbol{r}_1,\sigma_2)\ \dots\ u_N(\boldsymbol{r}_N,\sigma_N) \\ u_1(\boldsymbol{r}_2,\sigma_1)\ u_2(\boldsymbol{r}_2,\sigma_2)\ \dots\ u_N(\boldsymbol{r}_2,\sigma_N) \\ \vdots \\ u_1(\boldsymbol{r}_N,\sigma_1)\ u_2(\boldsymbol{r}_N,\sigma_2)\ \dots u_N(\boldsymbol{r}_N,\sigma_N) \end{bmatrix}. \tag{3.35}$$

The electrons considered in the Hartree-Fock approximation are fermions. Fermions have antisymmetric wavefunctions as opposed to bosons which can have an unlimited number of particles in the same place at the same time.

In equation (3.35), $\frac{1}{\sqrt{N!}}$ is the normalizing factor chosen such that $\int|\psi|^2 d\boldsymbol{\tau}=1$ [21]. Therefore, Slater determinant is given by:

$$\psi(\boldsymbol{r}_i,\sigma_i)=\frac{1}{\sqrt{N!}}\sum_P(-)^P P u_1(\boldsymbol{r}_1,\sigma_1)u_2(\boldsymbol{r}_2,\sigma_2)\dots u_n(\boldsymbol{r}_N,\sigma_N), \tag{3.36}$$

where P is the permutations operator. Antisymmetry can be achieved in the Slater determinant. If any two columns or rows are equal, the determinant is zero. Therefore, no two electrons can have the same position and spin [20]. The variable $\boldsymbol{r}_i$ is chosen to represent both position and spin of the i[th] electron. Therefore, the ground state wavefunction is given by:

$$\psi(\boldsymbol{r}_i)=\frac{1}{\sqrt{N!}}\sum_P(-)^P P u_1(\boldsymbol{r}_1)u_2(\boldsymbol{r}_2)\dots u_n(\boldsymbol{r}_n). \tag{3.37}$$

The Hartree-Fock wavefunction (3.37) is then substituted into the Schrödinger equation and the same procedure as was executed with the Hartree method is applied. This results in the following expectation value for the energy:

$$E=\langle\psi|H|\psi\rangle=\langle H\rangle$$

$$\therefore H=-\sum_i^N\frac{1}{2}\nabla_i^2-\sum_{I,i}^N\frac{Z_I}{|\boldsymbol{r}_i-\boldsymbol{R}_I|}+\frac{1}{2}\sum_{i,j}^N\frac{n_i(\boldsymbol{r}_i)n_j(\boldsymbol{r}_j)}{|\boldsymbol{r}_i-\boldsymbol{r}_j|}d^3\boldsymbol{r}_i d^3\boldsymbol{r}_j$$

$$-\frac{1}{2}\sum_{i,j}^N\int\frac{u_i^*(\boldsymbol{r}_i)u_j^*(\boldsymbol{r}_j)u_i(\boldsymbol{r}_j)u_j(\boldsymbol{r}_i)}{|\boldsymbol{r}_i-\boldsymbol{r}_j|}d^3\boldsymbol{r}_i d^3\boldsymbol{r}_j. \tag{3.38}$$

Insert this Hamiltonian back into the Schrödinger Equation (3.31):

$$\epsilon_i\,(\boldsymbol{r})u_i(\boldsymbol{r}) = \left[\begin{array}{c} -\sum_i^N \frac{1}{2}\nabla_i^2 - \sum_{I,i}^N \frac{Z_I}{|\boldsymbol{r}_i - \boldsymbol{R}_I|} + \frac{1}{2}\sum_{i,j}^N \frac{n_i(\boldsymbol{r}_i)n_j(\boldsymbol{r}_j)}{|\boldsymbol{r}_i - \boldsymbol{r}_j|} d^3\boldsymbol{r}_i d^3\boldsymbol{r}_j \\ -\frac{1}{2}\sum_{i,j}^N \int \frac{u_i^*(\boldsymbol{r}_i)u_j^*(\boldsymbol{r}_j)u_i(\boldsymbol{r}_j)u_j(\boldsymbol{r}_i)}{|\boldsymbol{r}_i - \boldsymbol{r}_j|} d^3\boldsymbol{r}_i d^3\boldsymbol{r}_j \end{array}\right] u_i(\boldsymbol{r}). \quad (3.39)$$

The above equation is known as the Hartree-Fock equation [22]. The third term on the right-hand side of the equation is the electron-electron interaction term and the fourth term is known as the exchange interaction. The exchange term originates purely from the antisymmetric nature of the wavefunction [22].

To further explain the last term, the nature of electrons is that they move in such a way that minimizes their energy thus increase their stability. Electrons with the same spin repel while oppositely spinning electrons attract and are able to share the same orbital state. Electrons are aware of their presence and go out of their ways to avoid being close to one another which may cause them to end up exchanging/swopping positions [23], thus the electron exchange interaction term. This is the term which links the non-interacting system to the interacting system, however Hartree-Fock equations are still not well-equipped to describe a QM system.

Although Hartree-Fock was the first theory which allowed qualitative predictions for molecular systems it had its own limitations and inaccurate predictions for a real solid state model [20, 24].

- A true self-consistent Hartree-Fock Approximation is very complex and relies on multi-variable wavefunction of 3N or more dimensions which in computational studies is referred to as the curse of dimensionality. Solving these multi-variable functions would take ages even with the use of high processing computers.

- Correlation energy, which is a measure of how much the movement of one electron is influenced by the presence of all other electrons, has been neglected.

- Electrons being distinguishable is represented mathematically by a changing sign of the function when the single-electron orbitals or wavefunctions change positions. Therefore Hartree-Fock treats electrons like fermions instead of boson and in any real system electrons are indistinguishable.

- Hartree-Fock equations are used to study small chemical systems like molecules successfully on the computer, but do not work well for bulk crystalline materials.

Therefore, a complete Schrödinger equation with all information of an interacting system will have an exchange term and a correlation term. We, therefore, turn to DFT to combat short comings of the Hartree-Fock approximation.

3.6 Density Functional Theory (DFT)

Density functional theory (DFT) provides another starting point for treating the many body systems and provides a better way of approximating electron correlations for ground state properties [15, 24]. DFT mainly states that the electron density and electron energy contains all the needed information pertaining to the chemistry of the quantum mechanical system. DFT is a highly computationally efficient method and has met with considerable success for calculating the binding energies, lattice parameters and bulk moduli of metals [9]. The impact of DFT in the science community was recognised by the awarding of Nobel Prize in Chemistry in 1998 to Walter Kohn [25].

Just like the Hartree approach, DFT reduces the many body ground state problem into a one-particle Schrödinger equation. DFT is based on two basic concepts. The first is the Hohenberg-Kohn theorem (HK) and the second is the Kohn-Sham equations (KS) [26].

3.6.1 Hohenberg-Kohn Theorem

Hohenberg-Kohn Theorem is composed of two parts [27]. The first part states that electron density uniquely determines the system's external potential energy. As always, the starting point is the Schrödinger based quantum mechanics. Therefore, the Hamiltonian for the many body system in the Born-Oppenheimer approximation is:

$$H_{BO}(\boldsymbol{r}_i, \boldsymbol{R}_i) = -\sum_i^N \frac{1}{2}\nabla_i^2 + \sum_{i<j}^N \frac{1}{|\boldsymbol{r}_i - \boldsymbol{r}_j|} - \sum_i^N V_{ext}(\boldsymbol{r}_i, \boldsymbol{R}_I). \tag{3.40}$$

Here the focus will be on the external potential:

$$V_{ext}(\boldsymbol{r}, \boldsymbol{R}_I) = -\sum_I^N \frac{Z_I}{|\boldsymbol{r}-\boldsymbol{R}_I|}. \quad (3.41)$$

In the quantum mechanical approach:

$$V_{ext}(\boldsymbol{r}, \boldsymbol{R}_i) \quad \rightarrow \quad \psi(\boldsymbol{r}_i, \boldsymbol{R}_i) \; and \; E(\boldsymbol{R}_i) \quad \rightarrow \quad Properties$$

The external potential $V_{ext}(\boldsymbol{r}, \boldsymbol{R}_i)$ is used to build the Hamiltonian, the Hamiltonian is used to solve the Shrödinger equation from which the wavefunction $\psi(\boldsymbol{r}_i, \boldsymbol{R}_i)$ and the energy are obtained, thus the properties of the system are also obtained. According to the Hohenberg-Kohn theorem, the ground state electron density ($n_0(\boldsymbol{r})$) uniquely determines the ground state wavefunction and energy [27].

$$n_0(\boldsymbol{r}) \quad \rightarrow \quad \psi(\boldsymbol{r}_i, \boldsymbol{R}_i) \; and \; E(\boldsymbol{R}_i) \quad \rightarrow \quad Properties$$

This suggests that there is a one-to-one unique correspondence between 3N V_{ext} and 3D n_0. Therefore, instead of finding the 3N or more dimensional wavefunction, we start by finding the 3D electron density. Thus, curse of dimensionality is avoided and equations can now be reasonably solved with computation.

Hamiltonian:

$$H = \sum_{i=1}^N T_e + \sum_{i<j}^N V_{ee} + \sum_{i=1}^N V_{ext}(\boldsymbol{r}_i, \boldsymbol{R}_I). \quad (3.42)$$

Expectation value for the energy:

$$\langle H \rangle = \langle \psi | T | \psi \rangle + \langle \psi | U | \psi \rangle + \sum_{i=1}^n \langle \psi | V_{ext}(\boldsymbol{r}_i) | \psi \rangle, \quad (3.43)$$

$$\therefore \langle \psi | V_{ext}(\boldsymbol{r}_k) | \psi \rangle = \int d\boldsymbol{r}_1 d\boldsymbol{r}_2 \ldots d\boldsymbol{r}_N \psi^*(\boldsymbol{r}_i) V_{ext}(\boldsymbol{r}_k) \psi(\boldsymbol{r}_i), \quad (3.44)$$

ψ is the 3N dimensional wavefunction and $V_{ext}(\boldsymbol{r}_k)$ is the external potential for electron (k). Therefore, electron k has position vector $\boldsymbol{r}_k$ and integration variable $d\boldsymbol{r}_k$. Since the electrons are continuously distributed, $d\boldsymbol{r}_k$ is separated from all other variables while the remaining variables are just grouped together as $d\boldsymbol{x}'$ and equation (3.44) becomes:

$$\langle \psi | V_{ext}(\boldsymbol{r}_k) | \psi \rangle = \int V_{ext}(\boldsymbol{r}_k) d\boldsymbol{r}_k \int d\boldsymbol{x}' |\psi(\boldsymbol{r}_i)|^2. \quad (3.45)$$

According to equation (3.18) this will reduce to:

$$\langle\psi|V_{ext}(\boldsymbol{r}_k)|\psi\rangle = \int V_{ext}(\boldsymbol{r}_k)n(\boldsymbol{r}_k)d\boldsymbol{r}_k. \quad (3.46)$$

Generally,

$$\langle\psi|V_{ext}(\boldsymbol{r})|\psi\rangle = \int V_{ext}(\boldsymbol{r})\, n(\boldsymbol{r})\, d\boldsymbol{r}. \quad (3.47)$$

This yields an expectation value of the external potential which is a functional consisting of a manageable 3 dimensional electron density.

Proof:

We seek to prove the first Hohenberg Kohn Theorem and this will be done by contradiction. That is, initially, the opposite is assumed correct for which this is expected to arrive at an absurd solution. The contradiction is to show that the ground state density does not uniquely determine the external potential. Therefore, suppose that two different potentials, differing by more than a constant, have the same ground state density:

Potential 1 with wavefunction 1 (WF1): $V_{ext}^{(1)} \rightarrow \psi_0^{(1)} \rightarrow n_0^{(1)}(\boldsymbol{r})$

Potential 2 with wavefunction 2 (WF2): $V_{ext}^{(2)} \rightarrow \psi_0^{(2)} \rightarrow n_0^{(2)}(\boldsymbol{r})$

Where: $n_0^{(2)}(\boldsymbol{r}) = n_0^{(1)}(\boldsymbol{r})$

Expectation value of WF1 in Hamiltonian 1 is the absolute minimum and therefore gives ground state energy lower than that produced by expectation value of WF2 in Hamiltonian 1:

$$\left\langle\psi_0^{(1)}\middle|H^{(1)}\middle|\psi_0^{(1)}\right\rangle < \left\langle\psi_0^{(2)}\middle|H^{(1)}\middle|\psi_0^{(2)}\right\rangle, \quad (3.48)$$

$$\left\langle\psi_0^{(1)}\middle|H^{(1)}\middle|\psi_0^{(1)}\right\rangle = \left\langle\psi_0^{(1)}\middle|T\middle|\psi_0^{(1)}\right\rangle + \left\langle\psi_0^{(1)}\middle|U\middle|\psi_0^{(1)}\right\rangle + \int V_{ext}^{(1)}(\boldsymbol{r})n_0^{(1)}(\boldsymbol{r})d\boldsymbol{r}, \quad (3.49)$$

$$\left\langle\psi_0^{(2)}\middle|H^{(1)}\middle|\psi_0^{(2)}\right\rangle = \left\langle\psi_0^{(2)}\middle|T\middle|\psi_0^{(2)}\right\rangle + \left\langle\psi_0^{(2)}\middle|U\middle|\psi_0^{(2)}\right\rangle + \int V_{ext}^{(1)}(\boldsymbol{r})n_0^{(2)}(\boldsymbol{r})d\boldsymbol{r}, \quad (3.50)$$

$$\left\langle\psi_0^{(1)}\middle|T\middle|\psi_0^{(1)}\right\rangle + \left\langle\psi_0^{(1)}\middle|U\middle|\psi_0^{(1)}\right\rangle < \left\langle\psi_0^{(2)}\middle|T\middle|\psi_0^{(2)}\right\rangle + \left\langle\psi_0^{(2)}\middle|U\middle|\psi_0^{(2)}\right\rangle. \quad (3.51)$$

The last terms of equations (3.49) and (3.50) are removed from the inequality equation (3.51) since they are the same (i.e. the density of the system is a constant) and thus one cannot be greater or smaller than the other.

Likewise if the expectation value of WF2 in Hamiltonian 2 gives absolute minimum and therefore its ground state energy is lower than the expectation value of WF1 in Hamiltonian 2. We follow the same procedure as above:

$$\left\langle \psi_0^{(2)} \middle| H^{(1)} \middle| \psi_0^{(2)} \right\rangle > \left\langle \psi_0^{(2)} \middle| H^{(2)} \middle| \psi_0^{(2)} \right\rangle, \tag{3.52}$$

$$\left\langle \psi_0^{(1)} \middle| T \middle| \psi_0^{(1)} \right\rangle + \left\langle \psi_0^{(1)} \middle| U \middle| \psi_0^{(1)} \right\rangle > \left\langle \psi_0^{(2)} \middle| T \middle| \psi_0^{(2)} \right\rangle + \left\langle \psi_0^{(2)} \middle| U \middle| \psi_0^{(2)} \right\rangle, \tag{3.53}$$

(3.51) and (3.53) cannot be true at the same time. Therefore **Absurd!** Two different potentials cannot have identical densities. Thus, Hohenberg-Kohn first theorem is true, the ground state density uniquely determines the external potential and consequently the wavefunction, energies, etc.

The second part of the Hohenberg-Kohn theorem is known as the variational property [28]. It states that the electron density that absolutely minimizes the energy functional is the ground state electron density.

In the first theorem we proved that electron density uniquely defines the energy functional. If the energy is a functional of electron density, then components of the energy (i.e. the kinetic energy, Coulomb interactions and external potential) are also functionals of the electron density. If the universal functional F[n(**r**)] is defined by:

$$F[n(\boldsymbol{r})] = \langle \psi(\boldsymbol{r}) | T + U | \psi(\boldsymbol{r}) \rangle, \tag{3.54}$$

T is the kinetic energy of the electrons and U is the electron-electron interaction potential. F is said to be universal because treatment of kinetic energy and Coulomb forces is common for all systems [29, 30]. Therefore, mathematically the second H-K theorem can be written as:

$$E[n(\boldsymbol{r})] = F[n(\boldsymbol{r})] + \int V_{ext}(\boldsymbol{r}) n(\boldsymbol{r}) d\boldsymbol{r} \geq E[n_0], \tag{3.55}$$

$$\therefore E[n_0] \leq E[n]. \tag{3.56}$$

Proof:

Consider an arbitrary wavefunction $\psi'(\boldsymbol{r})$ uniquely defined by electron density $n'(\boldsymbol{r})$,

$$\therefore N = \int n_0(\boldsymbol{r})d\boldsymbol{r} = \int n'(\boldsymbol{r})d\boldsymbol{r}. \tag{3.57}$$

This means that the total number of electrons in the system is the same regardless of integrating the ground state electron density $n_0(\boldsymbol{r})$ or any other arbitrary electron density $n'(\boldsymbol{r})$. Assume ψ' Minimizes $F[n'(\boldsymbol{r})]$ such that:

$$F[n'(\boldsymbol{r})] = \langle\psi'_{min}|T + U|\psi'_{min}\rangle. \tag{3.58}$$

Therefore, the arbitrary external potential $V'_{ext}(\boldsymbol{r})$ and energy functional $E[n'(\boldsymbol{r})]$ are expressed as:

$$E[n'(\boldsymbol{r})] = \langle\psi'_{min}|H|\psi'_{min}\rangle$$

$$E[n'(\boldsymbol{r})] = F[n'(\boldsymbol{r})] + \int V'_{ext}(\boldsymbol{r})n'(\boldsymbol{r})d\boldsymbol{r}. \tag{3.59}$$

From the first part of the H-K theorem it was proved that the electron density uniquely defines energy. Therefore, if we consider the ground state electron density $n_0(\boldsymbol{r})$ that corresponds to the wavefunction $\psi_0(\boldsymbol{r})$, it uniquely defines the ground state energy:

$$E[n_0(\boldsymbol{r})] = \langle\psi_0(\boldsymbol{r})|H|\psi_0(\boldsymbol{r})\rangle. \tag{3.60}$$

Applying equation (3.60) into (3.59) then:

$$E[n_0(\boldsymbol{r})] = F[n_0(\boldsymbol{r})] + \int V_{ext}(\boldsymbol{r})n_0(\boldsymbol{r})d\boldsymbol{r}. \tag{3.61}$$

According to equation (3.48) and (3.52) above:

$$\langle\psi'_{min}|H|\psi'_{min}\rangle > \langle\psi_0(\boldsymbol{r})|H|\psi_0(\boldsymbol{r})\rangle,$$

$$\therefore F[n'(\boldsymbol{r})] + \int V'_{ext}(\boldsymbol{r})n'(\boldsymbol{r})d\boldsymbol{r} > F[n_0(\boldsymbol{r})] + \int V_{ext}(\boldsymbol{r})n_0(\boldsymbol{r})d\boldsymbol{r},$$

$$\therefore E[n'(\boldsymbol{r})] \geq E[n_0(\boldsymbol{r})],$$

thus, equation (3.56) is correct. Therefore, this proves that the energy corresponding to any trial electron density should always be higher than or equal to the ground state energy

corresponding to the ground state electron density. This was the birth of DFT. The energy is a function of the electron density which is a function of the position vector $\boldsymbol{r}$. The energy is a function of a function and this, in mathematical terms, is called a functional.

However, at this point DFT is still not an applicable tool for material analysis. We know energy is a functional of electron density, but our challenge now is finding what this energy functional is exactly. Kohn-Sham equations were used to solve this problem.

3.6.2 Kohn-Sham Equations

Kohn and Sham were able to produce equations which are able to effect DFT from a theoretical phenomenon to a day-to-day applicable tool. Kohn-Sham equations are self-consistent equations which map the interacting many body electronic system onto a system of non-interacting electrons moving in an effective potential [31]. Therefore, Kohn-Sham approach is to find a good approximation of the energy functional [26, 31],

$$E[n(\boldsymbol{r})] = \langle\psi(\boldsymbol{r})|H|\psi(\boldsymbol{r})\rangle = \langle\psi(\boldsymbol{r})|T + U_{ee} + V_{ext}|\psi(\boldsymbol{r})\rangle, \tag{3.62}$$

$$= F[n(\boldsymbol{r})] + E_{ext}[n] = \int \psi^*(\boldsymbol{r})[T + U_{ee}]\psi(\boldsymbol{r})d\boldsymbol{r} + \int V_{ext}(\boldsymbol{r})n(\boldsymbol{r})d\boldsymbol{r}, \tag{3.63}$$

$$E[n] = F[n] + V_{ext}[n] = \mathrm{F[n]} + \int V_{ext}(\boldsymbol{r})n(\boldsymbol{r})d\boldsymbol{r}. \tag{3.64}$$

Energy is a functional of electron density. Since it has been figured out how to express external potential as a functional of the electron density, the challenge is to express kinetic energy and electron-electron interaction as functionals of electron density. Kohn-Sham equations follow single-electron Hartree orbitals.

Expectation value of the kinetic energy for single-particles is:

$$T[n] = -\frac{1}{2}\sum_i^N \langle u_i^*(\boldsymbol{r})|\nabla_i^2|u_i(\boldsymbol{r})\rangle. \tag{3.65}$$

Electron-electron interaction which is the Hartree Potential:

$$U_{ee}[n] = \sum_{i<j}^N \int \frac{|u_i(\boldsymbol{r}_i)|^2|u_j(\boldsymbol{r}_j)|^2}{|\boldsymbol{r}_i - \boldsymbol{r}_j|} d\boldsymbol{r}_i d\boldsymbol{r}_j. \tag{3.66}$$

Remembering: $n_i(\boldsymbol{r}_i) = \sum_i^N |u_i(\boldsymbol{r}_i)|^2$

$$\therefore U_{ee}[n] = \sum_{i<j}^N \int \frac{|u_i(\boldsymbol{r}_i)|^2 |u_j(\boldsymbol{r}_j)|^2}{|\boldsymbol{r}_i - \boldsymbol{r}_j|} d\boldsymbol{r}_i d\boldsymbol{r}_j = \int \frac{n_i(\boldsymbol{r}_i) n_j(\boldsymbol{r}_j)}{|\boldsymbol{r}_i - \boldsymbol{r}_j|} d\boldsymbol{r}_i d\boldsymbol{r}_j. \quad (3.67)$$

The kinetic energy and electron-electron interaction with the Kohn Sham approach becomes:

$$T[n] = -\frac{1}{2}\sum_i^N \int u_i^*(\boldsymbol{r}) \nabla_i^2 u_i(\boldsymbol{r}) d\boldsymbol{r} + T_c[n(r)] = T_{sp}[n(\boldsymbol{r})] + T_C[n(\boldsymbol{r})], \quad (3.68)$$

$$U[n] = \sum_{i<j}^n \int \frac{|u_i(\boldsymbol{r}_i)|^2 |u_j(\boldsymbol{r}_j)|^2}{|\boldsymbol{r}_i - \boldsymbol{r}_j|} d\boldsymbol{r}_i d\boldsymbol{r}_j + U_X[n(\boldsymbol{r})] = U_H[n(\boldsymbol{r})] + U_X[n(\boldsymbol{r})]. \quad (3.69)$$

The first term in equation (3.68) is the kinetic energy of a single electron (hence sp for single-particle) and the second term is the correlation energy which is unknown from a fully interacting system. The first term in equation (3.69) is the Hartree potential and the second term is the exchange interaction of electrons which is also unknown from a fully interacting system.

Therefore, there is an exact non-interacting part, and a separate exchange and correlation part to include information of the fully interacting system. The exchange and correlation cannot be exact and is therefore approximated. The success and effectiveness of DFT is due to this exact and approximation. Thus, the total energy functional will now have extra terms which are the correlation energy functional and the exchange interaction energy functional [32]:

$$E[n] = T_{sp}[n] + E_H[n] + E_{ext}[n] + T_C[n(\boldsymbol{r})] + U_X[n(\boldsymbol{r})]. \quad (3.70)$$

The two terms are contained in one term called the exchange and correlation functional $E_{XC}[n]$:

$$E[n] = T_{sp}[n] + E_H[n] + E_{ext}[n] + E_{XC}[n]. \quad (3.71)$$

Kohn Sham equations can thus be written as:

$$\left[-\frac{1}{2}\nabla^2 + V_{ext}(\boldsymbol{r}) + V_H(\boldsymbol{r}) + V_{XC}(\boldsymbol{r})\right]\psi_i(\boldsymbol{r}) = \varepsilon_i \psi_i(\boldsymbol{r}). \quad (3.72)$$

The potential terms are also known as effective potentials, $V_{eff}(\boldsymbol{r}) = V_{ext}(\boldsymbol{r}) + V_H(\boldsymbol{r}) + V_{XC}(\boldsymbol{r})$, such that (3.72) becomes:

$$\left[-\frac{1}{2}\nabla^2 + V_{eff}(\boldsymbol{r})\right]\psi_i(\boldsymbol{r}) = \varepsilon_i\psi_i(\boldsymbol{r}), \tag{3.73}$$

where:

$$V_{XC}(\boldsymbol{r}) = \frac{\delta E_{XC}[n(\boldsymbol{r})]}{\delta n(\boldsymbol{r})} \quad , V_H(\boldsymbol{r}) = \frac{\delta E_H[n(\boldsymbol{r})]}{\delta n(\boldsymbol{r})} = \int \frac{n(\boldsymbol{r}_2)}{|\boldsymbol{r}_1 - \boldsymbol{r}_2|} d\boldsymbol{r}_2, \quad V_{Ext}(\boldsymbol{r}) = \frac{\delta E_{Ext}[n(\boldsymbol{r})]}{\delta n(\boldsymbol{r})}.$$

Kohn and Sham made assumptions that transformed the problem from a system of N interacting electrons to an equivalent system with N non-interacting electrons with the same ground state electron density as the interacting system. These Kohn-Sham equations are self-consistently solved in the following manner [2, 33, 34]:

(1) Start with initial guess of n($\boldsymbol{r}$)
(2) Calculate V_{eff}
(3) Solve K-S equation for the K-Sham Wavefunction
(4) Use Wavefunction to find energy eigen-functions and thus total energy
(5) Total energy is a functional of density. Therefore use energy to find the density
(6) Match the new density with the initially guessed density
(7) If they are not equal then take a new guess of the density and repeat the process until new density is equal to initial density or converges to a certain interval of the initial density
(8) Once convergence is reached then total energy is computed.

3.7 Exchange Correlation Energy Functional

Exchange and correlation term possesses all information of the fully interacting system and is approximated. The most popular of the exchange and correlation approximations are local density approximation (LDA) and generalized gradient approximation (GGA) [35].

3.7.1 Local Density Approximation (LDA)/ Local Spin Density Approximation (LSDA)

Here, the model of a non-interacting homogenous electron gas or uniform electron gas (UEG) is used. This model uniformly distributes the electrons in the molecules. As a result of this uniformity, it can be assumed that the integral of the local density at $\boldsymbol{r}$ represent the exchange and correlation interactions over all space of the crystal.

Dirac in the 1930's developed local density approximation (LDA) for exchange functional of a homogeneous electron gas [36]. These produced results as accurate as possible and accelerated the use of DFT for electronic structure calculations.

For spin-polarized systems, the spin is included in the LDA and thus called local spin density approximation (LSDA) [26, 31]. The generalized expressions for LDA and LSDA approximations are:

LDA

$$E_{XC}^{LDA}[n(\boldsymbol{r})] = \int d\boldsymbol{r}\, n(\boldsymbol{r})\varepsilon_{XC}[n(\boldsymbol{r})]. \tag{3.74}$$

LSDA

$$E_{XC}^{LSDA}\left[n^{\uparrow}(\boldsymbol{r}), n^{\downarrow}(\boldsymbol{r})\right] = \int d\boldsymbol{r}\, n(\boldsymbol{r})\varepsilon_{XC}[n^{\uparrow}(\boldsymbol{r}), n^{\downarrow}(\boldsymbol{r})]. \tag{3.75}$$

The factor ε_{XC} is the exchange and correlation energy per density and, according to Dirac, their exact mathematical expressions are [2, 26]:

$$E_{XC}^{hom}[n(\boldsymbol{r})] = -\frac{3}{4}\left(\frac{3n(\boldsymbol{r})}{\pi}\right)^{1/3}, \tag{3.76}$$

$$E_{X}^{LDA}[n(\boldsymbol{r})] = -\frac{3}{4}\left(\frac{3}{\pi}\right)^{\frac{1}{3}}\int d\boldsymbol{r}\, n(\boldsymbol{r})^{\frac{4}{3}}. \tag{3.77}$$

Equation (3.76) can be evaluated exactly for a known local electron density, and equation (3.77) can be determined for a continuously distributed electron density. However, molecules do not conform to UEG model and in a crystal electrons are not uniformly distributed especially in the presence of defects where there are large variations in the density.

3.7.2 Generalized Gradient Approximation (GGA)

This approximation states that for the majority of real QM systems, there is a gradient in the density along $\boldsymbol{r}$. Therefore, GGA tends to improve LDA functionals by including the gradient of the density. The general expression for GGA functionals is given below as [37, 38]:

$$E_{XC}[n(\boldsymbol{r})] = \int d\boldsymbol{r}\varepsilon_{XC}[n(\boldsymbol{r}), \nabla n(\boldsymbol{r})]n(\boldsymbol{r}). \tag{3.78}$$

Equation (3.78) expresses exchange and correlation functional as an integral of all space for a function of local density and the gradient of the density $\nabla n(\boldsymbol{r})$. Most GGA functionals are constructed with the correction being a term added to the LDA functional. In 1996 Perdew *et al.* [39] introduced a function, within the LDA expression, which is a gradient expansion function $F_x(s)$:

$$E_{XC}^{GGA-PBE}[n(\boldsymbol{r})] = \int d\boldsymbol{r}\, n(\boldsymbol{r})\varepsilon_{XC}^{hom}[n(\boldsymbol{r})]F_X(s), \tag{3.79}$$

$$F_X(s) = 1 + k - \frac{k}{1+\frac{\mu s^2}{k}}, \tag{3.80}$$

$$s = const.\times \frac{|\nabla n|}{n^{4/3}}. \tag{3.81}$$

The expression (3.79) is named PBE functional flavour. In equation (3.81) the gradient of the density is normalized (dimensionless). Therefore, for constant gradient: $\nabla n = 0, s = 0$. Using $s = 0$ in equation (3.80) returns a $F_X(s)$ value of 1 thus returning equation (3.79) back to the exchange and correlation energy functional $E_{XC}^{LDA}[n(\boldsymbol{r})]$ of the uniformly distributed electron gas (UEG).

PBE functional and its parameters are the most commonly used, however through different calculations, different values of the parameters are obtained [40, 41]; Gradient Expansion: $\mu = 0.1235$, Becke-Lee-Yang-Parr (BLYP) (1998): $\mu = 0.2743$ and PBE (1996): $\mu = 0.2195$. GGA functionals may work better than the LDA functionals especially for systems with defects and large variations in electron densities [26, 38]. However, GGA always underestimates the band gap (E_g) of a material [42]. The model of DFT+U or GGA+U was developed to address the shortcomings of LDA and GGA functionals [43].

3.7.3 GGA+U

GGA+U is based on descriptive functionals build from the Hubbard model and is one of the simplest techniques applied to ground state of correlated systems. The total energy of a system for GGA+U approach is defined as [44, 45]:

$$E^{DFT+U}[n(\boldsymbol{r}),\hat{n}] = E^{DFT}[n(\boldsymbol{r})] + E^{U}[\hat{n}] - E^{dc}[\hat{n}]. \tag{3.82}$$

$E^{DFT}[n(\boldsymbol{r})]$ is the DFT total energy functional, $E^{U}[\hat{n}] = \frac{1}{2}U\sum_{i\neq j} n_i n_j$ is the electron-electron interaction and is the term that contains the Hubbard U used to model the localized states. Interestingly, a part of $E^{U}[\hat{n}]$ is already present in $E^{DFT}[n(r)]$ and to prevent double-counting, $E^{dc}[\hat{n}] = UN(N-1)/2$ is deducted in (3.82), $N = \sum_i n_i$ [45, 46]. Therefore,

$$E^{DFT+U}[n(\boldsymbol{r}),\hat{n}] = E^{DFT}[n(\boldsymbol{r})] + \frac{1}{2}U\sum_{i\neq j} n_i n_j - UN(N-1)/2. \tag{3.83}$$

The orbital eigenvalues, which is the energy per density, is obtained by taking the derivative with respect to density of that orbital,

$$\varepsilon_i = \frac{\partial E^{DFT+U}[n(\boldsymbol{r}),\hat{n}]}{\partial n_i}. \tag{3.84}$$

Through mathematical manipulations [45, 46, 47]:

$$\varepsilon_i = \varepsilon_i^{DFT} + U\left(\frac{1}{2} - n_i\right). \tag{3.85}$$

Therefore, for occupied orbitals ($n_i = 1$), equation (3.85) shifts DFT energy of the orbitals by $-U/2$ and for unoccupied orbitals ($n_i = 0$), the DFT energy of orbitals is shifted by $+U/2$. GGA+U potential is thus given by [45]:

$$V^{DFT+U}[r] = V^{DFT} + U\left(\frac{1}{2} - n_i\right)P_i, \tag{3.86}$$

where P_i is the projection operator for localized orbitals.

GGA+U exchange correlation is mainly used for strongly correlated first-principles calculations because of its simple expressions, low computational costs and easy implementation of energy derivatives such as atomic forces and stresses [46, 47]. In this

work, GGA+U functionals were used to accurately study structural and electronic properties of monolayer doped SnS_2.

3.8 Plane Wave and Pseudopotential Method

In this section, computational implementation of DFT is demonstrated. The many body problem is mapped onto an effective single-particle problem. This still poses a problem of handling infinite non-interacting electrons moving in a static potential of infinite nuclei or ions. Thus, a wavefunction must be calculated for each electron and each wavefunction must extend over an entire solid. This will require an infinite basis set to expand each wavefunction. Bloch's theorem provides a technique of handling the electronic wavefunctions for periodic solids.

3.8.1 Bloch's Theorem

In a periodic solid, Bloch's theorem states that the wavefunction can be expressed as a product of the cell periodic parts [14, 48]. Therefore, Bloch's theorem states that:

$$\psi_i(\boldsymbol{r}) = e^{i\boldsymbol{k}.\boldsymbol{r}} u_i(\boldsymbol{r}). \tag{3.87}$$

The term $u_i(\boldsymbol{r})$ contains periodicity of the lattice [24]:

$$u_i(\boldsymbol{r}) = \sum_{\boldsymbol{G}} c_i, G e^{i\boldsymbol{G}.\boldsymbol{r}}, \tag{3.88}$$

where $\boldsymbol{G}$ is the reciprocal lattice vector defined by $\boldsymbol{G}.\boldsymbol{l} = 2\pi m$, $\boldsymbol{l}$ symbolises the lattice vector of a crystal, m is an integer and, from DFT, $\boldsymbol{r}$ is the position vector of the electron density. Thus, this electronic wavefunction can be expressed as a plane-wave expansion [24]:

$$\psi_i(\boldsymbol{r}) = \sum_{\boldsymbol{G}} c_i, \boldsymbol{k} + \boldsymbol{G} e^{i(\boldsymbol{k}+\boldsymbol{G}).\boldsymbol{r}}. \tag{3.89}$$

The plane-wave coefficients, $c_i, \boldsymbol{k}+\boldsymbol{G}$, are used to define the size of the array. The maximum length of the $\boldsymbol{G}$ vectors can be further limited through defining a kinetic energy cut-off [2, 9]:

$$E_{cut} = \frac{1}{2}|\boldsymbol{k}+\boldsymbol{G}_{max}|^2. \tag{3.90}$$

Accurately solving these equations using iterative methods results in precision of the DFT code.

3.8.2 k-point sampling

For a periodic system, Bloch's theorem transforms the integral of an infinite number of k-points in real space to a finite number of k-points in reciprocal space. This reciprocal space is known as the Brillouin zone (BZ) [24, 49]. The integral over the BZ is expressed as:

$$f(\boldsymbol{r}) = \frac{\Omega}{(2\pi)^3}\int_{BZ} F(\boldsymbol{k})d^3k, \tag{3.91}$$

where Ω is the unit cell volume and $F(\boldsymbol{k})$ is the Fourier transformation term. Integrating over the BZ generates electronic properties such as Band Energy, DOS, charge density and total energy. There is a number of techniques to sample k-points in the BZ [50, 51], however this work uses the Monkhorst and Pack method [52] which determines k-points according to the crystal studied. The Fourier transformation term can be defined as [50, 51]:

$$F(\boldsymbol{k}) = f_0 + \sum_{m=1} A_m(\boldsymbol{k}), \tag{3.92}$$

where $A_m(\boldsymbol{k})$ is the transformation term expressed as:

$$A_m(\boldsymbol{k}) = \sum e^{i\boldsymbol{k}.\boldsymbol{r}}. \tag{3.93}$$

The sum in equation (3.92) converges as the exponential term in equation (3.93) moves towards zero at large $\boldsymbol{r}$ vectors. According to Meyer [49], metals require a small k-points sample to obtain well-converged results, while insulators and semi-conductors require a large k-points sample because of discontinuity at the Fermi surface [9, 24, 49]. Methfessel

and Paxton solved this problem by developing smearing [53], which ensures that the integrated function becomes smeared and, thus is not discontinued. This allows exponential convergence with a small k-points sample.

3.8.3 Pseudopotential Approximation

This phenomenon addresses the different types of electron energies and consequently the contributions between the core electrons and valence electrons. As is well known, the core electrons are bound and highly localized near the nucleus. The wavefunctions of core electrons oscillate with a rapid frequency [54]. Thus, these bound core electrons are inert and do not contribute to the chemical bonding. Their distribution is highly unaffected by different chemical environments, referred to as Frozen-Core approximation [55]. On the other hand, valence electrons are loosely bound, more energetic, participate in chemical bonding and they determine a material's physical and chemical properties. The difference between the core and valence electrons is what lead to the development of Pseudopotential (PP) Approximation method which has been a very effective approach [56].

The PP method replaces the wavefunctions of core electrons with smoothly varying pseudo wavefunctions, while valence electrons are replaced by weaker PP wavefunctions [57]. Therefore, there exists a relationship between all-electron (AE) and the PP wavefunctions which is demonstrated in figure 3.1.

There are major constructive influences by PP method which enabled easier study of materials using computational techniques. The major requirement which PPs have met is that they are transferable, meaning the same PP could be used per element even in different chemical environments [58]. However, one major challenge is that the construction of PPs for each atom involves many empirical parameters [9, 49, 59]. A solution to this was introduced by Blöchl in 1994 [60], called the projector augmented wave (PAW) method.

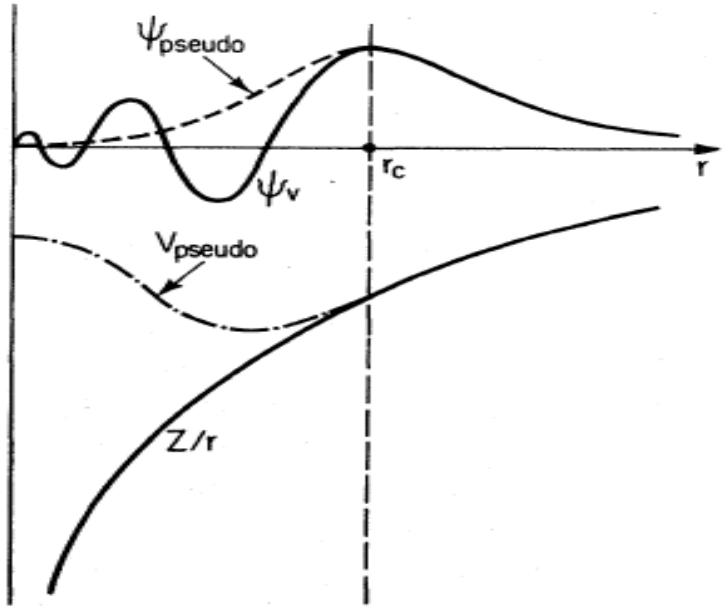

Figure 3.1: Schematic diagram of wavefunctions of AE (solid-lines) and PP (dashed-lines) with respect to the radius. The AE and PP intercept at a radius of oscillation called the cut-off oscillation or cut-off frequency [9, 24].

3.8.4 Projector Augmented Wave (PAW) Method

Similar to PP method, the PAW method minimizes complex electron-ion interactions. The PAW method corrects the shape difference between AE and PP wavefunctions [61]. Application of the PAW method is advantageous. The inert core electrons have no impact on the PAW method, thus, this reduces computational costs [60]. Moreover, this method uses the potential that has been acquired from the full charge density [60, 61]. PAWs are computationally applied during the solving procedure of K-S equations. The PAW method works well, with improved computational accuracy, for first-row and transition elements [60, 61]. Kresse and Joubert [59] showed that well-constructed PPs and Vanderbilt's ultrasoft PPs (USPPs) [62], in many cases, give results that are identical to the PAW method.

3.9 DFT Calculation

A first-principles plane-wave pseudopotential [4] method was carried out using quatum-espresso simulation package (QESP) [63, 64]. The exchange and correlation energy functional was described by the generalized gradient approximation (GGA), using the Perdew, Burke and Ernzerhof (PBE) [39] description for the electron-iron interaction. As mentioned, GGA tends to underestimate the band gap [42]. This is corrected by including the Hubbard U (DFT+U/GGA+U) correction [43] with U = 8 eV to obtain band gap values close to the theoretical value. A kinetic energy cut-off of 450 eV was used as a plane-wave basis set to expand Kohn-Sham equations. K-points were converged with a Monkhorst-Pack grid [65, 66] of $8 \times 8 \times 1$ for Brillouin zone sampling. Successful calculation of the cohesive energy were achieved through including smearing, which considers the distribution of electrons about the Fermi level, in the calculation using the Methfessel Paxton technique. The spin was excluded, which is a default setting in quantum espresso, or using $nspin = 0$ parameter. Thus, excluding spin also excludes magnetization, which is also a default setting in the quantum espresso package, or using the $starting\_magnetization = 0$ parameter. A study was conducted on the effects of dopants C and Si on the stability, electronic structure, charge density difference and band edge alignment of a $5 \times 5 \times 1$ supercell of SnS_2.

BIBLIOGRAPHY

[1] Piela, L. (2007). *Ideas of quantum chemistry*. Amsterdam: Elsevier, pp.55-89.

[2] Mapasha, R. (2014). *Van der Waals density functional studies of hydrogenated and lithiated bilayer graphene*. Ph.D. University of Pretoria, pp.30-76.

[3] Strang, G. (2017). *Calculus*. Wellesley, MA: Wellesley-Cambridge Press.

[4] Martin R. (2004). *Electronic Structure*. Cambridge University Press, pp.30 – 45.

[5] Sherrill, C. (2005). *The Born-Oppenheimer Approximation*. School of Chemistry and Biochemistry Georgia Institute of Technology.

[6] Echenique, P. and Alonso, J. (2007). *A mathematical and computational review of Hartree–Fock SCF methods in quantum chemistry*. Molecular Physics, 105(23-24), pp.3057-3098.

[7] Hartree, D. (1928). *The Wave Mechanics of an Atom with a Non-Coulomb Central Field. Part I. Theory and Methods*. Mathematical Proceedings of the Cambridge Philosophical Society, 24(1), pp.89-110.

[8] Marder, M. (2010). *Condensed Matter Physics*. John Wiley & Sons.

[9] Sholl, D. and Steckek, J. (2009). *Density functional theory*. Hoboken (New Jersey): Jonh Wiley & Sons.

[10] Maroulis, G. and Simos, T. (2009). *Computational methods in science and engineering*. Melville, N.Y.: American Institute of Physics.

[11] Ackermann, G. and Eichler, J. (2007). *Holography*. Germany: Wiley-Vch, pp.275-280.

[12] Andrew, R. (2013). *First Principles Studies of Si-C Alloys*. Ph.D. University of Pretoria, pp.16-44.

[13] Dirac, P. (1989). *The principles of quantum mechanics*. Oxford: Clarendon Pr., pp.17-52.

[14] Grosso, G. and Pastori Parravicini, G. (2014). *Solid state physics*. Amsterdam: Academic Press, an imprint of Elsevier, pp.136-163.

[15] Kohanoff, J. and Gidopoulos, N. (2003). *Density Functional Theory: Basics, New Trends and Applications*. 2nd ed. Handbook of molecular physics and quantum chemistry, pp.532-568.

[16] Harris, F. (1978). *Hartree-like methods in electronic structure theory*. International Journal of Quantum Chemistry, 13(2), pp.189-198.

[17] Tsuneda, T. (2014). *Density Functional Theory in Quantum Chemistry*. Dordrecht: Springer, pp.35 - 63.

[18] Kaxiras, E. (2022). *9780511755545: Atomic and Electronic Structure of Solids - AbeBooks - Kaxiras, Efthimios: 0511755546*. [online] Abebooks.com. Available at: <https://www.abebooks.com/9780511755545/Atomic-Electronic-Structure-Solids-Kaxiras-0511755546/plp> [Accessed 3 June 2022].

[19] Gonis, A. (2014). *Variational Properties of Density Functional Theory*. World Journal of Condensed Matter Physics, 4(3).

[20] Slater, J. (1951). *A Simplification of the Hartree-Fock Method*. Physical Review, 81(3), pp.370-390.

[21] Koch, W. and Holthausen, M. (2015). *A chemist's guide to density functional theory*. John Wiley & Sons.

[22] Harker, A. (2015). *Materials Modelling using Density Functional Theory: Properties and Predictions, by Giustino Feliciano*. Contemporary Physics, 57(1), pp.130-151.

[23] Pitzer, K. (1960). *The Nature of the Chemical Bond and the Structure of Molecules and Crystals: An Introduction to Modern Structural Chemistry*. Journal of the American Chemical Society, 82(15), pp.4111-4131.

[24] Payne, M., Teter, M., Allan, D., Arias, T. and Joannopoulos, J. (1992). *Iterative minimization techniques for ab initio total energy: molecular dynamics and conjugate gradients*. Review of modern physics, 64.

[25] Kohn, W. (1999). *Nobel Lecture: Electronic structure of matter—wave functions and density functionals*. Reviews of Modern Physics, 71(5), pp.1253-1266.

[26] Burke, K. (2007). *The ABC to DFT*. Department of Chemistry, University of California, Irvine, CA 92697.

[27] Hohenberg, P. and Kohn, W. (1964). *Inhomogeneous Electron Gas*. Physical Review, 136(3B), pp.B864-B871.

[28] MacDonald, J. (1933). *Successive Approximations by the Rayleigh-Ritz Variation Method*. Physical Review, 43(10), pp.830-833.

[29] Levy, M. (1982). *Electron densities in search of Hamiltonians*. Physical Review A, 26(3), pp.1200-1208.

[30] Lieb, E. (1982). *Physics as natural philosophy*. MIT Press Cam bridge, pp.110-112.

[31] Kohn, W. and Sham, L. (1965). *Self-Consistent Equations Including Exchange and Correlation Effects*. Physical Review, 140(4A), pp.A1133-A1138.

[32] Gidopoulos, N. (1998). *Kohn-Sham equations for multicomponent systems: The exchange and correlation energy functional*. Physical Review B, 57(4), pp.2146-2152.

[33] Baerends, E. (2000). *Perspective on Self-consistent equations including exchange and correlation effects.* Theoretical Chemistry Accounts: Theory, Computation, and Modeling (Theoretica Chimica Acta), 103(3-4), pp.265-269.

[34] Tong, B. and Sham, L. (1966). *Application of a Self-Consistent Scheme Including Exchange and Correlation Effects to Atoms*. Physical Review, 144(1), pp.1-4.

[35] Mattsson, A., Schultz, P., Desjarlais, M., Mattsson, T. and Leung, K. (2004). *Designing meaningful density functional theory calculations in materials science—a primer*. Modelling and Simulation in Materials Science and Engineering, 13(1), pp.R1-R31.

[36] Dirac, P. (1930). *Note on Exchange Phenomena in the Thomas Atom*. Mathematical Proceedings of the Cambridge Philosophical Society, 26(3), pp.376-385.

[37] Kleinman, L. (1974). *Gradient term in the Kohn-Sham exchange-correlation potential*. Physical Review B, 10(6), pp.2221-2225.

[38] Shul'man, A. and Posvyanskii, D. (2014). *Truly self-consistent solution of Kohn-Sham equations for extended systems with inhomogeneous electron gas*. Journal of Physics: Conference Series, 510, p.012029.

[39] Perdew, J., Burke, K. and Ernzerhof, M. (1996). *Generalized Gradient Approximation Made Simple*. Physical Review Letters, 77(18), pp.3863-3870.

[40] Perdew, J. and Wang, Y. (1992). *Accurate and simple analytic representation of the electron-gas correlation energy*. Physical Review B, 45(23), pp.13244-13249.

[41] Odashima, M. and Capelle, K. (2008). *Empirical analysis of the Lieb-Oxford bound in ions and molecules*. International Journal of Quantum Chemistry, 108(13), pp.2428-2432.

[42] Bhavani, J. and John, R. (2020). *Band Gap Engineering of Cu_2ZnSnX_4 (X = S, Se and Te) Quaternary Semiconductors Using PBE-GGA, TB-mBJ and mBJ+U Potentials*. International Journal of Materials, Mechanics and Manufacturing, 8(1).

[43] Lieb, E. and Oxford, S. (1981). *Improved lower bound on the indirect Coulomb energy*. International Journal of Quantum Chemistry, 19(3), pp.427-439.

[44] Hubbard, J. (1967). *Electron correlations in narrow energy bands VI. The connexion with many-body perturbation theory*. Proceedings of the Royal Society of London. Series A. Mathematical and Physical Sciences, 296(1444), pp.99-118.

[45] Côté, M., *Introduction to DFT+U*. Physics Department, Université de Montréal.

[46] Kirchner-Hall, N., Zhao, W., Xiong, Y., Timrov, I. and Dabo, I. (2021). *Extensive Benchmarking of DFT+U Calculations for Predicting Band Gaps*. Applied Sciences, 11(5), p.2395.

[47] Elenewski, J. and Hackett, J. (2012). *A GGA+U approach to effective electronic correlations in thiolate-ligated iron-oxo (IV) porphyrin*. The Journal of Chemical Physics, 137(12), p.124311.

[48] Ashcroft, N. W. and Mermin, N. D. (1976). *Solid State Physics*. Thomson Learning Inc., 25, pp.760-765.

[49] Meyer, B. (2006). *The Pseudopotential Plane Wave Approach.* Computational Nanoscience: do it yourself, 31, pp.71-83.

[50] Chadi, D. and Cohen, M.L. (1973). *Special Points in the Brillouin Zone*. Physical Review B, 8, p.5747.

[51] Moreno, J. and Soler, J.M. (1992). *Optimal Meshes for Integrals in Real- and Reciprocal-Space Unit Cells*. Physical Review B, 45, p.13891.

[52] Monkhorst, H.J. and Pack, J.D. (1976). *Special Points for Brillouin-Zone Integrations*. Physical Review B, 13, p.5188.

[53] Methfessel, M. and Paxton, A. (1989). *High-Precision Sampling for Brillouin-Zone Integration in Metals*. Physical Review B, 40, p.3616.

[54] Bialynicki-Birula, I. and Bialynicka-Birula, Z. (2010). *Simple model of self-supported deformed states of isolated atoms*. Physical Review A, 81(1).

[55] McEachran, R., Tull, C. and Cohen, M. (1968). *Frozen core approximation for atoms and atomic ions*. Canadian Journal of Physics, 46(23), pp.2675-2678.

[56] Schwerdtfeger, P., (2011). *The Pseudopotential Approximation in Electronic Structure Theory*. ChemPhysChem, 12(17), pp.3143-3155.

[57] Filippetti, A. and Bachelet, G. (2005). *Pseudopotential Method*. Encyclopedia of Condensed Matter Physics, pp.431-440.

[58] Chelikowsky, J. (2011). *Electrons in Semiconductors: Empirical and ab initio Pseudopotential Theories*. Comprehensive Semiconductor Science and Technology, pp.1-41.

[59] Kresse, G., Joubert, D. (1999). *From Ultrasoft Pseudopotentials to the Projector Augmented-Wave Method*. Physical Review B, 59, 1758.

[60] Blöchl, P. E. (1994). *Projector Augmented-Wave Method*. Physical Review B, 50 (24), 17953.

[61] Blöchl, P. E., Först, C. J., Schimpl, J. (2003). *Projector Augmented Wave Method: Ab Initio Molecular Dynamics with Full Wave Functions*. Bulletin of Materials Science, 26, 33-41.

[62] Vanderbilt, D. (1990). *Soft Self-Consistent Pseudopotentials in a Generalized Eigenvalue Formalism*. Physical Review B, 41, 7892.

[63] Giannozzi, P. *et al.* (2009). *Quantum Espresso: A modular and open-source software project for quantum simulations of materials*. Journal of Physics: Condensed Matter, 21(39), p. 395502. Available at: https://doi.org/10.1088/0953-8984/21/39/395502.

[64] Scandolo, S. *et al.* (2005). *First-principles codes for Computational Crystallography in the quantum-espresso package*. Zeitschrift für Kristallographie - Crystalline Materials, 220(5-6), pp. 574–579. Available at: https://doi.org/10.1524/zkri.220.5.574.65062.

[65] Wan, W. (2018) *Efficient Generation of K-point Grids for Quantum ESPRESSO and Catalytic Role of CoP (101) for Electrochemical Hydrogen Evolution Compared with Pt (100) and Pt (111)*. Thesis. Johns Hopkins University.

[66] Wang, Y. *et al.* (2021). *Rapid generation of optimal generalized Monkhorst-pack grids*. Computational Materials Science, 187, p. 110100. Available at: https://doi.org/10.1016/j.commatsci.2020.110100.

CHAPTER 4: RESULTS AND DISCUSSIONS

4.1 Brief introduction

In this chapter, the effects of doping pristine SnS_2 monolayer with a single Carbon and Silicon atom are studied with an effort to enhance its photocatalytic properties. Increased photoreception, thermodynamic stability and charge mobility would enable the material to act as a photoelectrode for water splitting. C/Si doping is proposed as the doping strategy to improve the photocatalytic properties of SnS_2. Various C and Si doped configurations are identified and their effects on the electronic structure are investigated.

Therefore, properties of SnS_2 as a photocatalytic water splitter are investigated in this chapter through performing a detailed DFT study which incorporates the GGA+U method. The structures of pristine and doped SnS_2 monolayer configurations were constructed using quantum espresso simulation package (QESP) [1] and viewed using XCrysDen [2]. Equilibrium properties, test of convergence, total and partial densities of states, charge density dynamics, and band edge alignment are examined. Carbon doped calculations are performed first then silicon doped calculations.

4.2 Analysis of energetic stability, structural and electronic properties of pristine SnS_2 monolayer

4.2.1 Structure of pristine SnS_2 monolayer

The structural aspects of pristine SnS_2 monolayer have been discussed in detail in chapter one. The SnS_2 monolayer has two phases namely; 1T phase and 2H phase. The 1T phase, which is the phase investigated in this study and is illustrated in figure 4.1, is more

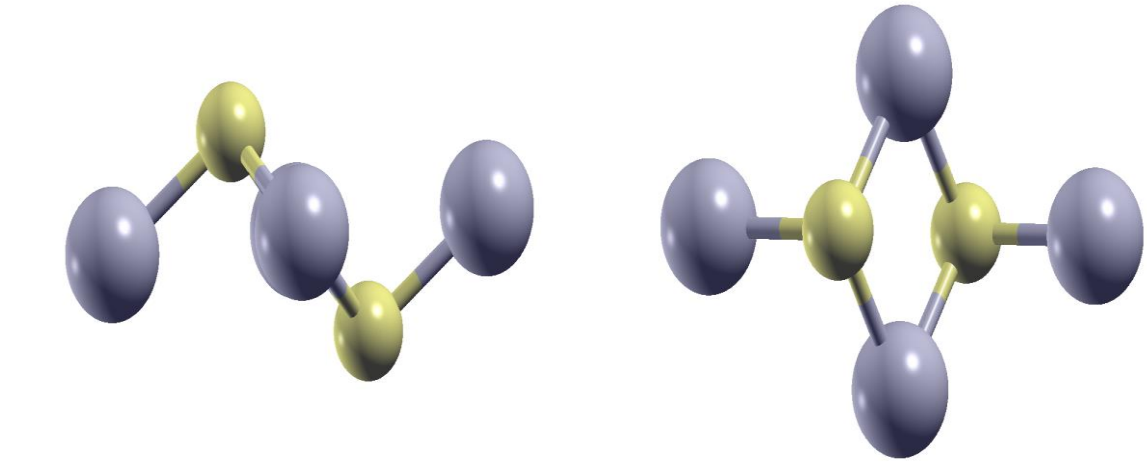

(a) (b)

Figure 4.1: The 1T structure of SnS_2 unit cell with the purple spheres representing tin (Sn) atoms and yellow spheres representing sulphur (S) atoms. (a) The side view of 1T structure of SnS_2 and (b) the top view of 1T structure of SnS_2.

thermodynamically stable than the 2H phase [3]. The 1 × 1 hexagonal unit cell consists of four Sn atoms sandwiched between two S atoms, with one S atom at the top and the other S atom at the bottom in an alternating manner. The four Sn atoms each contribute only ¼ of their atom in the unit cell. The input file, used to construct the 1T structure of SnS_2, consists of a total number of three atoms in the unit cell with coordinates (0.0000, 0.0000, 0.0000) for Sn, (0.3333, 0.6667, 0.5830) for S and (0.6667, 0.3333, 0.4170) for the other S. This unit cell is repeated periodically to form the supercells.

4.2.2 Test of convergence for the cut-off energy and k-points

In DFT calculations, to obtain the accurate and reproducible calculated properties, it is necessary to perform the tests of convergence of the cut-off energy and k-points of the material structure. A suitable cut-off energy is required for the expansion of the plane waves in the Fourier transformation and an appropriate number of k-points will adequately sample the first Brillouin zone. For the expansion of the plane waves, a series of SCF calculations were performed for different cut-off kinetic energies ranging from 200 to 800 eV (increments of 50 eV were considered) at a fixed k-points value. Figure 4.2 presents the

obtained total energies of SnS_2 monolayer structure with respect to change in cut-off energies. The total energy variations start to be insignificant at 400 eV, since the plot shows constant feature. The total energies are considered to have converged at the point which the energy differences are very minimal (less than 2meV) in comparison to the nearest point on the plot. Thus, 450 eV cut-off energy is considered to be sufficient and any value beyond this will not have any significant effect on the precision of the results. This value is very close to the converged value of 500eV considered in the works of Burton *et al.* [4].

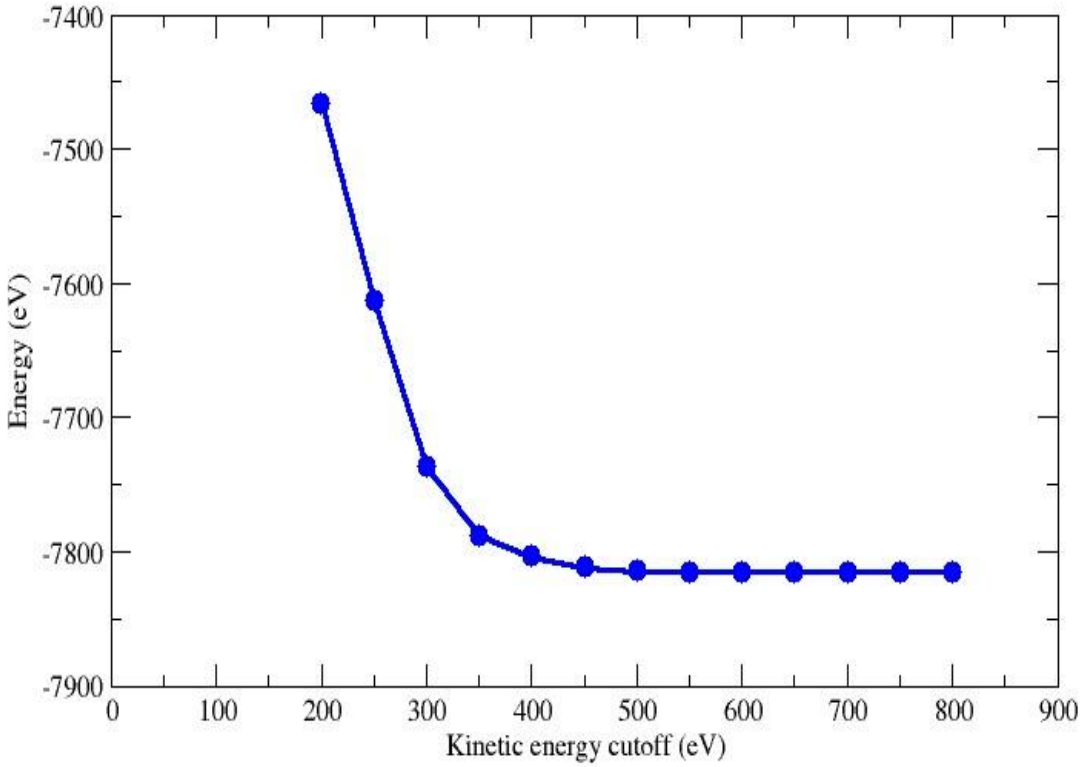

Figure 4.2: The calculated total energies versus cut-off energies for SnS_2 unit cell.

After obtaining the suitable cut-off energy, an appropriate number of k-points for integration over the Brillouin zone of SnS_2 monolayer was evaluated. There are numerous methods of generating the k-points [5, 6]. In this work, the Monkhorst and Pack [7] k-mesh grid was used to generate the discrete k-points of SnS_2 monolayer. Figure 4.3, presents the

total energy variation with respect to k-meshes change along the x, y, z directions. As can be observed, the total energy interval between the k-mesh grids of $8 \times 8 \times 1$ to $9 \times 9 \times 1$ has reached convergence (total energy difference between two nearest points is within 1meV), thus no significant changes will be noticed for any DFT calculations between these points. Therefore, for all calculations in this work, cut-off energy of 450 eV and k-point mesh of $8 \times 8 \times 1$ were used which are in close agreements with the works of Burton *et al.* [4] and Eads *et al.* [8].

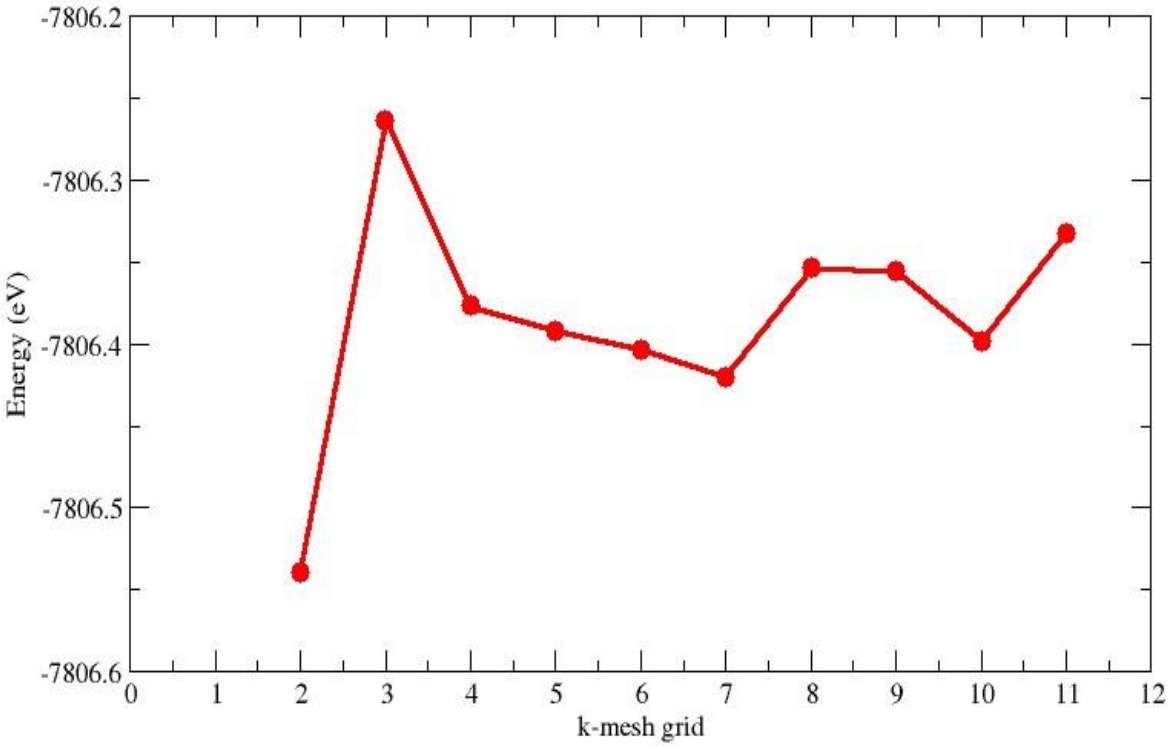

Figure 4.3: Total energy versus k-mesh grids, in which a k-mesh value of n along the x-axis represents a Monkhorst Pack grid of $n \times n \times 1$.

4.2.3 Equilibrium properties of SnS_2 monolayer

A full geometry optimization (FGO) calculation option (VC-relax criterion in PW-scf quantum espresso packages) was initially performed to obtain the equilibrium properties of SnS_2 monolayer. FGO calculations relax the atomic positions, the cell shape and volume

change to absolute minimum energy positions, defined by Hellman Fynman theorem [9]. A sufficient cut-off energy of 450eV (as shown in Figure 4.2) and k-mesh grid of $8 \times 8 \times 1$ (as shown in Figure 4.3) were used to perform FGO calculations of SnS_2 monolayer to obtain the equilibrium lattice constants (a_0) and bond lengths (d_{Sn-S}) as presented in table 4.1.

It is observable in table 4.1 that measured values are in close proximity to other DFT works and experimental values. The lattice constant ($a_0 = 3.64$Å) is exactly the same as the experimental, however differs by 1.62% from other DFT values ($a_0 = 3.70$Å), difference in values could be attributed to other DFT using a GGA functional. The bonding length ($d_{Sn-S} = 2.58$Å), which is the closest distance between any two atoms and in this case being Sn and S bond, was also measured and found to be 0.39% different from both the other DFT ($d_{Sn-S} = 2.59$Å) and experimental works ($d_{Sn-S} = 2.57$Å).

Cohesive energy (E_{Coh}), as mentioned in Chapter 1, measures the structure's overall relative chemical stability. In this work, cohesive energy is deduced from the total energy of SnS_2 monolayer as the difference between a total electronic energy and the sum of the energies of its constituent atoms at infinite separation [10]. The $E_{Coh/atom}$ was measured, mathematically, using the below equation [11]:

$$E_{Coh/atom} = \frac{\sum E_{atoms} - E_{system}}{N}. \quad (4.1)$$

Since N represents the number of atoms in the unit cell, equation 4.1 is thus the cohesive energy per atom. The SnS_2 unit cell consists of 3 atoms which has the form MX_2. Therefore, cohesive energy per atom of SnS_2 monolayer is calculated as follows:

$$E_{Coh/atom} = \frac{E_T[Sn] + 2E_T[S] - E_T[SnS_2]}{3}. \quad (4.2)$$

To measure the energy of the individual atoms ($E_T(Sn)$ and $E_T(S)$), a Sn and S atom were each placed at the central lattice site of a BCC lattice [12] then the energies of the individual Sn and S in the BCC structure were calculated using PW-scf in quantum espresso package. Using equation (4.2), the cohesive energy per atom for pristine SnS_2 was calculated and compared with other DFT and experimental values, as can be observed in

table 4.1. The cohesive energy per atom of this work is less than that of other DFT works by a value of 13.18%, but very close to the experimental value by 2.64%. The bigger deviation from other DFT works could be due to SnS_2 monolayer, in other DFT, being constructed using Vienna *Ab initio* Simulation Package (VASP) implemented using GGA+HSE06 exchange correlation functional. Since cohesive energy refers to binding, a positive cohesive energy value indicates a high stability of the SnS_2 monolayer.

4.2.4 Electronic properties of pristine SnS_2 monolayer obtained using GGA+U

In Chapter 3, it was mentioned that GGA functionals tend to underestimate the band gap, thus giving inaccurate and inconclusive results [13]. Including the Hubbard U correction term in the GGA functional is a way of mitigating this problem [14]. In this study, different band gaps (E_g) of pristine SnS_2 monolayer were measured from the density of states with varying U parameter, from 0 eV to 10 eV and presented in figure 4.4 below.

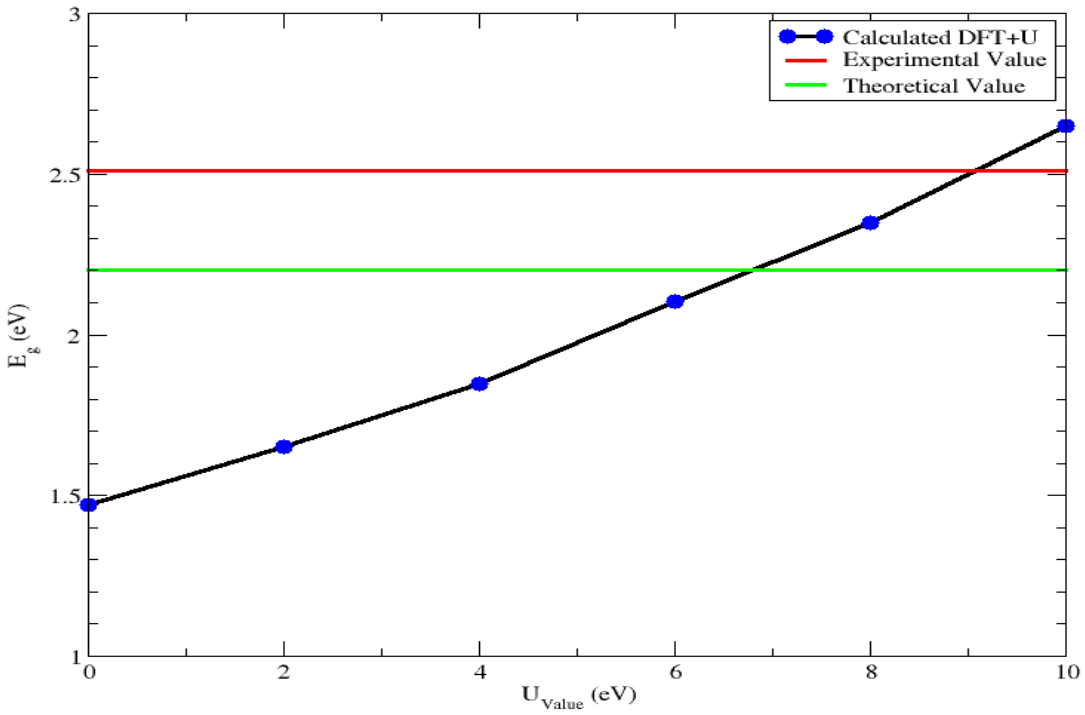

Figure 4.4: Plot of electronic band gap for SnS_2 against varying U values. The green and red lines depict the band gap interval of SnS_2 from other works, with green line representing the theoretical value and red line representing the experimental value. It is observable that the U value of 8 eV is in between both the theoretical and experimental interval.

Figure 4.4 shows there is an increasing trend in band gap values with increasing U parameter value. A U value of 8 eV produced a band gap value of 2.34 eV, which was the only value that fell within the experimental range of 2.20 to 2.51 eV [1, 15] for pristine SnS_2 monolayer. The total (TDOS) and partial density of states (PDOS) for standard GGA ($U = 0$ eV) and GGA+U ($U = 8$ eV) are shown in figure 4.5 (a) and (b), respectively. The 0 eV and 8 eV U parameters give the different band gaps of 1.45 eV and 2.34 eV, respectively, for the SnS_2 system.

In figure 4.5, the Fermi level was translated to the 0^{th} position on the energy-axis for an even comparison of the two band gaps for $U = 0\ eV$ and $U = 8\ eV$. The partial densities of states (PDOS) for both $U = 0\ eV$ and $U = 8\ eV$ reveal that the valence band maximum (VBM) is mainly contributed by 3p states of sulphur and the conduction band minimum (CBM) is contributed by a hybridization of 3p states of sulphur and 5s sates of tin. The PDOS in figure 4.5 accurately agree with the DFT work by Zhu *et al.* [16], thus indicating the suitability of our calculations. For accurate and conclusive results, all calculations will be based on a U parameter value of 8 eV hence forth unless stated otherwise. All measured properties and their theoretical equivalents are displayed in table 4.1.

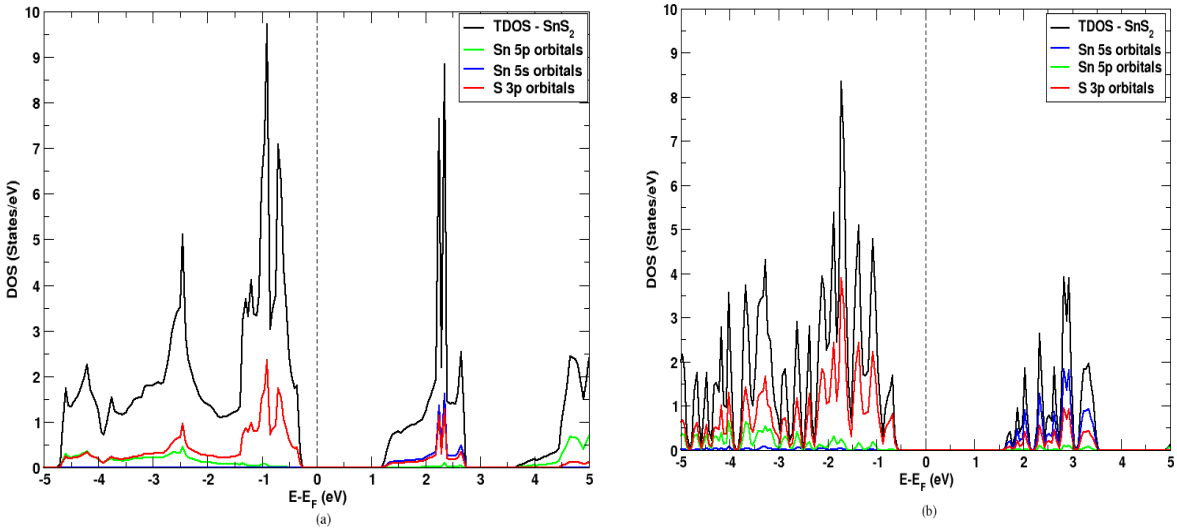

Figure 4.5: Electronic density of states of pristine SnS_2 for different U parameters. (a) TDOS and PDOS for standard GGA ($U = 0\ eV$) and (b) TDOS and PDOS for GGA+U ($U = 8\ eV$) simulations.

Table 4.1: A summary of equilibrium properties of hexagonal pristine SnS_2 monolayer. a_0 is the lattice constant, d_{Sn-S} is the bond length between nearest neighbour Sn and S atom, E_g is the band gap and $E_{Coh/atom}$ is the cohesive energy per atom. The interlayer distance is set to $c = 15$Å because of the 2D nature of SnS_2, an appreciable space should be in between the layers.

	a_0 (Å)	d_{Sn-S} (Å)	$E_{Coh/atom}$ (eV/atom)	E_g (eV)
This work	3.64	2.58	3.03	2.35
Other DFT	3.70[1](1.62%)	2.59[1](0.39%)	3.49[17](13.18%)	2.20[1](6.38%)
Experimental	3.64[15](0%)	2.57[15](0.39%)	2.95[18](2.64%)	2.51[15](6.3%)

Therefore, supercells were periodically constructed from this unit cell with all the above parameters from which a detailed study can be achieved on the photocatalytic effects of carbon doped and silicon doped SnS_2.

4.3 Carbon doping on SnS_2 monolayer

Doping with C is the technique used in this section to improve photocatalytic properties of SnS_2 monolayer. We identified five different C doped configurations to be examined. The final doped product suitable for photocatalytic application should be a thermodynamically stable and experimentally synthesizable material under favourable conditions. Figure 4.6 shows the unrelaxed structures for the different C doped configurations considered for this study. Figure 4.6 (a) is a configuration of C adsorbed on an interstitial position (C_{Int}). To further explain the C_{Int} configuration, the C is placed at the centre of hexagon, directly above the bottom sulphur and at the same height as the top sulphurs. Figure 4.6 (b) is a configuration of C adsorbed on a S atom (C_{Ads-S}). Figure 4.6 (c) is a configuration of C adsorbed on a Sn atom (C_{Ads-Sn}), at the same height as the S atoms. Figure 4.6 (d) is a C substituting S configuration (C_{Sub-S}). Lastly, figure 4.6 (e) is a C substituting Sn configuration (C_{Sub-Sn}).

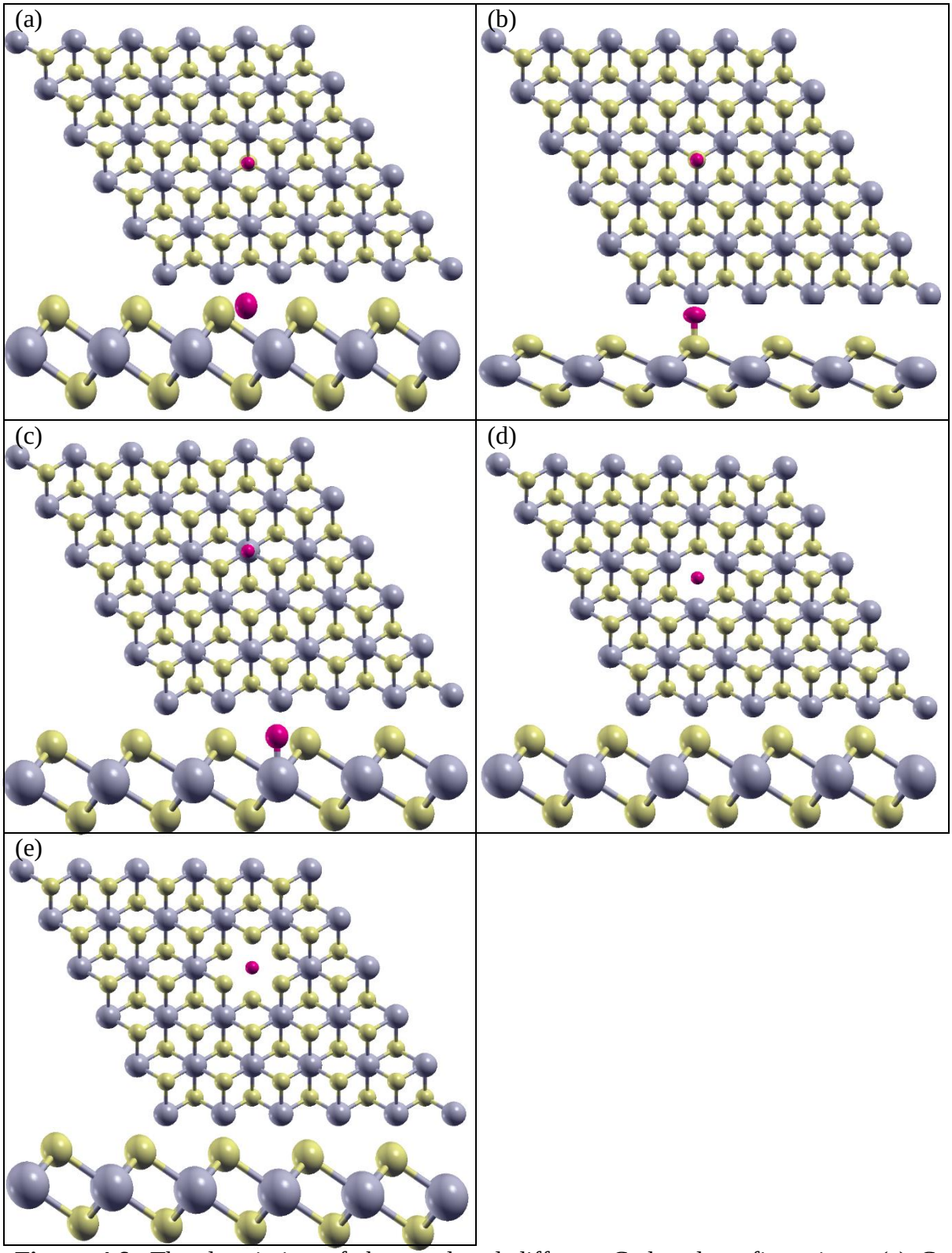

Figure 4.6: The description of the unrelaxed different C doped configurations: (a) C adsorbed on an interstitial position [C_{Int}], (b) C adsorbed on S [C_{Ads-S}], (c) C adsorbed on Sn [C_{Ads-Sn}], (d) C substituting S [C_{Sub-S}] and (e) C substituting Sn [C_{Sub-Sn}]. The C atom is represented by the magenta sphere, S atoms by the yellow spheres and Sn atoms by the purple spheres.

4.3.1 Energetic stability and structural properties of carbon doped configurations

In this study, formation energy E_f is used to examine the thermodynamic stability of doped SnS_2 systems [19]. The above structures were relaxed using FGO option and the obtained total energies were used in calculating their formation energies. The formation energies were obtained using the following equation (4.3) [19]:

$$E_f = E_{(dopedSnS_2)} - \left(E_{SnS_2} - \delta_{\mu_X} - \mu_C\right) - 1, \tag{4.3}$$

where E_{SnS_2} and $E_{(dopedSnS_2)}$ denote the pristine and doped supercell total energies, respectively. μ_C and δ_{μ_X} denote chemical potentials of C and the substituted atom, respectively, thus for the host lattice $X = S\ or\ Sn$. The chemical potential for C (μ_C) was calculated from energy of graphene and μ_X was calculated from the energy of a diatomic molecule in a large box ($10 \times 10 \times 10$). Since this study involves different types of doping i.e. adsorption, substitutions, etc., equation (4.3) takes the form of equation (4.4) – (4.6) depending on the doping type. In the interstitial doping and adsorption cases, the term μ_X is omitted from the formation energy equation, thus $\delta = 0$, and for substitutional doping $\delta = 1$. Consequently, formation energy for Sn substitution is calculated using equation (4.4) below;

$$E_f = E_{(dopedSnS_2)} - E_{SnS_2} - \mu_C + \delta_{\mu_{Sn}}. \tag{4.4}$$

For S substitution, equation (4.3) is reduced to equation (4.5),

$$E_f = E_{(dopedSnS_2)} - E_{SnS_2} - \mu_C + \delta_{\mu_S}. \tag{4.5}$$

For all adsorption and interstitial doping configurations, equation (4.3) is reduced to equation (4.6),

$$E_f = E_{(dopedSnS_2)} - E_{SnS_2} - \mu_C. \tag{4.6}$$

The calculated formation energies of all identified configurations are presented in figure 4.7 and their relaxed structures in figure 4.8. The formation energies are positive (endothermic), suggesting that an external energy should be supplied for formation to occur. Subsequently, the formation energies of these configurations differ in magnitude.

This is an indication that the formation of C doping in a SnS_2 monolayer greatly depend on the configuration.

The dopant-dopant interaction due to periodicity of the lattice can affect the formation energy. It is always advisable to consider supercell convergence tests before making conclusion of the results [20]. In this study, the supercell convergence tests were also considered. The formation energies of all identified doping configurations for different supercell sizes of 3×3, 4×4, 5×5 and 6×6 were calculated and presented in figure 4.7. Except for C_{Sub-Sn}, the formation energies of other identified doping configurations have converged showing maximum difference of almost 0.92 eV from 3×3 supercell onwards. This could be the reason other studies used 3x3 and 4x4 supercells in their investigations. These include the studies done on Na ion diffusion into a 3×3 SnS_2 monolayer by Samad *et al.* [21] and Fe-doped 4×3 SnS_2 monolayer by Li *et al.* [22]. However, in a big supercell there is a doping region and a region with less average strain felt by the atomic bonds, at distances further away from the dopant [23, 24]. Freysoldt *et al.* [20] revealed that defects in bigger surface areas are more isolated and therefore, one will able to observe their real effects on the structure. Hence, the 5×5 supercell was chosen for its bigger surface area and its computational time efficiency.

The formation energies of our identified doping configurations take the following order of stability, as shown in figure 4.7 for 5x5 supercell: $C_{Ads-Sn} < C_{Sub-S} < C_{Int} < C_{Ads-S} < C_{Sub-Sn}$. C_{Sub-Sn} has the highest formation energy, thus the least experimentally feasible doping configuration. The relaxed structure of C_{Sub-Sn} is presented in figure 4.8 (e). In the C_{Sub-Sn} configuration, the C dopant migrated to the lower S atoms layer and formed a planar bond with three adjacent S atoms. Thus, C_{Sub-Sn} is highly unstable. Configuration C_{Ads-S} has the second highest formation energy, therefore, more stable than C_{Sub-Sn} but less stable than other configurations. The relaxed structure of C_{Ads-S} is presented in figure 4.8 (b). The C_{Ads-S} configuration shows instability as the sulphur and carbon molecule broke off from the middle Sn atoms layer to h_{Carbon} of 3.94 Å.

For C_{Int} configuration, the C atom formed a planar bond with the three adjacent S atoms and also stayed in the same line as the S atoms as shown in figure 4.8 (a). This configuration has a formation energy of 6.46 eV and it was considered to be synthesizable

by Shown *et al.* [25]. Configuration C_{Sub-S} has a formation energy of 5.90 eV which is closer to that of C_{Int}. The relaxed structure of C_{Sub-S} is presented in figure 4.8 (d). For the C_{Sub-S} configuration, the C atom bonded to the adjacent Sn atoms. It further relaxes downwards to the Sn atoms layer leading to the height (h_{Carbon}) of 0.56 Å. C_{Ads-Sn} has the least formation energy of $5.07eV$, as shown in figure 4.7. This shows that adsorbing on Sn is the most convenient doping location for C as it relaxes the structure. In the C_{Ads-Sn} configuration, the C formed bonds with the three adjacent S atoms as well as the Sn atom which it was adsorbed on top of making a height (h_{Carbon}) of 0.83 Å. The C dopant pushed the Sn atom towards the lower S atoms layer.

The bond lengths of these configurations were measured and shown in table 4.2. C_{Sub-S} is the closest to the Sn atoms, however C adsorbed on S had the shortest bonding length due to both their high electronegativity values which cause the individual atoms to have a strong pull on the electrons which they share. The orientation of these relaxed doping

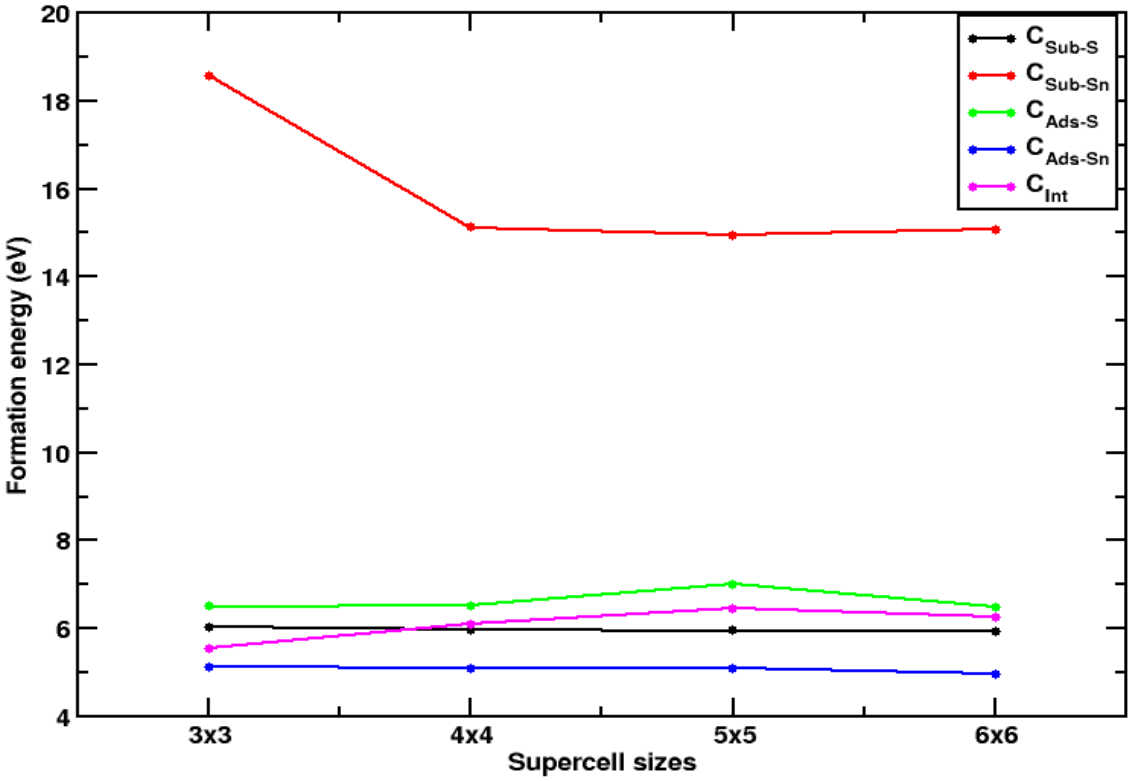

Figure 4.7: Graph of formation energy values for the different carbon atom doped configurations and different supercell sizes.

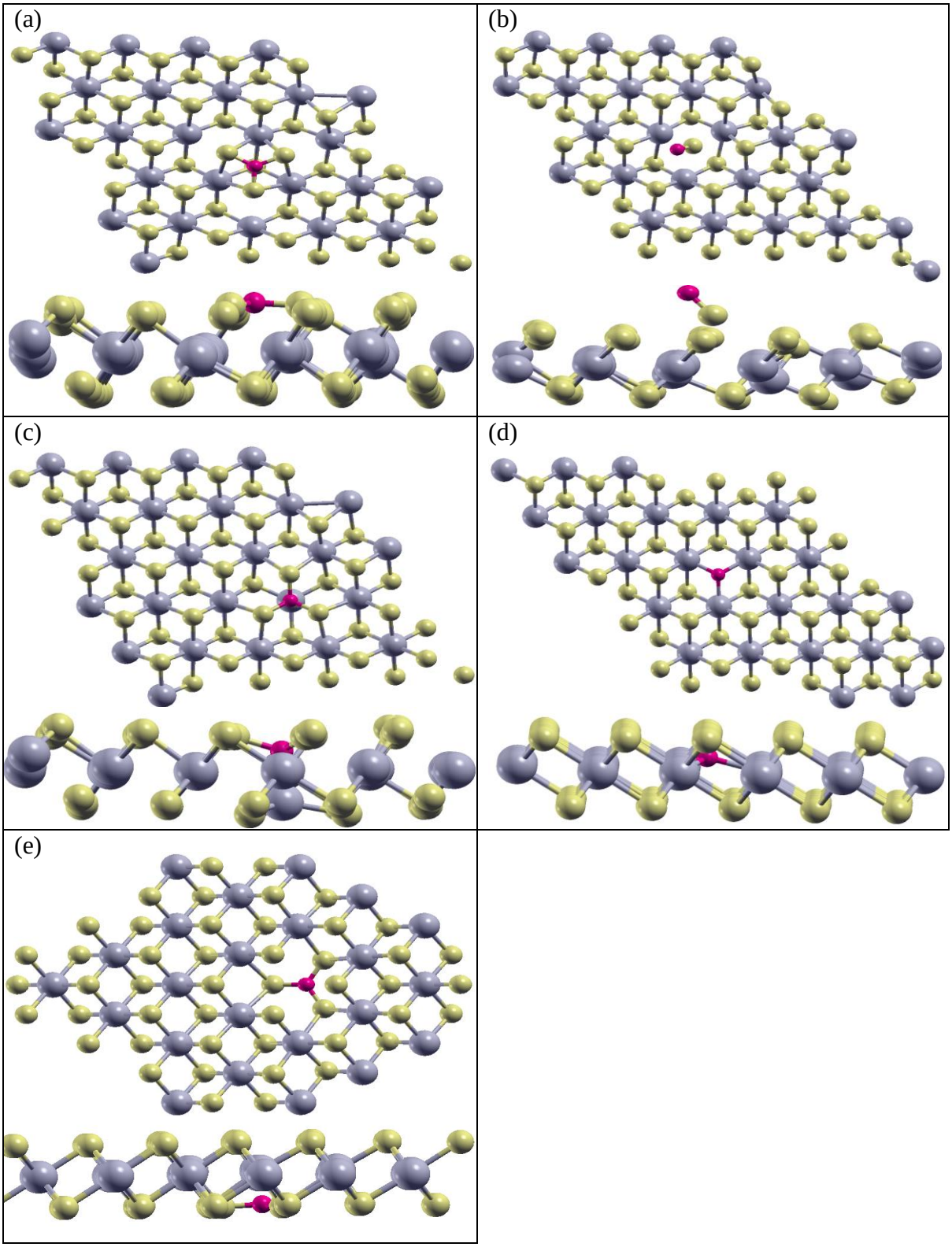

Figure 4.8: The different relaxed C doped configurations: (a) C_{Int}, (b) C_{Ads-S}, (c) C_{Ads-Sn}, (d) C_{Sub-S} and (e) C_{Sub-Sn} on a 5 × 5 SnS_2 supercell.

configurations could be explained further from the study of their charge density differences. All bond lengths are shorter than that of the pristine of 2.58 Å due to the smaller atomic radius of C, and the higher electronegativity of C causes a stronger Coulomb interaction between C and the supercell atoms. Understandably, the C_{Sub-S} configuration has the bond length closest to that of the pristine since the dopant is placed in the S position, however, due to relaxation, the bond length reduces.

Table 4.2: Bond lengths of the relaxed doped configurations. For the bond lengths d_{C-X}, C is the dopant and X = Sn or S depending on the doped configuration. h_{Carbon} is the height of the C dopant from the Sn atoms layer. Negative (-) indicates below and positive (+) indicates above the Sn layer according to the configurations presented in figure 4.8.

Configurations	$\boldsymbol{d_{C-X}}$ (Å)	$\boldsymbol{h_{Carbon}}$ (Å)
C_{Int} X=S	1.73	2.00
C_{Ads-S} X=S	1.56	3.94
C_{Ads-Sn} X=S	1.83	0.83
C_{Sub-S} X=Sn	2.23	0.56
C_{Sub-Sn} X=S	1.73	-1.56

4.3.2 Total and partial density of states for carbon doped SnS_2 monolayer

DFT simulation for the DOS were performed for these different doping configurations and presented in figures 4.9 – 4.13. These simulations are beneficial for understanding the effects of C doping on the electronic structure of the SnS_2 material. Fermi level shifts observed in the DOS are also reported. Conclusions on these Fermi level shifts are based

on the work of Almadori *et al.* [26], who reported that hole doping (p-type) causes downshift for the Fermi level and electron doping (n-type) causes an upshift of the Fermi level.

The reference TDOS and PDOS, which are the TDOS and PDOS for pristine SnS_2, are presented in figure 4.5. In particular, figure 4.5 (b) with Hubbard U value of 8 eV, which all further calculation were based on. The Fermi level was moved to the 0 point on the x-axis for all doped configurations. Figure 4.9 (a), (b) and (c) show the TDOS and PDOS for C_{Int} configuration. The Fermi level moved upwards towards the CBM, thus, modifying the material to be strongly n-type [26, 27]. As a result of the upwards shift of the Fermi level, the VBM moved to lower energy levels of -1.17 eV, as compared to -0.57 eV for pristine. The VBM is still dominated by the S 3p orbitals, however the doped C 2s orbitals induced relatively long peak states as shown in figure 4.9 (c). The valence states are constantly composed of a hybridization of the C 2p, S 3p and Sn 5p orbitals as shown in figure 4.9 (b). As a result of upward shift of the Fermi level, the CBM moved to lower energy levels of 0.08 eV. The CBM is now mainly composed of a hybridization of the C 2p, S 3p and Sn 5s orbitals as seen in figure 4.9 (b) and (c). The conduction states are mainly dominated by a hybridization of the Sn 5s, C 2p and S 3p orbitals as shown in figure 4.9 (b) and (c). There exists intermediates states mainly contributed by C 2p orbitals at the vicinity of the Fermi level as shown in figure 4.9 (a) and (b).

Figure 4.10 (a), (b) and (c) show the TDOS and PDOS for C_{Ads-S} configuration. The Fermi level shifts towards the CBM making this structure an n-type material. The upwards shift of the Fermi level resulted in the downward shift of the VBM and CBM to energies of -1.11 eV and 0.29 eV, respectively. The VBM is mainly contributed by S 3p, C 2p and C2s orbitals as shown in figure 4.10 (b) and (c). The valence states are composed of a hybridization of the C 2p, S 3p, Sn 5p and C 2s orbitals as shown in figure 4.10 (b) and (c). The C 2p orbitals caused an extension of the CBM with a long peak hybridized with minority S 3p and Sn 5s orbitals as shown in figure 4.10 (b) and (c). The conduction states are composed by hybridization of C 2p, S 3p and Sn 5s orbitals as shown in figure 4.10 (b) and (c). Two peaks appear in between the band gap which are mainly composed of C 2p orbitals hybridized with a minority S 3p and Sn 5s orbitals as shown in figure 4.10 (b) and

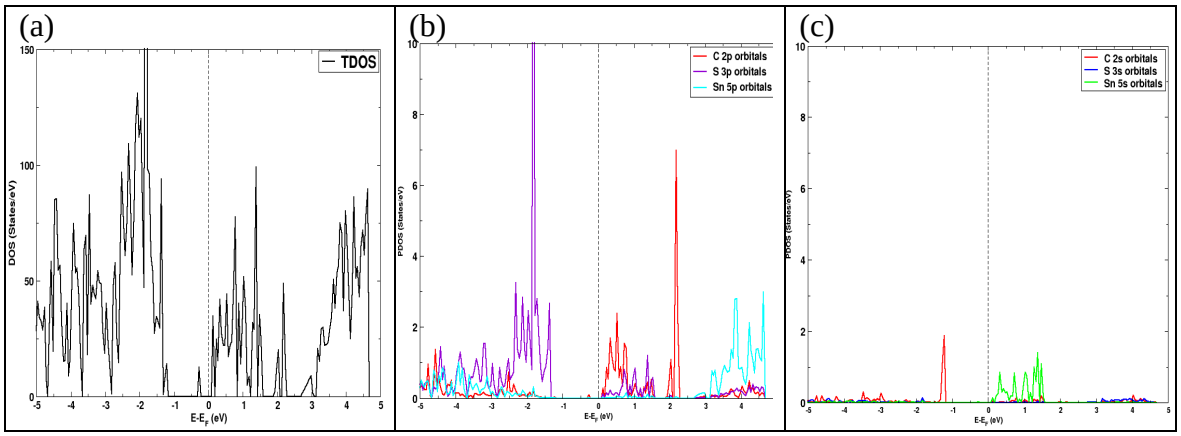

Figure 4.9: C_{Int} (a) TDOS, (b) PDOS for p orbitals and (c) PDOS for s orbitals.

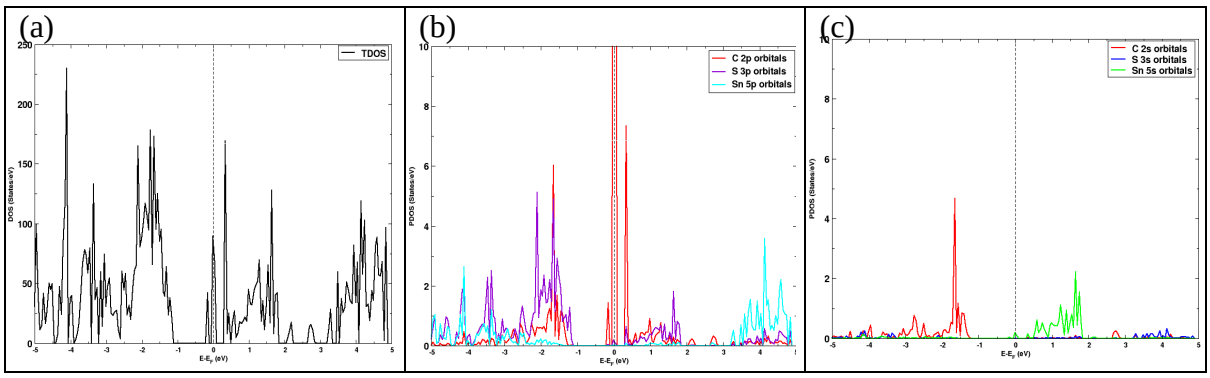

Figure 4.10: C_{Ads-S} (a) TDOS, (b) PDOS for p orbitals and (c) PDOS for s orbitals.

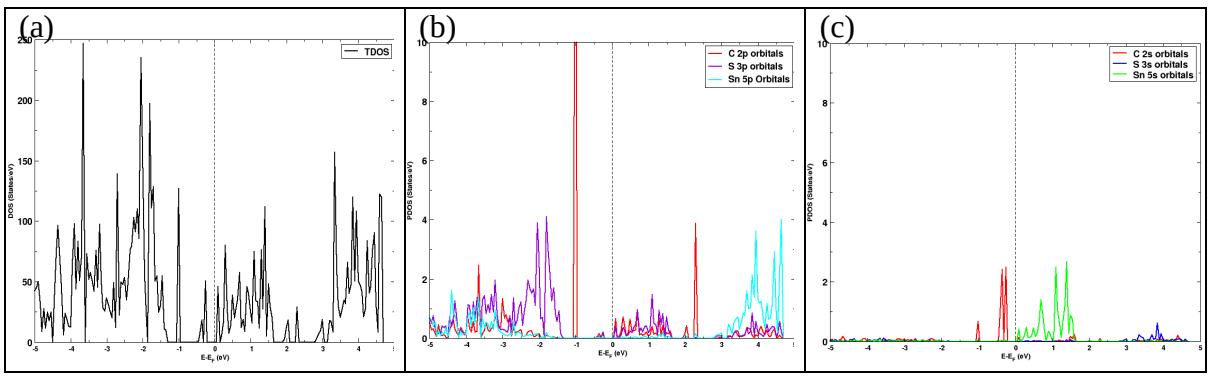

Figure 4.11: C_{Ads-Sn} (a) TDOS, (b) PDOS for p orbitals and (c) PDOS for s orbitals.

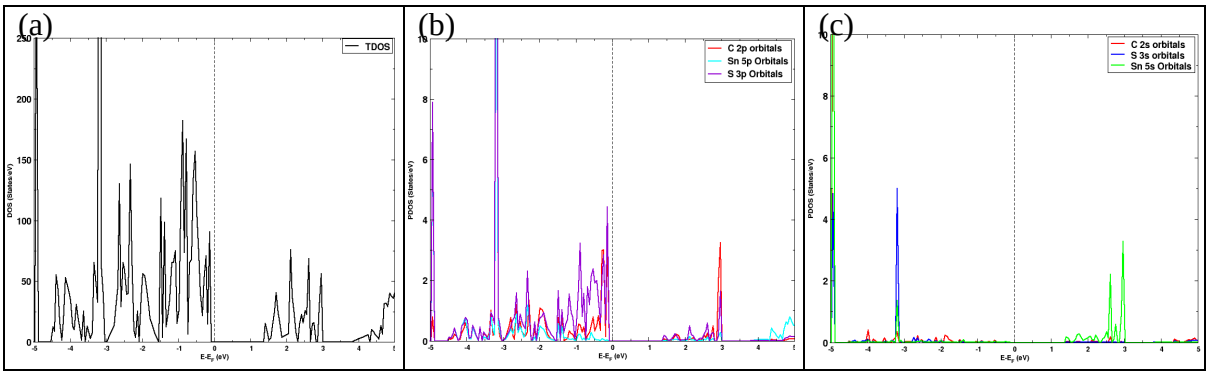

Figure 4.12: C_{Sub-S} (a) TDOS, (b) PDOS for p orbitals and (c) PDOS for s orbitals.

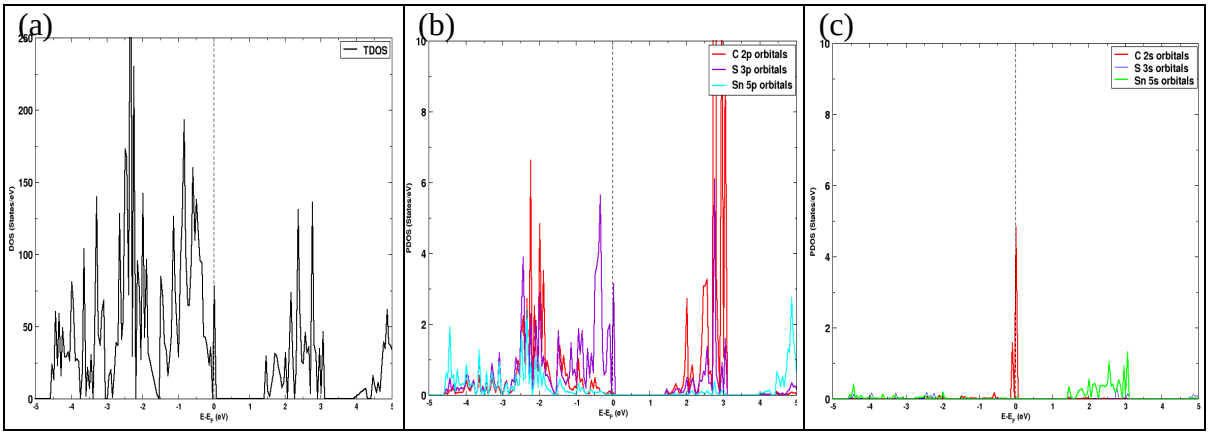

Figure 4.13: C_{Sub-Sn} (a) TDOS, (b) PDOS for p orbitals and (c) PDOS for s orbitals.

(c). Figure 4.11 (a), (b) and (c) show the TDOS and PDOS for C_{Ads-Sn} configuration. The Fermi level of the C_{Ads-Sn} configuration moved closer to the CBM making the material an n-type. The upward shift of Fermi level reduced VBM to -1.30 eV. Much like pristine, the VBM is mainly contributed by S 3p orbitals, as shown in figure 4.11 (b), and the valence states are due to the hybridization of S 3p, Sn 5p and C 2p orbitals as shown in figure 4.11 (b). CBM is located at 0.05 eV as a result of Fermi level shifts and is contributed by a hybridization of Sn 5s, S 3p and C 2p orbitals as shown in figure 4.11 (b) and (c). This hybridization also forms the entire conduction band. Three intermediate band peaks appear at -1 eV, -0.4 eV and -0.3 eV. The peak at -1 eV mainly consists of C 2p orbitals and a minority C 2s orbitals. The peaks at -0.4 eV and -0.3 eV are mainly contributed by C 2s orbitals and a minority S 3p and C 2p orbitals, these are shown in figure 4.11 (b) and (c).

Figure 4.12 (a), (b) and (c) show the TDOS and PDOS for C_{Sub-S} configuration. Different scenario is noted with the DOS of C_{Sub-S} configuration. The Fermi level shifted downwards towards the VBM making a p-type material [26, 27]. In this case the VBM is contributed by a hybridization of S 3p and C 2p orbitals as shown in figure 4.12 (b). The valence states are constantly contributed by a hybridization of S 3p, Sn 5p and C 2p orbitals, shown in figure 4.12 (b). The CBM is at a higher energy value of 1.37 eV, as compared to the CBM of the adsorption configurations. The CBM is contributed by a hybridization of S 3p, C 2p and Sn 5s orbitals where the conduction states are composed of a hybridization of Sn 5s, S 3p, Sn 5p and C 2p orbitals as shown in figure 4.12 (b) and (c). There are no intermediate states within the band gap of the C_{Sub-S} configuration, shown in figure 4.12 (a).

Figure 4.13 (a), (b) and (c) show the TDOS and PDOS for C_{Sub-Sn} configuration. A unique case appears in the C_{Sub-Sn} configuration whereby the Fermi level is submerged into the VBM, making the material strongly p-type. The VBM appears at 0.07 eV and is composed of a hybridization of S 3p and C 2s orbitals as shown in figure 4.13 (b) and (c). The valence states are composed of a hybridization of C 2p, Sn 5p and S 3p orbitals as shown in figure 4.13 (b). The CBM appears at 1.42 eV and is composed of S 3p, C 2p and Sn 5s orbitals as shown in figure 4.13 (b) and (c). The conduction states are composed of mainly S 3p, C 2p, S 5s and a minority Sn 5p orbitals. Even with the C_{Sub-Sn} configuration there are no intermediate states within the band gap as shown in figure 4.13 (a).

The exact values of the band gaps for the doped configurations along with pristine SnS_2 band gap are shown in table 4.3. All the band gap values, including that of pristine, are within the range at which visible light excites electrons into the conduction band [28]. Compared to all the doped configurations, C_{Int} configuration has the least band gap of 1.25 eV and C_{Sub-S} has the highest band gap value of 1.45 eV. All band gaps of the doped configurations are lower than that of the pristine monolayer, thus it can be concluded that C doping reduces the band gap of SnS_2.

Table 4.3: The different band gap values of carbon doped configurations compared with that of the pristine SnS_2 monolayer.

Configurations	E_g (eV)
SnS_2	2.34
C_{Int}	1.25
C_{Ads-S}	1.40
C_{Ads-Sn}	1.35
C_{Sub-S}	1.43
C_{Sub-Sn}	1.35

4.3.3 Charge density difference of carbon doped configurations

To further understand the charge dynamics between the C dopant and SnS_2 material's atoms, the charge density differences for different configurations were plotted and shown in figure 4.14 (a)-(e). These charge differences were plotted using the following equation (4.7) [29, 30]:

$$\Delta\rho = \rho^{total} - \sum_i \rho^{fragments}, \tag{4.7}$$

where ρ^{total} and $\rho^{fragments}$ represent total and individual charge density, respectively. This charge density difference could be an advantageous reaction centre for charge carriers such as the hydroxyl ion (OH^-) and hydrogen ion (H^+) for water splitting application as reported for hematite surface doping by Chang *et al.* [31] and Simfukwe *et al.* [32].

For all doped systems, the magenta sphere denotes the C atom, the purple spheres denote Sn atoms and the yellow spheres denote the S atoms. The orange shows a depletion of charge (positive) region and the blue shows an accumulation of charge (negative) region for all configurations. These charge shifts are attributed to the difference in electronegativity values of the interest atoms following this order S > C > Sn (the exact

values being: 3.44 > 3.15 > 2.68, respectively) [33]. Electronegativity measures the tendency of an atom to attract or hold on to electrons. Electronegativity increases as you move up and to the right of the periodic table.

The top and side views of these charge density differences of (a) C_{Int}, (b) C_{Ads-S}, (c) C_{Ads-Sn}, (d) C_{Sub-S} and (e) C_{Sub-Sn} are shown in figure 4.14 below. In figure 4.14 (a) C_{Int} configuration, as expected, the S atoms are surrounded by the blue cloud (negative charge) and the C atom is surrounded by the orange cloud (positive charge). This indicates that due to the electronegativity difference, the C atom was unable to retain its electrons, thus becomes a positive centre which would be an oxidation point.

Figure 4.14 (b), shows the charge density differences for C_{Ads-S} configuration. It is noticed from the side view that C atom has an orange cloud (positive charge) above it, and also surrounded by a blue sphere (negative charge). Another orange cloud is noted between the C and S atoms. This is due to C being more electronegative than Sn, but less electronegative than S. Therefore, both the C and S pulled electrons from their nearest neighbour Sn atoms. This accumulation of charge by C and S atoms and the electron deficiency at the adjacent Sn atoms lead to failure in C-S bond formation as is evident in figure 4.8 (b).

Figure 4.14 (c), present the charge density difference for C_{Ads-Sn} configuration. The blue clouds (accumulated charge) at the S atoms adjacent to the C atom are noted and the orange cloud (electron deficiency region) above and below the C atom is also noted. This is an indication that the S atoms have pulled electrons away from the C dopant as expected. However, it is also noted from the top and side views that there are small blue clouds surrounding the C atom. This is due to the C atom pulling some electrons from the Sn atom, since C is more electronegative than Sn. Figure 4.14 (d) presents charge density difference for C_{Sub-S} configuration. The blue cloud accumulates above and below the C atom and the orange clouds are in between C atom and Sn atoms. The C atom was only bonded to the low electronegative adjacent Sn atoms, thus, was able to draw electrons from them. Figure 4.14 (e) presents the charge density differences for C_{Sub-Sn} configuration. C atom is surrounded by the orange clouds indicating that it has lost the charge. Also noticed in between the C and S bonds are blue clouds showing that the charge has been shifted

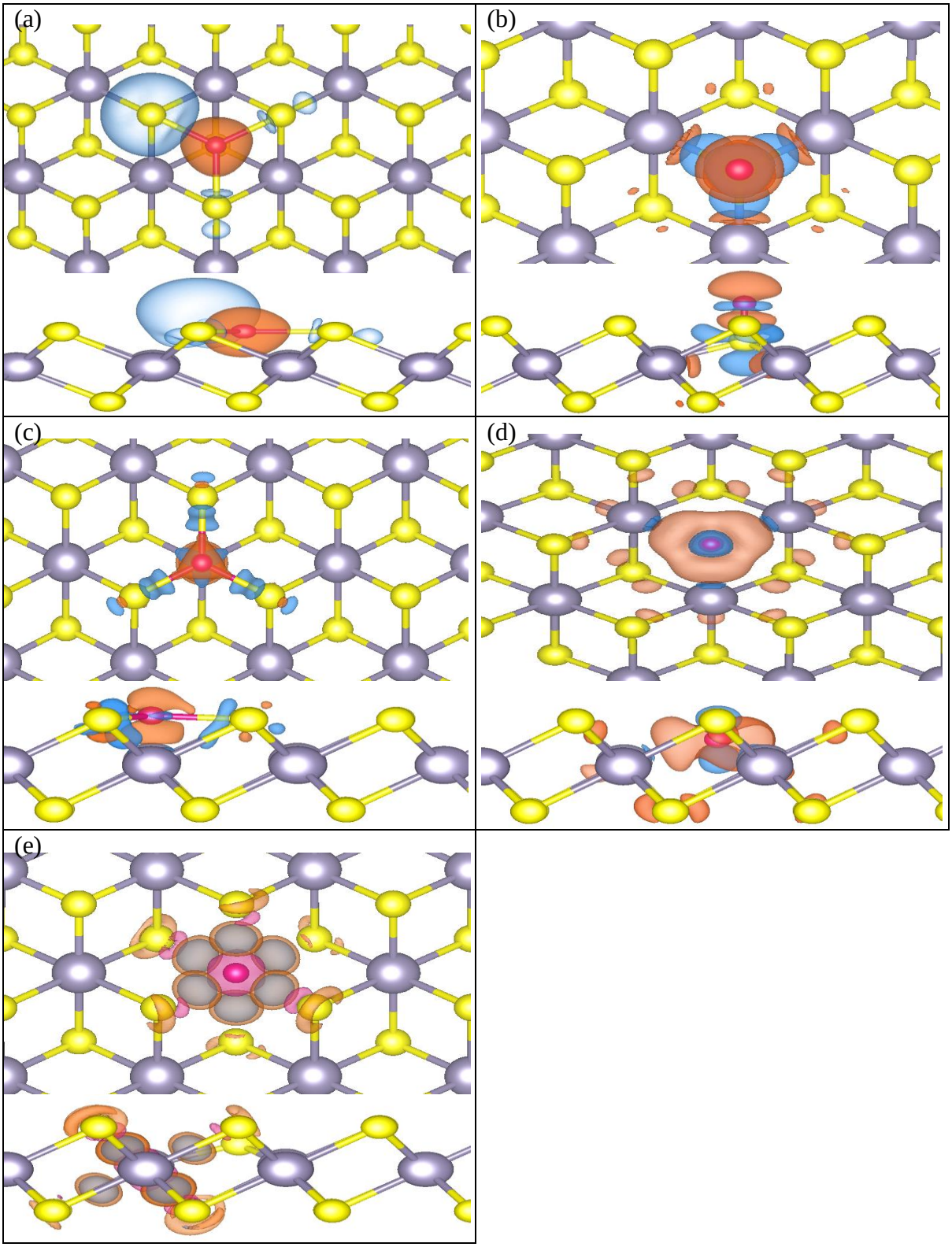

Figure 4.14: Charge density difference diagrams for: (a) C_{Int}, (b) C_{Ads-S}, (c) C_{Ads-Sn}, (d) C_{Sub-S} and (e) C_{Sub-Sn}.

from C atom to S atoms due to the high electronegativity of S.

Thus, adsorbed carbon doping (C_{Int}, C_{Ads-S} and C_{Ads-Sn}) modify the material into an n-type material which is good for electron donating. Substitutional carbon doping (C_{Sub-S} and C_{Sub-Sn}) modify the material into a p-type material, thus good for electron receiving. As photo-excitons (electrons + holes) move about the material, the carbon doped region in the material will become the concentration centre of the holes which would make a good oxidation reaction zone for OH^-. The sulphurs adjacent to the dopant will be the concentration centres of negative charges, thus good reduction reaction zones for H^+. It is only C_{Sub-Sn} configuration which seems to have a net neutral charge at the doping region.

4.3.4 Band edge alignment of pristine and carbon doped configurations

As mentioned in chapter 1, band edge alignment compares the VBM and CBM to the water redox potentials. The CBM should be above the water reduction potential (H^+/H_2), the VBM should be below the water oxidation potential (O_2/H_2O) and a non-zero E_g should be measurable for photoactivation ($E_g < 3.1\ eV$) [28] for PEC WS to advance. Figure 4.15 shows the band alignment of pristine SnS_2 compared to the carbon doped configurations. Labels specified above the bars are the pristine and doped configurations, and the values below the bars are their corresponding band gaps. The values inside the bar charts are the differences of the band edges (CBMs and VBMs) of the doped configurations and the pristine SnS_2. The negative values show a downward shift while the positive values show an upward shift from the band edges of pristine SnS_2. The orange bars are conduction bands and the green bars are valence bands. The blue dashed line across the graph is the reduction potential and the red dashed line is the oxidation potential.

All the band gap values are suitable for light activation of electrons as illustrated in figure 4.15. The VBM position for pristine SnS_2 ($E_g = 2.34\ eV$) is suitable for ultra-spontaneous oxygen evolution, however position of CBM inhibits water reduction as it is below H^+/H_2. Lindquist *et al.* [34] reported that when the CBM of the photoelectrode is below the water reduction potential, the electrons from an external circuit are able to provide the required voltage for PEC WS to proceed. The external circuit introduces electrons to the

photoelectrode which enable band maxima shifts. Therefore, the use of an external bias voltage enables lifting the bands to higher energies. Thus, application of an external bias to pristine SnS_2 photoelectrode could be a technique used to increase its CBM, by a reasonably low value of 0.14 eV, to be above H^+/H_2 as shown in figure 4.11. The VBM would also increase, but would still be at an energy below O_2/H_2O, thus enabling pristine SnS_2 to be an ideal photocatalyst for hydrogen production and for overall water splitting.

Doped configuration C_{Int} has a band gap of 1.25 eV, which is ideal for photoactivation with visible light, and a VBM that is 0.60 eV below the VBM of pristine. The CBM of C_{Int} configuration is far below the H^+/H_2 potential. Hence, this doping configuration is not suitable for hydrogen evolution, but would be suitable for oxygen evolution. This has similar behaviour with C_{Ads-S} and C_{Ads-Sn}, but differing in shifts magnitude. C_{Ads-S} configuration has an E_g of 1.40 eV, the VBM is 0.54 eV below the reference and the CBM is 1.29 eV below the reference. C_{Ads-Sn} configuration has an E_g of 1.35 eV, the VBM is 0.73 eV below the reference and the CBM is 1.53 eV below the reference. These doped configurations are only suitable for oxygen evolution.

Doped configuration C_{Sub-S} has an E_g of 1.45 eV, thus requiring less photoactivation energy than pristine SnS_2. C_{Sub-S} has a VBM that is 0.49 eV above the reference, which is still below O_2/H_2O and suitable for oxygen evolution, as shown in figure 4.15. Its CBM is 0.21 eV below the reference, thus still unsuitable for hydrogen evolution. Therefore, an external bias could be applied to raise the CBM by at least 0.35 eV to energy levels above H^+/H_2, thus, making it suitable for water reduction. Thus, the external bias could enable C_{Sub-S} to be the most suitable for overall water splitting to produce both hydrogen and oxygen.

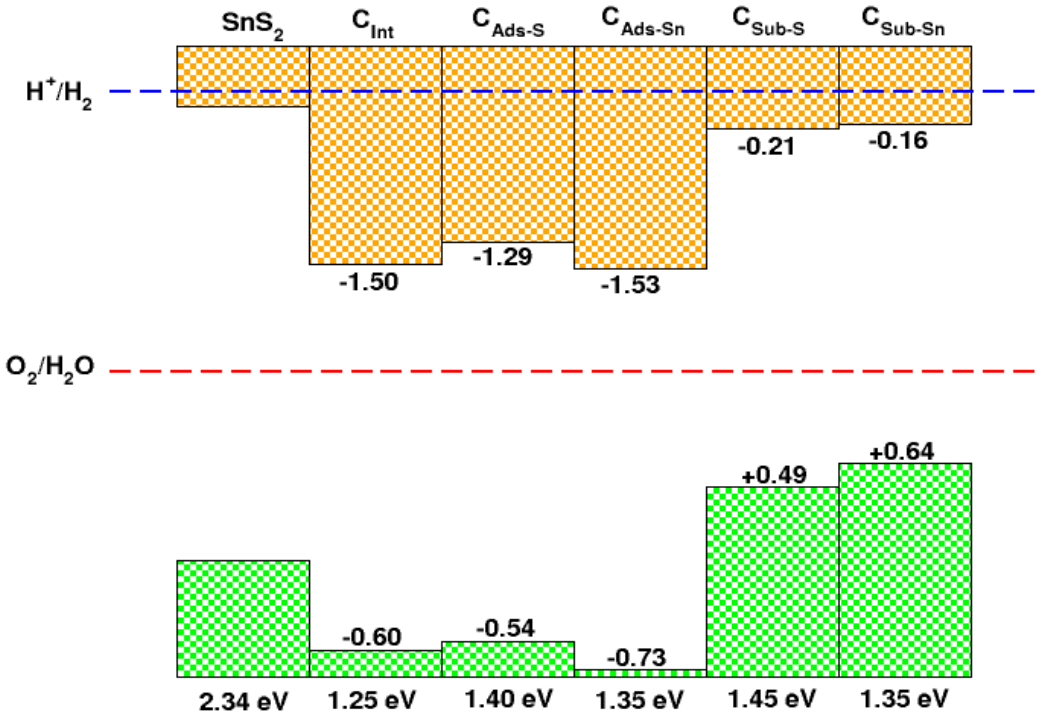

Figure 4.15: Band edge alignment for pristine SnS_2 and carbon doped configurations: C_{Int}, C_{Ads-S}, C_{Ads-Sn}, C_{Sub-S} and C_{Sub-Sn}.

Doped configuration C_{Sub-Sn} has an E_g of 1.35 eV, also requiring less photoactivation energy than pristine SnS_2. The VBM of C_{Sub-Sn} is 0.64 eV above the reference, which is still below O_2/H_2O thus making it suitable for oxygen evolution. Its CBM is 0.16 eV below the reference, thus below H^+/H_2 making it unsuitable for water reduction. The external bias could help in making it suitable for overall water splitting, however C_{Sub-Sn} has the highest formation energy (figure 4.7).

4.4 Silicon doping on SnS_2 monolayer

In this section, the effects of doping with silicon, using the same doping techniques as carbon were investigated to improve efficiency of SnS_2 for photocatalytic water splitting. Silicon is in the same group as carbon, in fact directly below it on the periodic table, thus

has a larger atomic number and radius. Silicon is sp^3 hybridized [35] as opposed to carbon which has sp^3, sp^2 and sp^1 hybridizations [36]. It is expected that silicon and carbon will behave similarly, however their difference in hybridizations could make their electronic behaviours different.

A comparative investigation as C doped configurations was performed for Si doped on SnS_2 monolayer. Thermodynamic stability was calculated for all these configurations in order to determine whether they are experimentally synthesizable. The Si atom is doped at similar positions as C doped configurations and corresponding notations were given to the Si doped configurations, shown in figure 4.16 (a)-(e). Figure 4.16 (a) is a configuration of Si adsorbed at an interstitial position (Si_{Int}). In the Si_{Int} configuration, the Si is placed at the centre of hexagon, directly above the bottom sulphur and at the same height as the top sulphurs. Figure 4.16 (b) is a configuration of Si adsorbed on a S atom (Si_{Ads-S}). Figure 4.16 (c) is a configuration of Si adsorbed on a Sn atom (Si_{Ads-Sn}), at the same height as the S atoms. Figure 4.16 (d) is a Si substituting S configuration (Si_{Sub-S}). Lastly, figure 4.16 (e) is a Si substituting Sn configuration (Si_{Sub-Sn}).

4.4.1 Energetic stability and structural properties of silicon doped configurations

The different unrelaxed Si doped structures are shown in figure 4.16. A full geometry optimization (FGO) calculation (VC-relax criterion in PW-scf quantum espresso packages) was performed to obtain the equilibrium properties of the Si doped SnS_2 monolayer. Just like for carbon study, the single Si was doped on the supercell sizes 3×3, 4×4, 5×5 and 6×6. Again the formation energy was calculated using equation (4.8), however was modified to be suitable for Si doping:

$$E_f = E_{(doped\ SnS_2)} - \left(E_{SnS_2} - \delta_{\mu_X} - \mu_{Si}\right) - 1, \tag{4.8}$$

where E_{SnS_2} and $E_{(doped\ SnS_2)}$ denote the pristine and doped supercell energies, respectively. μ_{Si} and μ_X ($X = Sn$ or S) denote silicon's and the substituted atom's chemical potential, respectively. The chemical potential for Si (μ_{Si}) was calculated from energy of

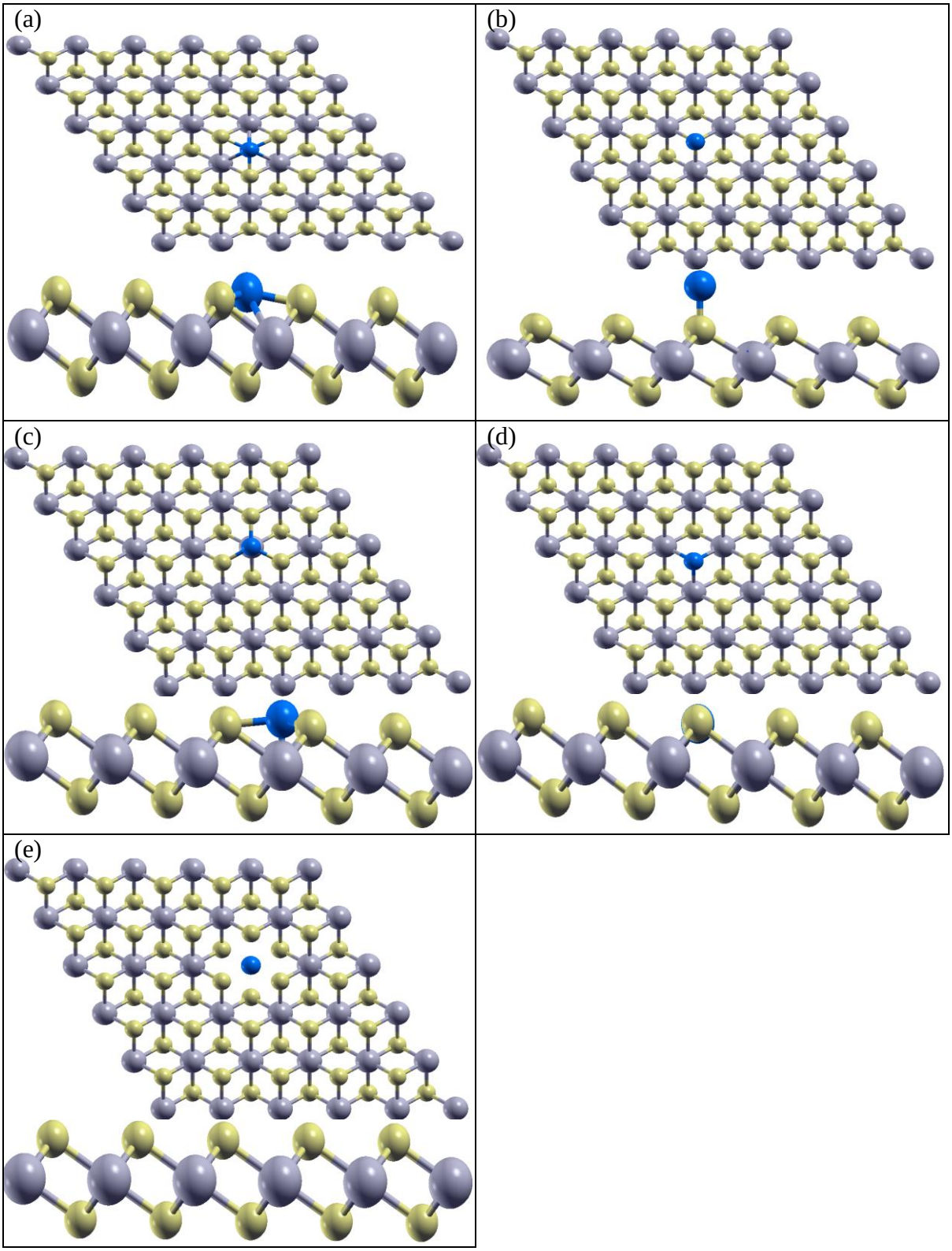

Figure 4.16: The description of the unrelaxed different Si doped configurations: (a) Si_{Int}, (b) Si_{Ads-S}, (c) Si_{Ads-Sn}, (d) Si_{Sub-S} and (e) Si_{Sub-Sn}. The Si atom is represented by the blue sphere, S atoms by the yellow spheres and Sn atoms by the purple spheres.

silicene. μ_X was calculated from the energy of a diatomic molecule in a large box ($10 \times 10 \times 10$). For the different types of doping configurations, equation (4.8) takes the same form as equations (4.4) – (4.6), except that the chemical potential for C (μ_C) is changed to the chemical potential for Si (μ_{Si}). For the adsorption doping cases (Si_{Int}, Si_{Ads-S} and Si_{Ads-Sn}), the term μ_X was omitted from the formation energy equation, therefore $\delta = 0$, while for substitutional doping $\delta = 1$.

Figure 4.17 presents the formation energies for the different supercell sizes and doping configurations. The formation energies are positive (endothermic), suggesting that an external energy should be supplied for formation to occur. Subsequently, the formation energies of these configurations differ in magnitude which indicates that the formation of Si doping in a SnS_2 monolayer greatly depend on the configuration.

For supercell convergence tests, except for Si_{Sub-Sn}, the formation energies of all other identified doping configurations have converged with a maximum difference of about

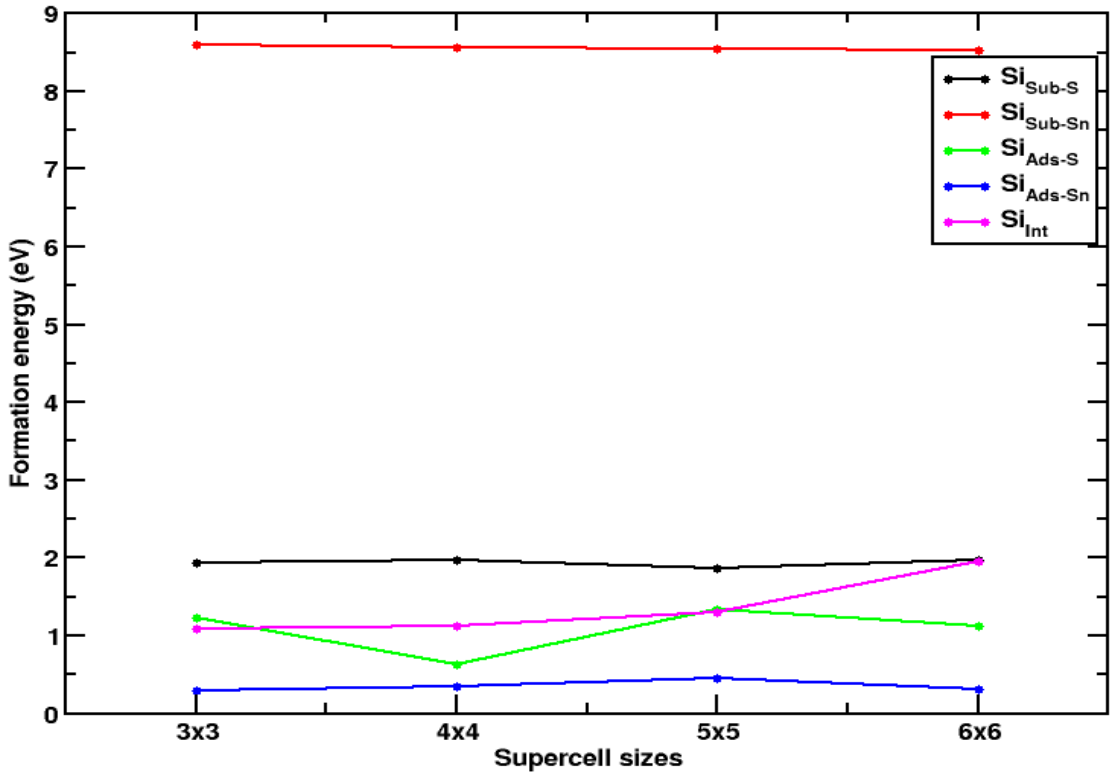

Figure 4.17: Graph of formation energy values for the different silicon atom doped configurations on different supercell sizes.

0.87 eV from 3×3 supercell onwards. As was noticed in the C doping study, Si_{Sub-Sn} also has the highest formation energy and Si_{Ads-Sn} also has the least formation energy. On average, Si doped configurations have lower formation energies than C doped configurations. Thus, Si doped SnS_2 is more experimentally feasible than C doped SnS_2.

In an effort to avoid the influence of atomic strain resulting from a small supercell, as explained in the C doping study, the 5×5 supercell was chosen again. Choosing the 5×5 supercell also allows consistency for efficient comparison with the C doped study. The formation energies of our identified doped configurations take the following order of stability, as shown in figure 4.17 for 5×5 supercell: $Si_{Ads-Sn} < Si_{Int} < Si_{Ads-S} < Si_{Sub-S} < Si_{Sub-Sn}$. The 5×5 relaxed doped configurations are shown in figure 4.18 (a)-(e).

For the Si_{Int} configuration in figure 4.18 (a), the Si atom formed bonds with the adjacent S atoms. Also due to its sp^3 hybridization nature and its relatively big atomic radius, it also formed bonds with the adjacent Sn atoms. This configuration has a formation energy of 1.30 eV. Configuration Si_{Ads-S} is presented in figure 4.18 (b) and has a formation energy of 1.37 eV. In this configuration, the Si atom relaxed into an interstitial position and bonded to three adjacent S atoms. The Si_{Ads-Sn} configuration, shown in figure 4.18 (c), had the least formation energy of $0.44\ eV$, therefore highest stability. Thus, adsorbing Si on Sn requires small enthalpy of formation, promising to form spontaneously. The Si dopant formed bonds with the adjacent S atoms and the Sn atom which it was adsorbed on, as shown in figure 4.18 (c). The Si dopant further relaxes towards the Sn atoms layer leading to the height ($h_{Silicon}$) of 1.15Å. The Si dopant pushed the Sn atom towards the lower S atoms layer.

Configuration Si_{Sub-S} in figure 4.18 (d) has a formation energy of 1.84 eV. Si_{Sub-S} has a bond length ($d_{Si-Sn} = 2.23$Å) smaller than that of pristine SnS_2 monolayer ($d_{S-Sn} = 2.58$Å). This causes the Si atom to sink below the upper S atoms layer as presented in figure 4.18 (d). The shorter bond length of configuration Si_{Sub-S} could also be attributed to silicon's sp^3 hybridization. Brown *et al.* [37], reported that a greater s-character causes electrons to be held closer to the nucleus, thus the shorter and stronger the bond. Bu *et al.* [38] also reported a shorter bond length between sp^3-sp^3 bonds.

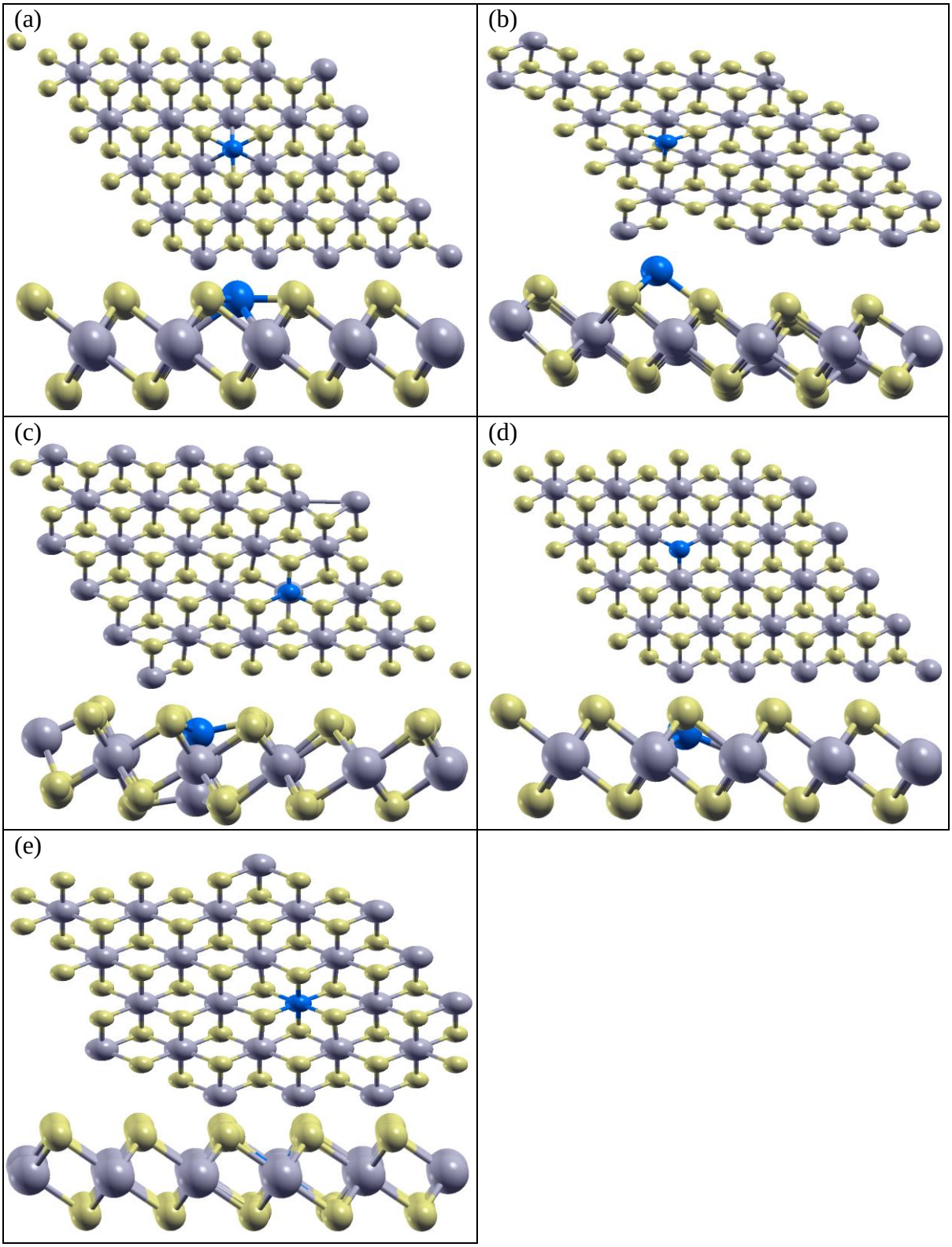

Figure 4.18: The different relaxed silicon doped configurations: (a) Si_{Int}, (b) Si_{Ads-S}, (c) Si_{Ads-Sn}, (d) Si_{Sub-S} and (e) Si_{Sub-Sn} on a 5 × 5 SnS_2 supercell.

Table 4.4: Bond lengths of the relaxed doped configurations. For the bond lengths d_{Si-X}, Si is the dopant and X = Sn or S depending on the doped configuration. $h_{Silicon}$ is the height of the Si dopant from the Sn atoms layer. Again, negative (-) indicates relaxation below and positive (+) indicates above the Sn layer according to the configurations presented in figure 4.18.

Configurations	$\boldsymbol{d_{Si-X}}$ (Å)	$\boldsymbol{h_{Silicon}}$ (Å)
Si_{Int} X=S	2.09	1.53
Si_{Ads-S} X=S	2.35	2.74
Si_{Ads-Sn} X=S	2.13	1.15
Si_{Sub-S} X=Sn	2.23	0.91
Si_{Sub-Sn} X=S	2.36	0.01

Finally, Si_{Sub-Sn} has the largest formation energy ($E_f = 8.54eV$) of all Si doped configurations. Therefore, Si_{Sub-Sn} is the least stable configuration of all the Si doped configurations. The Si remained in the Sn middle layer and bonded to all six adjacent S atoms as Sn would be. The bond lengths (d_{Si-X}) and height of the silicon dopant from the Sn atoms layer ($h_{Silicon}$) for these configurations are shown in table 4.4.

Unlike the C doping case, the silicon atom of the Si_{Ads-S} configuration moved closer to the middle Sn atom layer. Si also remained in the same position as the substituted Sn atom for Si_{Sub-Sn} whereas C formed a planar bond with 3 bottom S atoms for C_{Sub-Sn}. Si_{Int} had the shortest bonding length which could be attributed to Silicon forming bonds with adjacent S and Sn atoms which bring it much closer to the supercell, as can be noticed from the top view of figure 4.18 (a). All bond lengths for doped configurations are shorter than that of the pristine (2.58 Å) due to silicon's hybridization and carbon's smaller atomic

radius. The Si atom and the C atom both have the same number of valence electrons, but C has a smaller atomic radius hence C doping has, on average, smaller bond lengths. Silicon's sp^3 hybridization gives it a tendency of being close to the supercell, hence $average\ |h_{Silicon}| < average\ |h_{Carbon}|$.

4.4.2 Total and partial density of states for silicon doped SnS_2 monolayer

TDOS and PDOS simulations, for studying the effects of Si doping on the SnS_2 monolayer, were constructed and presented in figures 4.19 – 4.23. The reference DOS and PDOS are those for pristine SnS_2 with Hubbard U value of 8 eV in figure 4.5 (b). For all cases, the Fermi level was moved to the 0 point on the x-axis. Figure 4.19 (a), (b) and (c) show the TDOS and PDOS for the Si_{Int} configuration. The Fermi level moved a bit into CBM, as shown in figure 4.19 (a), thus, modifying the material to be strongly n-type. The VBM appears at energy levels of -1.33 eV, as compared to -0.57 eV for pristine. The VBM consists of only S 3p orbitals as shown in figure 4.19 (b). The valence states are constantly composed of a hybridization of the S 3p, Si 3p and Sn 5p orbitals as shown in figure 4.19 (b). As a result of upward shift of the Fermi level, the CBM moved to lower energy levels of 0.17 eV, as compared to 1.58 eV for pristine. The CBM is composed of a hybridization of the S 3p, Si 3p, Si 3s and Sn 5s orbitals. The conduction states are mainly dominated by a hybridization of the Sn 5s, Si 3s, Si 3p, S 3p and minority Sn 5s orbitals, as shown in figure 4.19 (b) and (c). There exists two intermediate states, of which those closest to the CBM are contributed by Si 3s and S 3p orbitals, and those closest to the VBM are caused by S 3p, Si 3p and a majority Si 3s orbitals.

Figure 4.20 (a), (b) and (c) show the TDOS and PDOS for Si_{Ads-S} configuration. The Fermi level shifts close to the CBM, thus material becomes a n-type structure. As a result of the upward shift of the Fermi level, the VBM and CBM appear at smaller energies of -1.23 eV and 0.22 eV, respectively. The VBM is mainly contributed by S 3p orbitals and the valence states are composed of a hybridization of S 3p, Si 3p, Sn 5p and Si 3s, as shown in figure 4.20 (b) and (c). The CBM is contributed by a hybridization of Si 3p, S 3p and Sn 5s orbitals and conduction states are composed by a hybridization of Sn 5s, Si 3p and S 3p states, as shown in figure 4.20 (b) and (c). Three IB peaks appear and are

described in their order from the CBM moving towards the VBM. The first peak, closest to the CBM, mainly consists of S 3p orbitals, the second peak is contributed by a hybridization of majority Si 3p, minority S 3p and minority Sn 5s orbitals. The third peak, closest to the VBM, mainly consists of Si 3p orbitals.

Figure 4.21 (a), (b) and (c) show TDOS and PDOS for the Si_{Ads-Sn} configuration. The Fermi level penetrates a little bit into the CBM making the material strongly n-type. The upward shift of the Fermi level reduced VBM and CBM to energy levels -1.41 eV and -0.02 eV, respectively. The VBM is mainly composed by S 3p orbitals and the valence states are contributed by a hybridization of S 3p, Sn 5p and Si 3p orbitals, as shown in figure 4.21 (b). CBM is contributed by a hybridization of Si 3p, Si 3s, Sn 5s and minority S 3p orbitals. This hybridization also forms the entire conduction band as shown in figure 4.21 (b) and (c). There exists intermediate states contributed by S 3p and Si 3s orbitals.

Figure 4.22 (a), (b) and (c) show the TDOS and PDOS for Si_{Sub-S} configuration. The Fermi level shifts towards the VBM, therefore making the material strongly p-type. Thus, shifts the VBM up to -0.38 eV, which is the biggest VBM value out of all Si doped configurations, even bigger than the VBM of pristine SnS_2 (-0.57 eV). The VBM is contributed by a hybridization of S 3p and Si 3p orbitals and the valence states are entirely contributed by a hybridization of S 3p, Si 3p, Si 3s and Sn 5p orbitals, as shown in figure 4.22 (b) and (c). The CBM is also at a higher energy value of 0.97 eV which is the highest of all Si doping configurations, but smaller than CBM of pristine SnS_2 (1.58 eV). The CBM is contributed by a hybridization of S 3p and Sn 5s orbitals and the conduction states are composed of a hybridization of S 3p, Sn 5p and Si 3p orbitals, as shown in figure 4.22 (b) and (c). There are no intermediate states for Si_{Sub-S} configuration, as illustrated in figure 4.22 (a).

Figure 4.23 (a), (b) and (c) shows the TDOS and PDOS for Si_{Sub-Sn} configuration. The Fermi level moves closer to the CBM, thus has a value of 0.41 eV, and modifies the material to be more n-type. This is contradictory to all other substitutional doping configurations. The CBM is composed of S 3p and Sn 5s orbitals and the conduction states

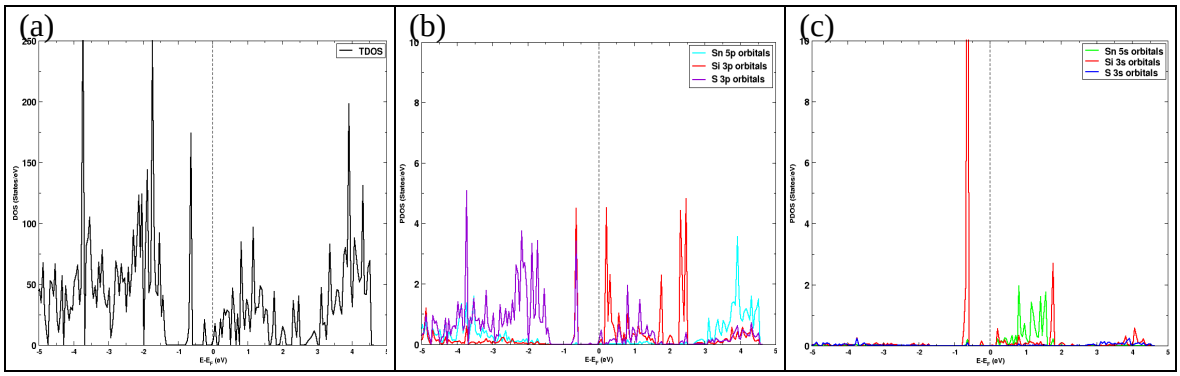

Figure 4.19: Si_{Int} (a) TDOS, (b) PDOS for p orbitals and (c) PDOS for s orbitals.

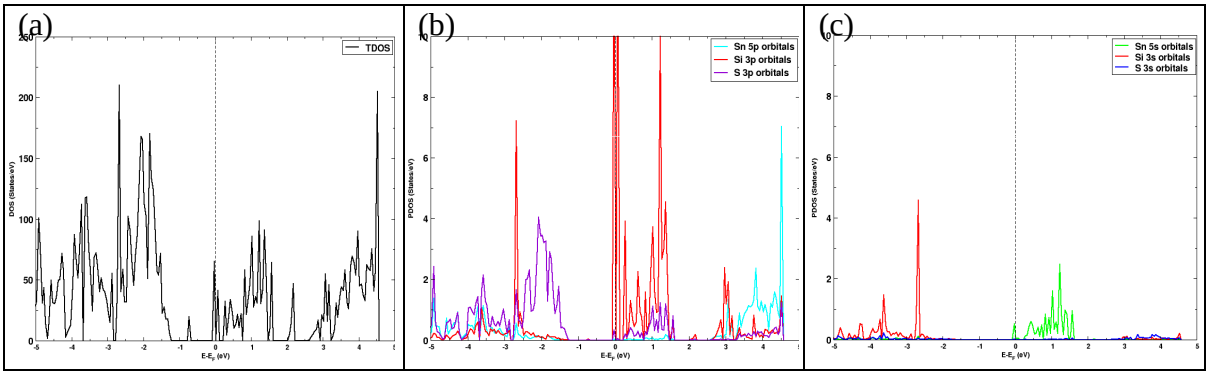

Figure 4.20: Si_{Ads-S} (a) TDOS, (b) PDOS for p orbitals and (c) PDOS for s orbitals.

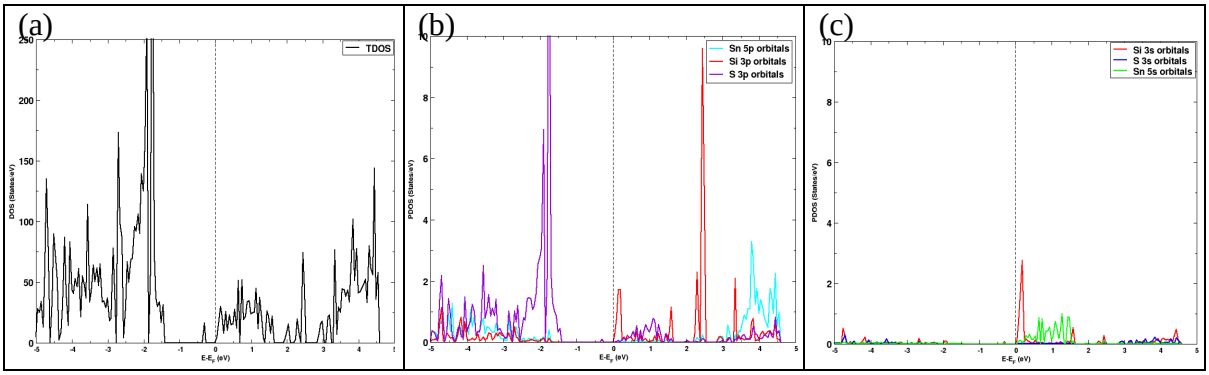

Figure 4.21: Si_{Ads-Sn} (a) TDOS, (b) PDOS for p orbitals and (c) PDOS for s orbitals.

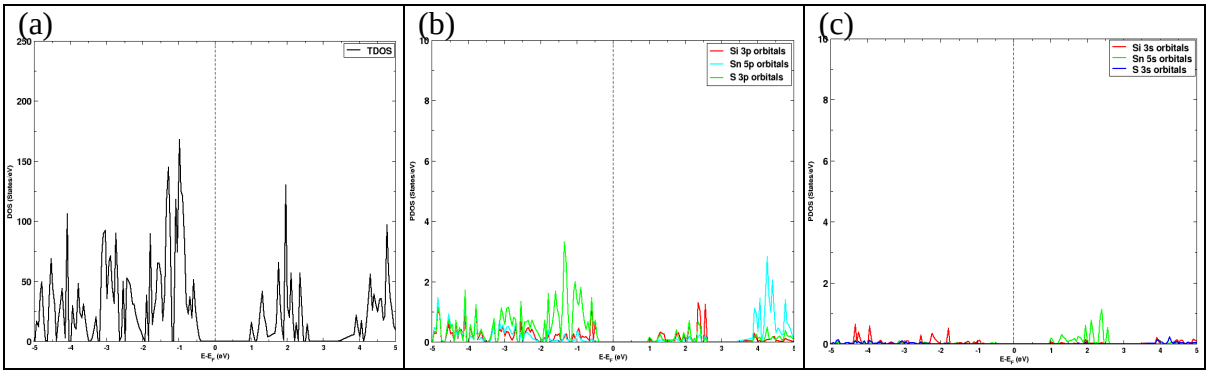

Figure 4.22: Si_{Sub-S} (a) TDOS, (b) PDOS for p orbitals and (c) PDOS for s orbitals.

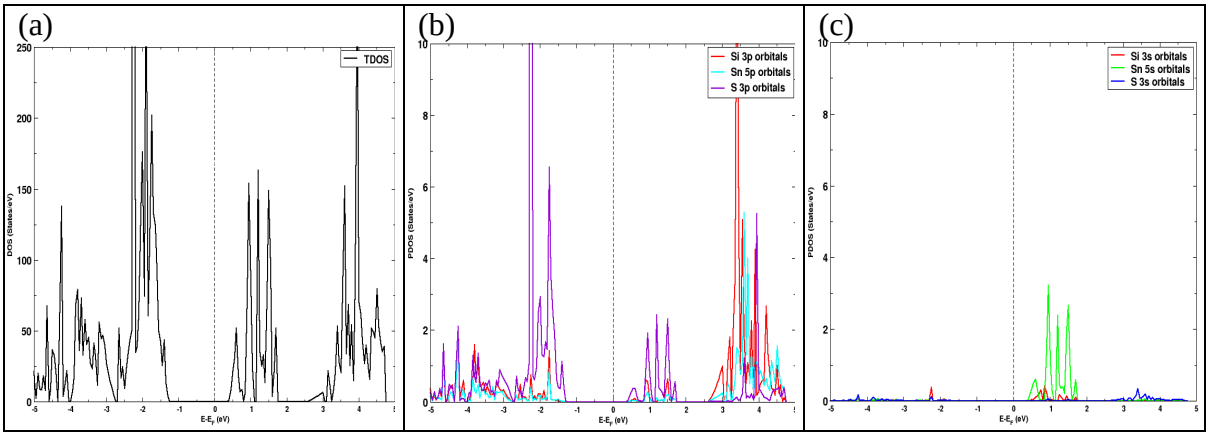

Figure 4.23: Si_{Sub-Sn} (a) TDOS, (b) PDOS for p orbitals and (c) PDOS for s orbitals.

are contributed by a hybridization of Si 3p, Sn 5p, S 3p, Sn 5s and Si 3s orbitals, as shown in figure 4.23 (b) and (c). The VBM appears at low energy levels of -1.24 eV and is mainly composed of S 3p orbitals, as shown in figure 4.23 (b). The valence states are contributed by hybridization of S 3p, Sn 5p, Si 3p and Sn 5s orbitals as shown in figure 4.23 (b) and (c). There are no intermediate states for Si_{Sub-Sn} configuration, shown in figure 4.23 (a).The exact values of the band gaps for the Si doped configurations along with pristine SnS_2 band gap are shown in table 4.5. Much like C doped configurations, all the Si doped configurations E_g values are smaller than pristine SnS_2 and are within the range at which visible light excites electrons into the conduction band ($E_g < 3.1eV$) [28]. Si_{Sub-S}

configuration has the least band gap value (1.35 eV) and Si_{Sub-Sn} has the highest band gap value (1.65 eV) of all doped configurations.

Table 4.5: The different band gaps of the silicon doped configurations compared with pristine SnS_2.

Configurations	E_g (eV)
SnS_2	2.34
Si_{Int}	1.50
Si_{Ads-S}	1.45
Si_{Ads-Sn}	1.40
Si_{Sub-S}	1.35
Si_{Sub-Sn}	1.65

4.4.3 Charge density differences of silicon doped configurations

The charge density difference plots for Si doped configurations will again be used to further understand the bonding dynamics between the impurity atom and host material's atoms. For all Si doped systems in figure 4.24, the black sphere denotes a Si atom, the yellow spheres denote S atoms and purple spheres denote Sn atoms. The orange cloud depicts a depletion of charge (positive) region and the blue cloud depicts an accumulation of charge (negative) region for all configurations. These charged regions were again calculated with equation (4.7), using parameters specific for silicon doped configurations. That is, ρ^{total} is the charge of the Si doped supercell. The term $\sum_i \rho^{fragments}$, is the sum of charges of the individual components, these are, the charge of the Si dopant and the charge of the pristine supercell. Thus, final result will be the charge density distribution

around the doped region of the material. Advantages imposed by these charged surfaces have been discussed as reaction centres for charge carriers OH^- and H^+.

The electronegativity is a major contribution factor to these charge shifts. The order of the electronegativity values, of the interest atoms, is S > Si > Sn (the exact values being: 3.44 > 2.82 > 2.68, respectively) [33]. Again, S has the highest electronegativity and Sn has the lowest. Therefore, it is expected that sulphur will have a larger electron cloud than all other atoms and tin is expected to have the largest positive cloud than all other atoms.

The top and side views of the Si doped charge surfaces of (a) Si_{Int}, (b) Si_{Ads-S}, (c) Si_{Ads-Sn}, (d) Si_{Sub-S} and (e) Si_{Sub-Sn} are shown in figure 4.24. In figure 4.24 (a) for Si_{Int} configuration, the Si atom is surrounded by a larger blue cloud (negative charge) shaped as a 3-pointed star, as a result of attaining electron charge from the adjacent less electronegative Sn. S atoms, with the highest electronegativity were also surrounded by blue clouds. Therefore, Si_{Int} configuration has a larger spread of negative than positive making the doped region of Si_{Int} a suitable reduction zone for H^+/H_2.

Figure 4.24 (b) shows the Si_{Ads-S} configuration. It is noticed from the top view that the blue cloud (electron charge) is more concentrated at the doped region and orange cloud (positive charge) is spread about the adjacent Sn atoms. Also noticed from the side view is an orange cloud above and below the Si atom and a blue cloud around it. This is expected as S pulls electrons from all atoms around it and a greater pull from adjacent (least electronegative) Sn atoms leading to the large orange clouds at the adjacent Sn atoms. Therefore, the doped region could be a good reduction zone (H^+/H_2) since the concentration of electron clouds is around this region.

Figure 4.24 (c) presents the charge density difference for Si_{Ads-Sn} configuration. The blue cloud in the shape of a 3-pointed star on the Si atom is noticed, blue clouds around the S atoms are noticed and a huge orange cloud around the Sn atom is noticed. This is a clear indication of the electron pull by the Si and S atoms bonded to the Sn atom. A similar result is observed with Si_{Sub-S} configuration in figure 4.24 (d). It is noticed that Si has a huge blue cloud around it as it is bonded to three less electronegative Sn atoms. A blue cloud is also noticed at the Sn atoms adjacent to the Si dopant because Sn has the largest

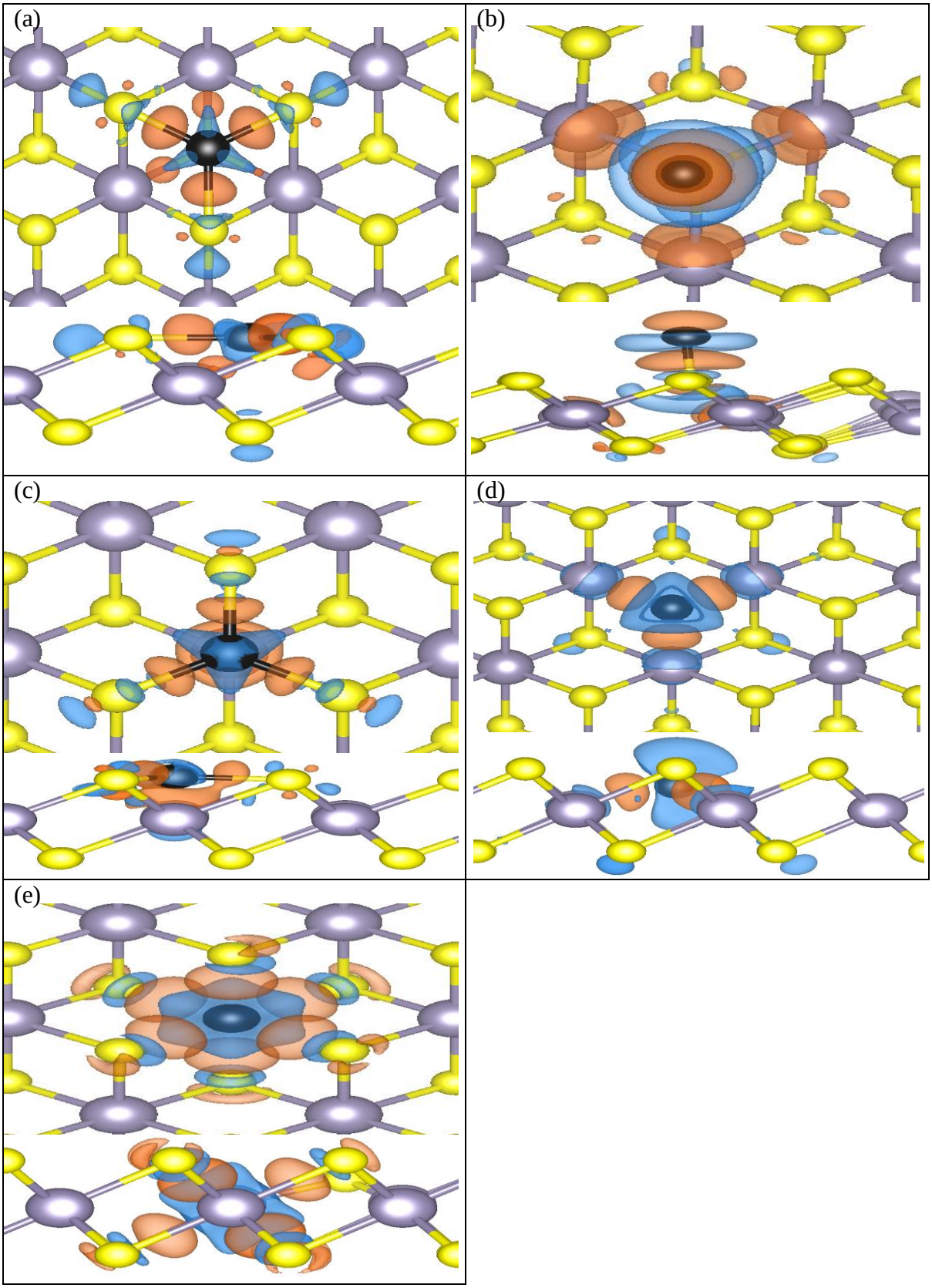

Figure 4.24: Charge density difference diagrams for: (a) Si_{Int}, (b) Si_{Ads-S}, (c) Si_{Ads-Sn}, (d) Si_{Sub-S} and (e) Si_{Sub-Sn}.

number of pseudo electrons. The Si pulling on the three bigger Sn atoms will cause it to move towards the middle Sn atoms layer.

Figure 4.24 (e) presents the charge density differences for Si_{Sub-Sn} configuration. A blue cloud surrounds the Si dopant. This indicates that the Si atom was able to retain some of its charge, which could be due to a larger number of pseudo electrons. Also noticed in between Si and S bonds are orange clouds and blue clouds. This shows that valence electrons shifted from Si atom to S atoms due to the high electronegativity of S.

4.4.4 Band edge alignment of pristine and silicon doped configurations

A comparison of the VBM and CBM to the water redox potentials is presented in figure 4.25. All band gap values are suitable for light activation of electrons ($E_g < 3.1\ eV$) [28] as illustrated in table 4.5. The band gap values for all doped configurations are below the pristine SnS_2 band gap value. Thus, Si doped configurations require less photoactivation energy than pristine SnS_2. Figure 4.25 shows the band alignment for pristine SnS_2 compared with the silicon doped configurations. Labels above the bars are the pristine and doped configurations and below the bars are their corresponding band gaps. The values inside the bar charts are the differences of the band edges (CBMs and VBMs) of the doping configurations and the pristine SnS_2. The negative values show a downward shift while the positive values show an upward shift from the reference band edges (pristine SnS_2). The orange bars are the conduction bands and green bars are the valence bands. The blue dashed line across the graph is the reduction potential and the red dashed line is the oxidation potential.

The effect of VBM and CBM positions for pristine SnS_2 with respect to water redox potentials has been discussed in the C doped study. The focus in this section will only be for Si doped configurations. Doped configuration Si_{Int} has a band gap $E_g = 1.50\ eV$ which is ideal for photoactivation with visible light and a VBM that is 0.76 eV below the pristine VBM. Much like C_{Int} configuration, the CBM of Si_{Int} configuration is far below the H^+/H_2 potential. Hence, this doping configuration is not suitable for hydrogen evolution, but would be spontaneous for oxygen evolution. This is a similar observation

with doped configurations Si_{Ads-S}, Si_{Ads-Sn} and Si_{Sub-Sn}, but with differing magnitudes. Si_{Ads-S} configuration has an E_g of 1.45 eV, the VBM is 0.66 eV below the reference and CBM is 1.36 eV below the reference. Si_{Ads-Sn} configuration has an E_g of 1.40 eV, the VBM is 0.84 eV below the reference and CBM is 1.59 eV below the reference. Si_{Sub-Sn} configuration has an E_g of 1.65 eV, the VBM is 0.67 eV below the reference and the CBM is 1.17 eV below the reference. Thus, these doping configurations are only suitable for oxygen evolution. A unique result is observed with Si_{Sub-S} configuration, with an E_g of

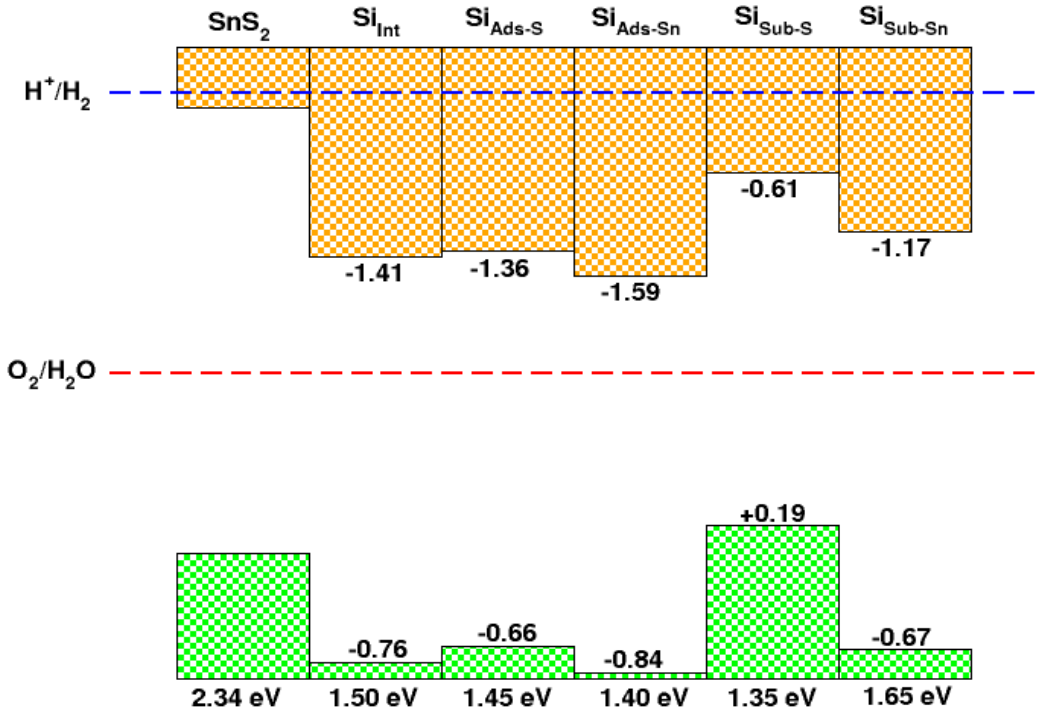

Figure 4.25: Band edge alignment for pristine SnS_2 and silicon doped configurations: Si_{Int}, Si_{Ads-S}, Si_{Ads-Sn}, Si_{Sub-S} and Si_{Sub-Sn}.

1.35 eV, the VBM is 0.19 eV above the reference, which is still below O_2/H_2O, and the CBM is 0.61 eV below reference CBM. The CBM for pristine SnS_2 is below H^+/H_2, therefore the CBMs of all Si doped configurations being below the CBM of pristine means the CBMs of doped are far below H^+/H_2, thus unsuitable for water reduction. As mentioned by Lindquist *et al.* [34] that when CBM is below H^+/H_2, an external voltage is

required for PEC water reduction to proceed. Therefore, Si_{Sub-S} is the Si doped configuration with a CBM closet to H^+/H_2. A minimum external bias of 0.75 eV is required to lift the CBM of Si_{Sub-S} to potentials above H^+/H_2. This would also raise the VBM to an energy level that is 0.31 eV below O_2/H_2O, which is still suitable for oxygen evolution. Thus, making Si_{Sub-S} the most suitable Si doped configuration for water splitting to produce both hydrogen and oxygen.

4.5 Brief Summary

All calculations in this work used cut-off of 450 eV and k-point mesh of $8 \times 8 \times 1$ to obtain equilibrium properties of pristine SnS_2. A FGO calculation was performed using PW-scf in quantum espresso. A positive cohesive energy for pristine SnS_2 monolayer signifies overall chemical stability. GGA+U was used to mitigate band gap underestimation by the GGA. The identified doped configurations are: C_{Int}, C_{Ads-S}, C_{Ads-Sn}, C_{Sub-S} and C_{Sub-Sn} for C doped configurations, and are: Si_{Int}, Si_{Ads-S}, Si_{Ads-Sn}, Si_{Sub-S} and Si_{Sub-Sn} for Si doped configurations. Formation energy calculations, total and partial density of states, charge density difference and band edge alignment simulations were performed for all doped configurations. The formation energies were all positive, thus all doped configurations are endothermic and experimentally synthesizable under ambient conditions. Si doping has lower overall formation energy than C doping. The $5 \times 5 \times 1$ supercell was chosen in order to eliminate supercell strain felt as a result of doping. All band gap values for pristine and doped SnS_2 monolayer were within the range of photoactivation. Moreover, all doped configurations had band gaps lower than that of pristine, thus it can be concluded that C/Si atom doping reduces the band gap of SnS_2. It was noticed from charge density differences that the Si atom is a negative region, thus suitable for water reduction (H^+/H_2) and C atom is a positive region, thus suitable for water oxidation (O_2/H_2O). It was observed from the band edge alignment diagrams that, with an application of an external bias, pristine SnS_2, C_{Sub-S} and Si_{Sub-S} are the most suitable for overall water splitting for photo-production of both hydrogen and oxygen.

BIBLIOGRAPHY

[1] Giannozzi, P. *et al.* (2009). *Quantum Espresso: A modular and open-source software project for quantum simulations of materials*. Journal of Physics: Condensed Matter, 21(39), p. 395502. Available at: https://doi.org/10.1088/0953-8984/21/39/395502.

[2] Kokalj, A. (1999). *XCrySDen—a new program for displaying crystalline structures and electron densities*. Journal of Molecular Graphics and Modelling, 17(3–4), pp. 176–179. doi:10.1016/s1093-3263(99)00028-5.

[3] Mabiala-Poaty, H., Douma, D., M'Passi-Mabiala, B. and Mapasha, R. (2018). *Structural and electronic properties of SnS 2 stacked nanosheets: An ab-initio study*. Journal of Physics and Chemistry of Solids, 120, pp.211-217.

[4] Burton, L.A. *et al.* (2016). *Electronic and optical properties of single crystal SnS_2: An Earth-abundant disulfide photocatalyst*. Journal of Materials Chemistry A, 4(4), pp. 1312–1318. Available at: https://doi.org/10.1039/c5ta08214e.

[5] Wan, W. (2018) *Efficient Generation of K-point Grids for Quantum ESPRESSO and Catalytic Role of CoP (101) for Electrochemical Hydrogen Evolution Compared with Pt (100) and Pt (111)*. Thesis. Johns Hopkins University.

[6] Wang, Y. *et al.* (2021). *Rapid generation of optimal generalized Monkhorst-pack grids*. Computational Materials Science, 187, p. 110100. Available at: https://doi.org/10.1016/j.commatsci.2020.110100.

[7] Monkhorst, H.J. and Pack, J.D. (1976). *Special points for Brillouin-zone integrations*. Physical Review B, 13(12), pp. 5188–5192. Available at: https://doi.org/10.1103/physrevb.13.5188.

[8] Eads, C.N. *et al.* (2017). *Anisotropic attosecond charge carrier dynamics and layer decoupling in quasi-2d layered SnS_2*. Nature Communications, 8(1). Available at: https://doi.org/10.1038/s41467-017-01522-3.

[9] Politzer, P., Murray, J.S (2018). *The Hellmann-Feynman theorem: a perspective*. J Mol Model **24**, 266.

[10] Kittel, C. (2004). *Introduction to Solid State Physics*. 8th ed. Berkeley: University of California, pp.58-60.

[11] Abdulsalam, M., 2015. *A Theoretical Investigation of the Structural, Electronic and Optical Properties of Transition Metal Chalcogenides*. Ph.D. University of the Witwaterstrand.

[12] Grosso, G. and Parravicini, G.P. (2014) *Solid State Physics*. 2nd edn. Oxford, Kidlington: Elsevier, pp.64-104.

[13] Bhavani, J. and John, R. (2020). *Band Gap Engineering of Cu2ZnSnX4 (X = S, Se and Te) Quaternary Semiconductors Using PBE-GGA, TB-mBJ and mBJ+U Potentials*. International Journal of Materials, Mechanics and Manufacturing, 8(1).

[14] Lieb, E. and Oxford, S. (1981). *Improved lower bound on the indirect Coulomb energy*. International Journal of Qunatum Chemistry, 19(3), pp.427-439.

[15] Gong, Y., Yuan, H., Wu, C., Tang, P., Yang, S., Yang, A., Li, G., Liu, B., van de Groep, J., Brongersma, M., Chisholm, M., Zhang, S., Zhou, W. and Cui, Y. (2018). *Spatially controlled doping of two-dimensional SnS2 through intercalation for electronics*. Nature Nanotechnology, 13(4), pp.294-299.

[16] Zhu, X. *et al.* (2018). *Band Gap Engineering of SnS_2 nanosheets by anion–anion codoping for visible-light photocatalysis*. RSC Advances, 8(6), pp. 3304–3311. Available at: https://doi.org/10.1039/c7ra12058c.

[17] Bacaksiz, C., Cahangirov, S., Rubio, A., Senger, R., Peeters, F. and Sahin, H. (2016). *Bilayer SnS_2: Tunable stacking sequence by charging and loading pressure*. Physical Review B, 93(12).

[18] Delplancke-Ogletree, M. (2006). *Cathodic Arc Evaporation and its Applications to Thin-Film Synthesis*. Materials Surface Processing by Directed Energy Techniques, pp.383-410.

[19] Shown, I., Samireddi, S., Chang, Y., Putikam, R., Chang, P., Sabbah, A., Fu, F., Chen, W., Wu, C., Yu, T., Chung, P., Lin, M., Chen, L. and Chen, K. (2018). *Carbon-doped SnS_2 nanostructure as a high-efficiency solar fuel catalyst under visible light*. Nature Communications, 9(1).

[20] Freysoldt, C. *et al.* (2014). *First-principles calculations for point defects in solids*. Reviews of Modern Physics, 86(1), pp. 253–305. Available at: https://doi.org/10.1103/revmodphys.86.253.

[21] Samad, A., Noor-A-Alam, M. and Shin, Y.-H. (2016). *First Principles Study of a SnS_2/graphene heterostructure: A promising anode material for rechargeable na ion batteries*. Journal of Materials Chemistry A, 4(37), pp. 14316–14323. Available at: https://doi.org/10.1039/c6ta05739j.

[22] Li, B. *et al.* (2017). *A two-dimensional Fe-doped SNS2 magnetic semiconductor*. Nature Communications, 8(1). Available at: https://doi.org/10.1038/s41467-017-02077-z.

[23] Earwood, W.P. (2017) *Phase stability in cobalt-based L12 Quaternary intermetallics from density functional theory*. dissertation.

[24] Mayeshiba, T. and Morgan, D. (2017). *Strain effects on oxygen vacancy formation energy in Perovskites*. Solid State Ionics, 311, pp. 105–117. Available at: https://doi.org/10.1016/j.ssi.2017.09.021.

[25] Shown, I., Samireddi, S., Chang, YC. *et al.* (2018). *Carbon-doped SnS_2 nanostructure as a high-efficiency solar fuel catalyst under visible light*. Nat Commun **9**, 169. https://doi.org/10.1038/s41467-017-02547-4.

[26] Almadori, Y. *et al.* (2019). *Fermi level shift in carbon nanotubes by Dye Confinement*. Carbon, 149, pp. 772–780. Available at: https://doi.org/10.1016/j.carbon.2019.04.041.

[27] Mead, C.A. and Spitzer, W.G. (1964). *Fermi level position at metal-semiconductor interfaces*. Physical Review, 134(3A). Available at: https://doi.org/10.1103/physrev.134.a713.

[28] Yaghoubi, H. *et al.* (2014). *Toward a visible light-driven photocatalyst: The effect of midgap-states-induced energy gap of undoped tio2nanoparticles*. ACS Catalysis, 5(1), pp. 327–335. Available at: https://doi.org/10.1021/cs501539q.

[29] Simfukwe, J. *et al.* (2021). *Ab initio studies of bimetallic-doped {0001} hematite surface for enhanced photoelectrochemical water splitting*. Catalysts, 11(8), p. 940. Available at: https://doi.org/10.3390/catal11080940.

[30] Mahata, A. *et al.* (2014). *Direct vs. indirect pathway for nitrobenzene reduction reaction on a Ni catalyst surface: A density functional study*. Phys. Chem. Chem. Phys., 16(47), pp. 26365–26374. Available at: https://doi.org/10.1039/c4cp04355c.

[31] Chang, S.-min and Liu, W.-szu (2011). *Surface doping is more beneficial than bulk doping to the photocatalytic activity of vanadium-doped tio2*. Applied Catalysis B: Environmental, 101(3-4), pp. 333–342. Available at: https://doi.org/10.1016/j.apcatb.2010.09.035.

[32] Simfukwe, J. *et al.* (2018). *Density functional theory study of CU doped {0001} and {01$\overline 1 $2} surfaces of hematite for water splitting*. MRS Advances, 3(13), pp. 669–678. Available at: https://doi.org/10.1557/adv.2018.180.

[33] Tantardini, C. and Oganov, A.R. (2021). *Thermochemical electronegativities of the elements*. Nature Communications, 12(1). Available at: https://doi.org/10.1038/s41467-021-22429-0.

[34] Lindquist, S.-E. and Fell, C. (2009). *Fuels – hydrogen production | photoelectrolysis*. Encyclopedia of Electrochemical Power Sources, pp. 369–383. Available at: https://doi.org/10.1016/b978-044452745-5.00319-1.

[35] Lin, Z. *et al.* (2002). *DNA attachment and hybridization at the silicon (100) surface*. Langmuir, 18(3), pp. 788–796. Available at: https://doi.org/10.1021/la010892w.

[36] Libretexts (2020) *5.4: Hybridization of carbon, Chemistry LibreTexts*. Libretexts. Available at: https://chem.libretexts.org/Bookshelves/Organic_Chemistry/Organic_Chemistry_I_(Cortes)/05%3A_Orbital_Picture_of_Bonding-

_Orbital_Combinations_Hybridization_Theory_and_Molecular_Orbitals/5.04%3A_Hybridization_of_Carbon (Accessed: November 27, 2022).

[37] Evans, J.A. (2009). *Owl (online web-based learning) (published by Cengage-Brooks/Cole)*. Journal of Chemical Education, 86(6), p. 695. Available at: https://doi.org/10.1021/ed086p695.

[38] Bu, H. *et al.* (2019). *The role of sp2 and sp3 hybridized bonds on the structural, mechanical, and electronic properties in a hard BN framework*. RSC Advances, 9(5), pp. 2657–2665. Available at: https://doi.org/10.1039/c8ra09636h.

CHAPTER 5: CONCLUSION

In this dissertation, the effects of doping with carbon and silicon on SnS_2 monolayer were studied using first-principles simulations based on DFT. The aim of this study was to improve photocatalytic properties of SnS_2 through doping to achieve its optimum performance for PEC water splitting. In this work, the calculations were performed using DFT PW-scf implemented in the quantum espresso software to obtain equilibrium properties of C/Si doped SnS_2 monolayer. GGA+U was used to mitigate the band gap usually underestimated by the standard GGA functional. Initially, SnS_2 monolayer was doped with single C dopant atom, and later with single Si dopant atom. The doped configurations studied are named: C/Si adsorbed on an interstitial position (C_{Int}/Si_{Int}), C/Si adsorbed on S (C_{Ads-S}/Si_{Ads-S}), C/Si adsorbed on Sn (C_{Ads-Sn}/Si_{Ads-Sn}), C/Si substituting S (C_{Sub-S}/Si_{Sub-S}) and C/Si substituting Sn (C_{Sub-Sn}/Si_{Sub-Sn}).

The formation energy (E_f), total and partial density of states, charge density difference and band edge alignment were calculated for the doped configurations. The formation energies are all positive, thus all doped configurations are endothermic and can experimentally be synthesized under ambient conditions. The formation energies of the identified doping configurations took the following order of stability for a $5 \times 5 \times 1$ supercell: $C_{Ads-Sn} < C_{Sub-S} < C_{Int} < C_{Ads-S} < C_{Sub-Sn}$, for C doped and $Si_{Ads-Sn} < Si_{Int} < Si_{Ads-S} < Si_{Sub-S} < Si_{Sub-Sn}$ for Si doped supercells. This is an indication that the thermodynamic stability of C/Si doped SnS_2 monolayer depends on structural configurations. Si doped configurations displayed lower formation energies than C doped configurations.

All the band gaps of the doped configurations are lower than that of the pristine SnS_2, thus it can be concluded that C/Si doping reduced the band gap of SnS_2. Interestingly, all the band gap values, including that of pristine, are within the range at which visible light excites electrons into the conduction band. It was further noticed from the TDOS and PDOS plots that C_{Int}, C_{Ads-S}, C_{Ads-Sn}, Si_{Int}, Si_{Ads-S} and Si_{Ads-Sn} configurations modified the SnS_2 material to be a n-type with intermediate bands. The C_{Sub-S}, C_{Sub-Sn} and Si_{Sub-S} modified the material to be a p-type material with no intermediate bands.

The charge density difference diagrams for C doped configurations indicate that C is a positive centre, while for Si doped configurations, Si is a negative centre, which could be the oxidation and reduction centres, respectively. From band alignment diagrams, a distinct noticeable difference between C doped and Si doped configurations is that the CBMs of the Si doped extend far below the CBM of the pristine, except for Si_{Sub-S}. The VBMs of both C and Si doped configurations extend far below the VBM of the pristine material, except for Si_{Sub-S}, C_{Sub-S} and C_{Sub-Sn}, which are actually above the VBM of the pristine. Thus, the CBMs are far below the water reduction line H^+/H_2 and VBMs are far below the water oxidation line O_2/H_2O. Thus, C/Si doping qualify for spontaneous water oxidation to synthesize oxygen (O_2). Application of an external bias potential qualifies pristine SnS_2, C_{Sub-S} and Si_{Sub-S} as the most suitable for overall water splitting for photo-production of both hydrogen and oxygen. Si_{Sub-S} has a lesser formation energy and band gap than C_{Sub-S}, however C_{Sub-S} requires a lesser external bias to raise CBM above H^+/H_2. Pristine SnS_2 has the largest band gap, but requires the least external bias to raise CBM above H^+/H_2. This research can effectively guide experimentalists to modify SnS_2 to perform at its peak for PEC WS for mass-hydrogen production to be realized.